SPECTRAL DECOMPOSITION AND ITS APPLICATION IN MAPPING STRATIGRAPHY AND HYDROCARBONS

…………………………………………

A Dissertation
Presented to

the Faculty of the Department of Geosciences
University of Houston

…………………………………………

In Partial Fulfillment
of the Requirements for the Degree
Doctor of Philosophy

…………………………………………

By

Jianlei Liu

August, 2006

Spectral decomposition and its application in mapping stratigraphy and hydrocarbons

by Jianlei Liu ________________________

Approved by

____
Dr. Kurt J. Marfurt

____
Dr. Fred J. Hilterman

____
Dr. Hua-wei Zhou

____
Dr. Aibing Li

____
Dr. Yonghe Sun, Chevron Corp.

____
Dr. John L. Bear, Dean, College of Natural Sciences and Mathematics

ACKNOWLEGEMENTS

First of all, I would like to thank my advisor, Dr. Kurt J. Marfurt, for his guidance and encouragements. Kurt not only taught me how to be a good computer programmer, but also inspired many good geophysical ideas.

Second, I especially thank my committee members Dr. Fred J. Hilterman, Dr. Huawei Zhou, Dr. Aibing Li, and Dr. Yonghe Sun for their useful comments and suggestions to my dissertation. I would also like to thank Devon Energy, Burlington Resources, and Fairfield Industries for providing field data, and the consortium sponsors of Allied Geophysical Laboratories for financial support, such as Marathon Oil, and ExxonMobil, etc. I want to acknowledge Chevron Corp. for twice giving me summer intern opportunities which helped me learn geophysics as it is used in an industrial setting.

My thanks and appreciation also go to Dr. John Castagna, Dr. De-hua Han, and Dr. Gennady Goloshubin for their useful discussions and feedback. The help from graduate students, staff and faculty of the Dept. of Geosciences are appreciated. I would give special thanks to Long Ma for his help during my first year in Houston.

Finally I am most indebted to my wife Zhengyun (Jenny) for her patience and encouragement. Without her support, the completion of my study would not be possible.

DEDICATION

To my wife Zhengyun (Jenny)

SPECTRAL DECOMPOSITION AND ITS APPLICATION IN MAPPING STRATIGRAPHY AND HYDROCARBONS

…………………………………………….

An Abstract of a Dissertation
Presented to

the Faculty of the Department of Geosciences
University of Houston

…………………………………………….

In Partial Fulfillment
of the Requirements for the Degree
Doctor of Philosophy

…………………………………………….

By

Jianlei Liu

August, 2006

ABSTRACT

In this dissertation, I develop a new spectral decomposition method and apply it to mapping stratigraphy and hydrocarbons. This new spectral decomposition method combines matching pursuit concepts with a least-squares solution, providing an accurate time-frequency decomposition. The output spectral attributes include single frequency, peak frequency, peak amplitude, and peak phase volumes. Based on these spectral attributes, I can generate the composite volume of either peak frequency or phase with peak amplitude. I also show how I can plot spectral attributes which include a newly developed Red-Green-Blue display method.

I demonstrate the value of spectral decomposition through these applications. First I use spectral attributes to predict thin bed thickness of a Pennsylvanian age limestone verified by equations and a synthetic model. Next I show how to use composite volume of peak frequency, peak amplitude and coherence to detect channels in a Tertiary Gulf of Mexico as well as in a Paleozoic West Texas survey. Coherence can detect the lateral variation, while peak frequency can show the vertical thickness variation. Finally, I show how the new Red-Green-Blue display technique, which is based on three different basis functions, can be used to detect low frequency zones.

TABLE OF CONTENTS

LIST OF FIGURES

CHAPTER 1

SPECTRAL DECOMPOSITION USING PROJECTION METHODS

1.1 INTRODUCTION

Although the short window discrete Fourier transform (SWDFT) has been used by seismic processors in time-variant spectral balancing since the advent of digital processing, Morlet *et al.* (1982) appears to be the first to generate such spectra for purposes of seismic interpretation. Morlet *et al.*'s (1982) SWDFT was based on Gaussian-tapered sines and cosines (now called Morlet wavelets) that are often a good approximation to real seismic wavelets. Partyka *et al.* (1999) who used tapered rectangular windowed sines and cosine wavelets were the first to demonstrate the value of spectral decomposition in interpreting 3D seismic data volumes. Marfurt and Kirlin (2001) used the short window discrete Fourier transforms (SWDFT) to directly decompose a seismic signal into its Fourier components. Sinha *et al.* (2003, 2005) used variable window Morlet wavelets as their wavelet basis, generating a suite of frequency sections that can be used to study anomalous tuning and attenuation.

Stockwell *et al.* (1996) introduced the S-transform which is very similar to Morlet *et al.*'s technique. Taner and Treitel (2004) showed the harmonic attributes based on Gabor-

Morlet wavelet theory. The only difference in spectral decomposition between S-transform and Morlet *et al.*’s technique is that the S-transform scales the output by the mean frequency. The S-transform is a good tool to analyze local time-frequency distribution using a frequency dependent window. The advantage of the S-transform over the short window discrete Fourier transform is that the low frequency analysis uses a longer time window while the high frequency analysis uses a shorter time window. Matos *et al.* (2005) examined the maximum peak frequencies computed using the S-transform for reservoir characterization. Odebeatu *et al.* (2006) applied the S-transform to detect gas reservoir anomalies. In this chapter, I will introduce the theoretical background of spectral decomposition using projection methods, which include both the short window discrete Fourier transform (SWDFT) and the S-transform.

I begin this chapter by reviewing the implementation of the most popular spectral decomposition methods currently in use, the SWDFT. I then introduce the S-transform and discuss the difference between the SWDFT and the S-transform. Next, I use a synthetic example to compare the different decomposed spectral attributes including the amplitude and phase spectra. Finally, I decompose a seismic line extracted from a 3-D seismic survey acquired over the Louisiana Shelf, Gulf of Mexico using the S-transform and examine different spectral components.

1.2 THEORY OF SPECTRAL DECOMPOSITION USING PROJECTION METHODS

1.2.1 *Short Window Discrete Fourier Transform (Transform using Constant Size Windows)*

Conventional spectral decomposition is usually performed using the short window discrete Fourier transform (SWDFT). Partyka *et al.* (1999) proposed the application of the SWDFT to generate common frequency cubes. They first selected a data analysis window containing stratigraphic features of interest. The next step is to transform the time-domain data to frequency domain using the SWDFT. After spectral balancing (Chapter 2), they viewed the decomposed common frequency horizon slices to identify textures and geological patterns.

The equation for the short window discrete Fourier transform can be written as (Mallat, 1999)

$$U_{SWDFT}(\tau, f) = \frac{1}{\sqrt{2\pi}} \int u(t) W(t-\tau) e^{-j2\pi ft} dt \ , \tag{1-1}$$

where $u(t)$ is the time domain seismic data, τ is the center time of the window function $W(t-\tau)$, f is the frequency, and $U_{SWDFT}(\tau, f)$ is the time-frequency function. The defined window $W(t-\tau)$ can be either a tapered or untapered rectangular window (boxcar), Gaussian window, Hamming window, or Hanning window (Mallat, 1999).

Figure 1.1 shows three different windows include both tapered and untapered rectangular windows, and a Gaussian window.

Partyka *et al.* (1999) use a tapered rectangular window, while Mallat (1999) uses a Gaussian window of the form

$$W(t-\tau) = e^{-\sigma^2 (t-\tau)^2} \quad , \tag{1-2}$$

where σ is a constant value controlling the window size, with larger values of σ resulting in smaller time windows. In Figure 1.2 I plot $e^{\frac{-(\tau-t)^2 \sigma^2}{2}} \cos(2\pi ft)$ and the corresponding spectra for three different carrier frequencies. Note that the amplitude spectra of the three Morlet wavelets have the same window size and the same bandwidth.

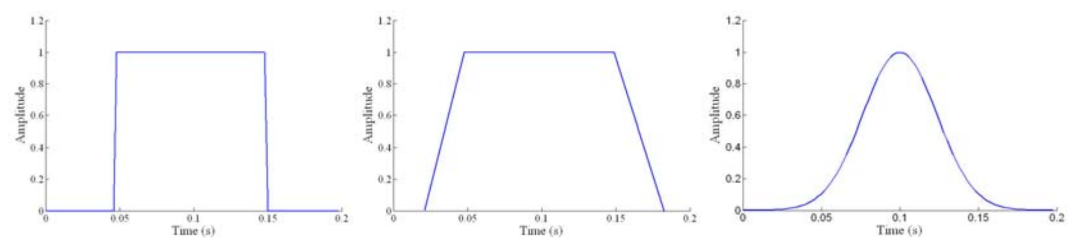

(a) (b) (c)

Figure 1.1 Three alternative windows commonly used in the short window discrete Fourier transform: (a) an untapered rectangular window, (b) a tapered rectangular window, and (c) a Gaussian window.

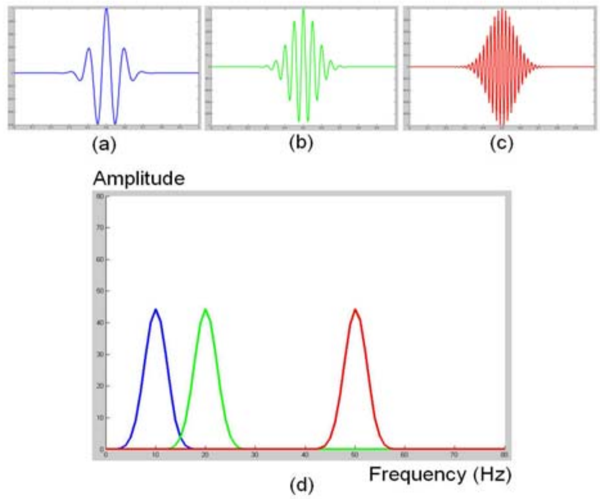

Figure 1.2 Cosine Morlet wavelets and corresponding amplitude spectra (SWDFT). Morlet wavelet of mean frequency at (a) 10Hz (blue), (b) 20Hz (green), and (c) 50Hz (red). (d) The corresponding amplitude spectra for (a), (b) and (c).

1.2.2 *The S-transform (Transform using Variable Size Windows)*

Morlet *et al.* (1982) cross-correlated both cosine and sine (or complex) Morlet wavelets W_M, with the input seismic trace $u(t)$. The instantaneous amplitude spectrum of the seismic trace is then the modulus of the complex cross-correlation coefficients. The Morlet wavelet decomposition is then given by

$$U_M(\tau, f) = \int u(t) \cdot W_M \, dt \quad , \tag{1-3}$$

where

$$W_M = e^{-(\tau - t)^2 f^2 \ln 2} e^{-i2\pi f t} , \tag{1-4}$$

W_M is the complex Morlet wavelet, and $U_M(\tau, f)$ is the complex time-frequency spectrum.

Stockwell *et al.* (1996) introduced the S-transform which differs from the Gaussian tapered SWDFT given in equation 1-2 in that the amplitude of the wavelet is a function of the carrier frequency

$$U_S(\tau, f) = \int u(t) \frac{|f|}{\sqrt{2\pi}} e^{\frac{-(\tau-t)^2 f^2}{2}} e^{-i2\pi ft} dt \quad , \tag{1-5}$$

where $u(t)$ is the input seismic trace, f is the frequency, τ is the analysis time point, t is the time, and $U_S(\tau, f)$ is the complex time-frequency spectrum. Comparing equation 1-3 and equation 1-5, we note that the S-transform is quite similar to Morlet's decomposition technique. The only difference between S-transform and Morlet wavelet decomposition is that the S-transform time-frequency function is scaled by the carrier frequency f.

The continuous wavelet transform commonly used in data compression decomposes the signal from the time domain to the time-scale domain using orthogonal wavelets that vary in length and frequency by a factor of two. In contrast, the S-transform decomposes the signal from the time domain to the time-frequency domain using non-orthogonal variable size Morlet wavelets (Mallat, 1999; Stockwell, 1996; Sinha, *et al.*, 2005). While computationally more intensive than the orthogonal wavelet transform, the non-orthogonal S-transform provides added time and frequency resolution valuable for interpretation. Stockwell *et al.* (1996) interpreted the S-transform as a combination of continuous wavelet transform and the short window discrete Fourier transform. The difference between the S-transform and the SWDFT is that the Gaussian window is a function of time and frequency for the S-transform, while the Gaussian window is only a function of time for the SWDFT.

Figure 1.3 shows three different window size Morlet wavelets and their corresponding amplitude spectra. The Morlet wavelet with a mean frequency at 10 Hz has a longer window in the time domain, resulting in a narrower bandwidth in the frequency domain. In contrast, the Morlet wavelet with a mean frequency at 50 Hz has a shorter window in the time domain, resulting in a wider bandwidth in the frequency domain. In general, the S-transform gives better low frequency resolution and reduced high frequency resolution than the corresponding SWDFT. Comparing Figures 1.2 and 1.3, we can easily see that the S-transform applies different Gaussian windows or different size Morlet wavelets to calculate the time-frequency distribution, while the SWDFT uses the same window size to do spectral decomposition.

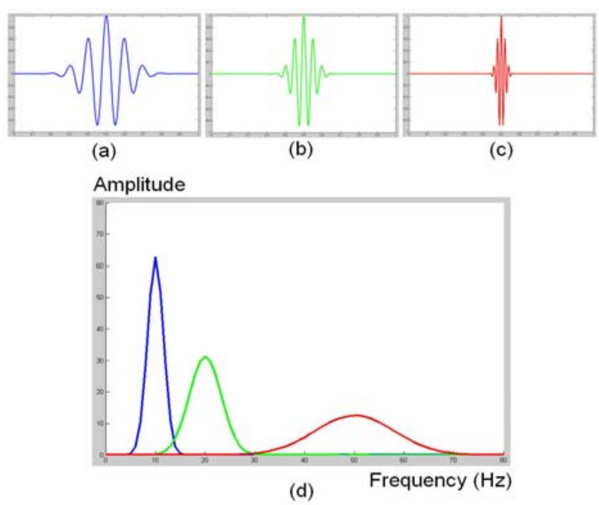

Figure 1.3 Cosine Morlet wavelets and corresponding amplitude spectra (S-transform). Morlet wavelet of mean frequency at (a) 10Hz (blue), (b) 20Hz (green), and (c) 50Hz (red). (d) The corresponding amplitude spectra for (a), (b) and (c).

According to the Heisenberg uncertainty principle, we can not obtain both good temporal resolution and frequency resolution simultaneously (Mallat, 1999; Morlet, *et al.* 1982). In other words, if we wish to obtain a good frequency resolution in our time-frequency distribution, we will need to sacrifice some temporal resolution.

I calculate the S-transform using the following four steps:

1) Pre-compute a dictionary of cosine (zero-phase) and sine (90 degree phase) Morlet wavelets for the range of frequencies of interest, thereby forming complex wavelets
2) Read in the seismic trace,
3) At each time sample, cross-correlate a time-shifted version of each complex wavelet in the dictionary with the seismic trace to generate complex cross-correlation coefficients,
4) Calculate the modulus of the above complex coefficients as the amplitude spectrum, and calculate the phase angle of the complex coefficients as the phase spectrum. For each time-frequency spectrum point, the time location is the sample of the seismic trace, while the frequency is the mean frequency of wavelet from the dictionary.

The steps above are illustrated in Figure 1.4. In Figure 1.4b only nine complex Morlet wavelets are displayed to explain the decomposition flow. In practice 80-100 wavelets are used. Figure 1.4c is the instantaneous amplitude spectrum at time 1.0 s of input seismic trace (Figure 1.4a, blue dashed line). If I repeat the same steps for other time locations, I will obtain the amplitude spectrum of whole seismic trace. The time-frequency distribution of the whole seismic trace is shown in Figure 1.5.

Fortran90 program *spec_proj,* computes spectral decomposition using both the SWDFT and the S-transform algorithms. I provide the UNIX 'man page' of this algorithm as Appendix A.

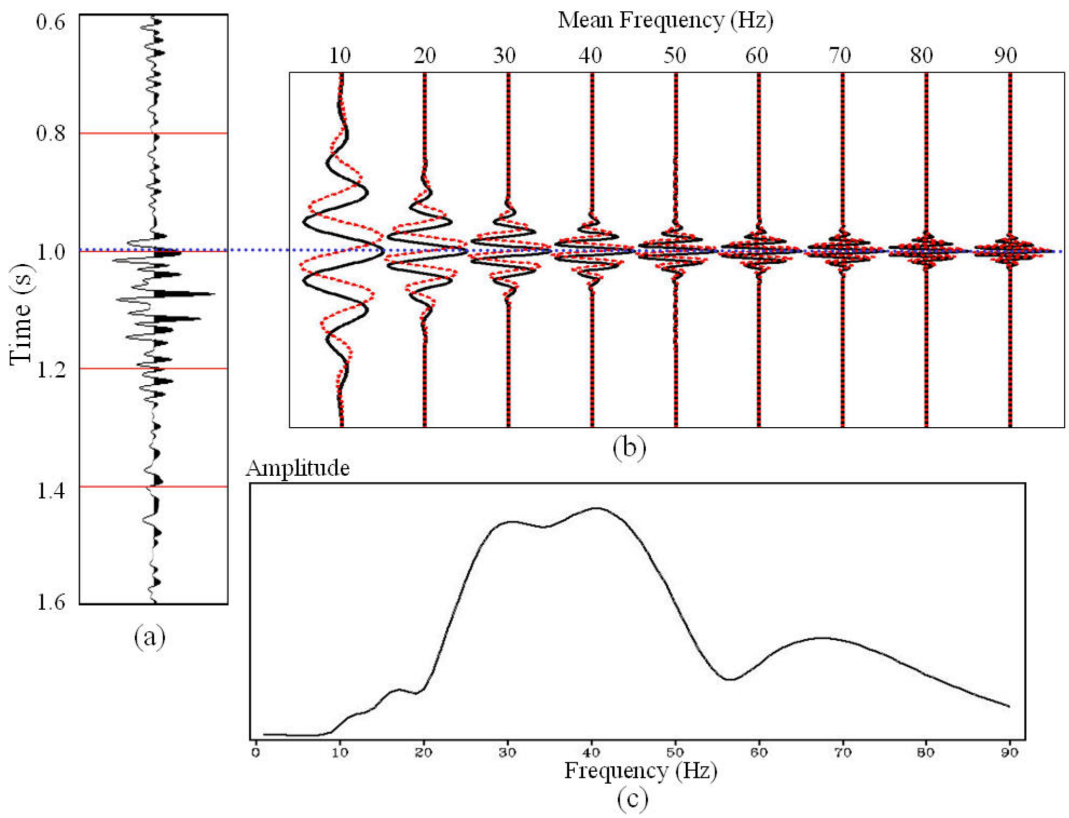

Figure 1.4 The time-frequency decomposition of the S-transform. (a) Input seismic trace, (b) cosine and sine Morlet wavelets from 10 Hz to 90 Hz (the cosine Morlet wavelet is indicated by the black solid line, the sine Morlet wavelet is indicated by the red dotted line), and (c) the instantaneous amplitude spectrum at time 1.0 s.

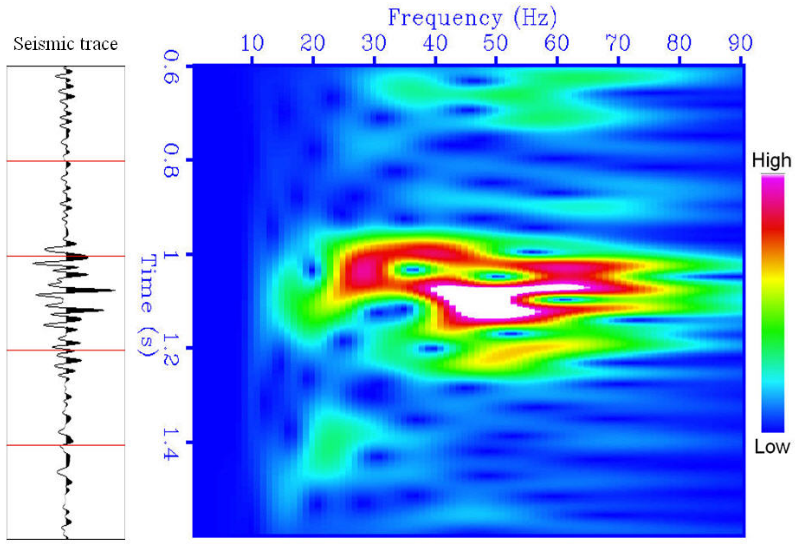

Figure 1.5 The seismic trace (from Figure 1.4a) and its time-frequency distribution using the S-transform.

1.3 SPECTRAL DECOMPOSITION EXAMPLES

I use the synthetic traces in Figure 1.6a to compare the results of the S-transform and SWDFT spectral decomposition algorithms. The synthetic traces in Figure 1.6a are composed of different phase angle Morlet wavelets with mean frequencies of 10 Hz, 30 Hz and 50 Hz. The corresponding amplitude spectrum and phase angle of the S-transform decomposition results are shown in Figures 1.6b and 1.6c. Figures 1.7 and 1.8 show the decomposed amplitude spectrum and phase spectrum using the SWDFT of fixed Gaussian windows $\sigma = 20$ and $\sigma = 30$ (described in equation 1-2), respectively. Comparing Figures 1.7 and 1.8, I note that the different Gaussian window sizes used in SWDFT result in different spectral attributes. The selected window size of SWDFT will depend on the application of spectral decomposition. If you want to interpret the low frequency attributes of seismic data, a longer window size can be used in the SWDFT. If you are interested in the high frequency contents of a certain reservoir zone, a shorter window size should be selected for the SWDFT. Comparing Figures 1.6 and 1.7, I note that the time-frequency distribution of the S-transform has better frequency resolution at lower frequencies than the SWDFT.

Figure 1.9a shows a seismic line extracted from a 3-D seismic survey acquired over West Texas, USA. In Figures 1.9b, 1.9c and 1.9d I display single frequency sections generated at 10 Hz, 30 Hz, and 50 Hz using the S-transform. These single frequency sections will serve as input to the low frequency detection by a Red-Green-Blue plot which I will discuss in Chapters 3 and 6.

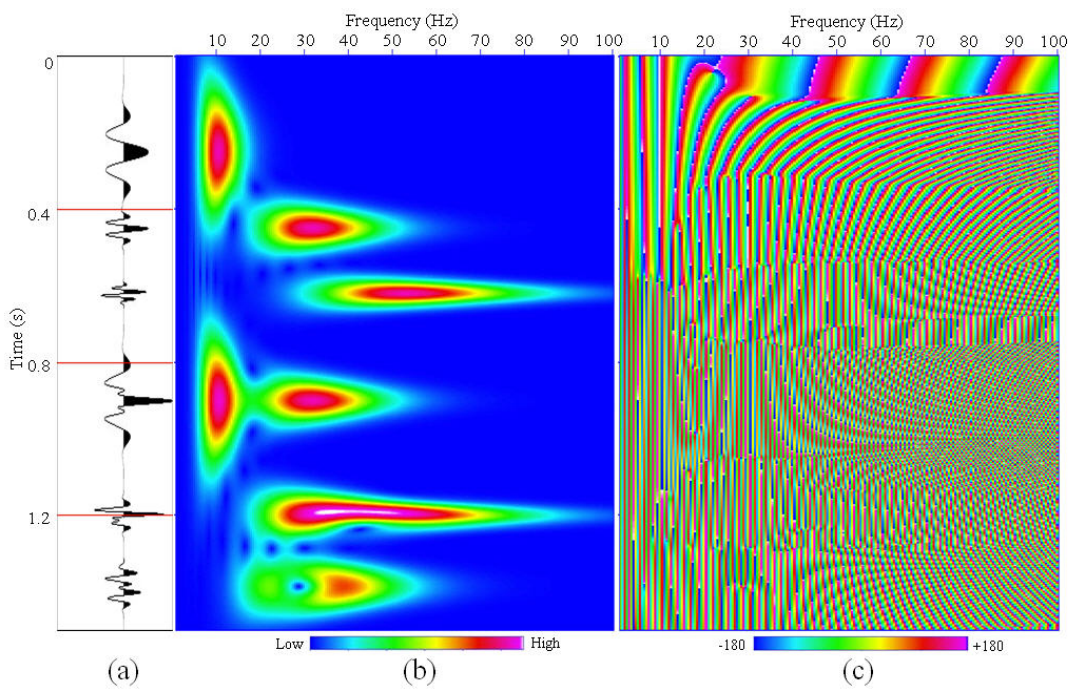

Figure 1.6 Spectral decomposition using the S-transform. (a) Synthetic trace; (b) amplitude spectrum; (c) phase spectrum.

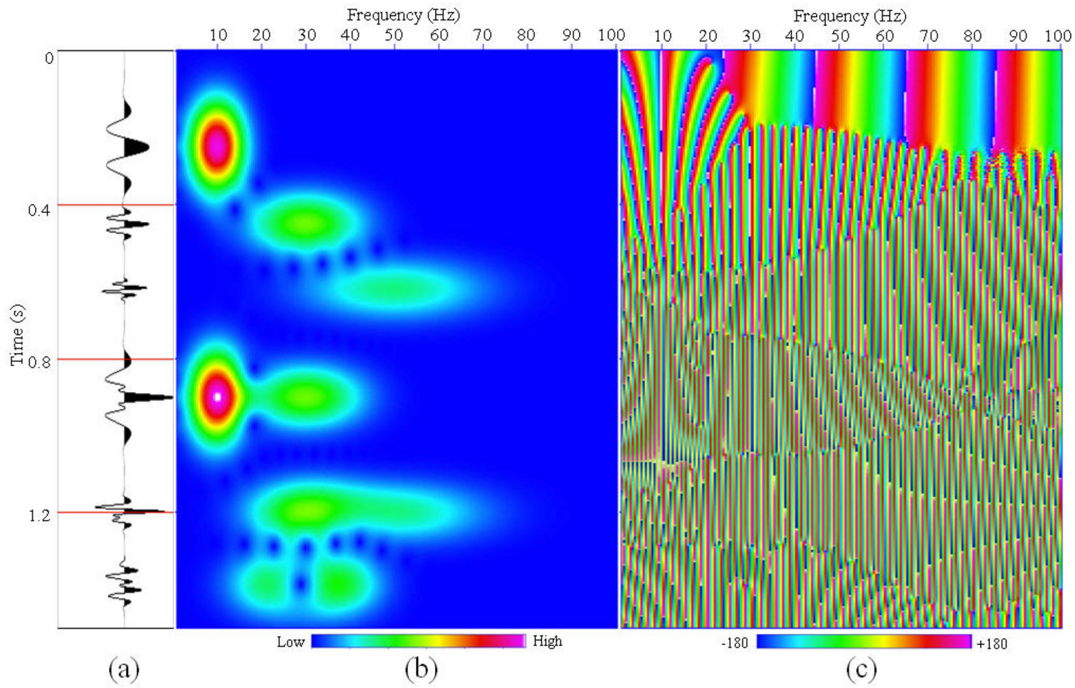

Figure 1.7 Spectral decomposition using SWDFT with fixed Gaussian window ($\sigma = 20$). (a) Synthetic trace; (b) amplitude spectrum; (c) phase spectrum.

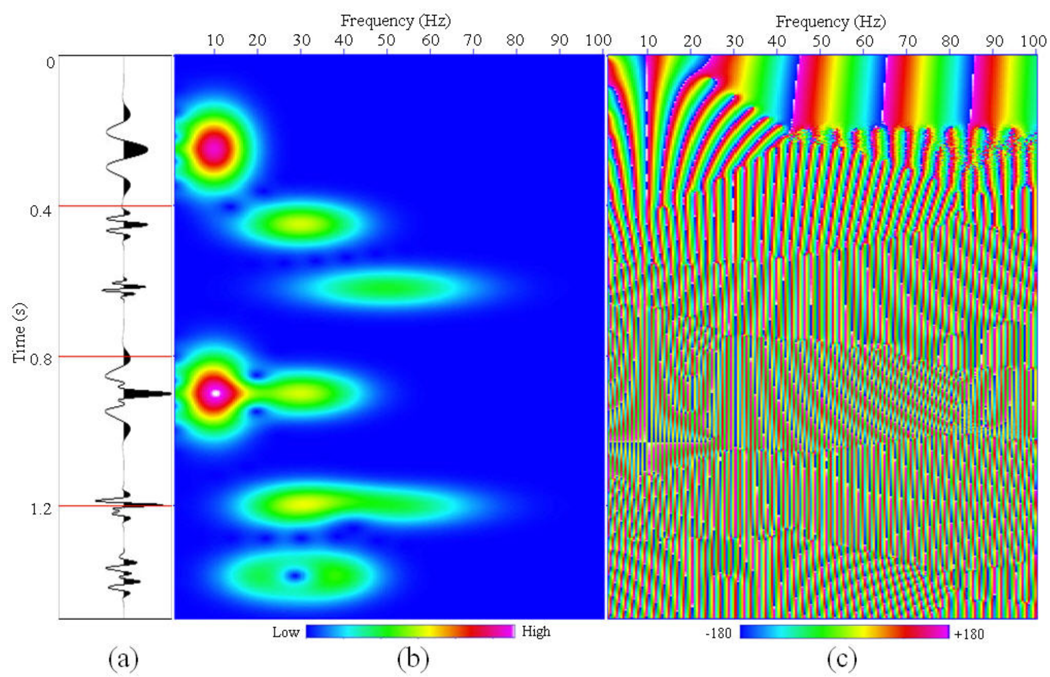

Figure 1.8 Spectral decomposition using SWDFT with fixed Gaussian window ($\sigma = 30$). (a) Synthetic trace; (b) amplitude spectrum; (c) phase spectrum.

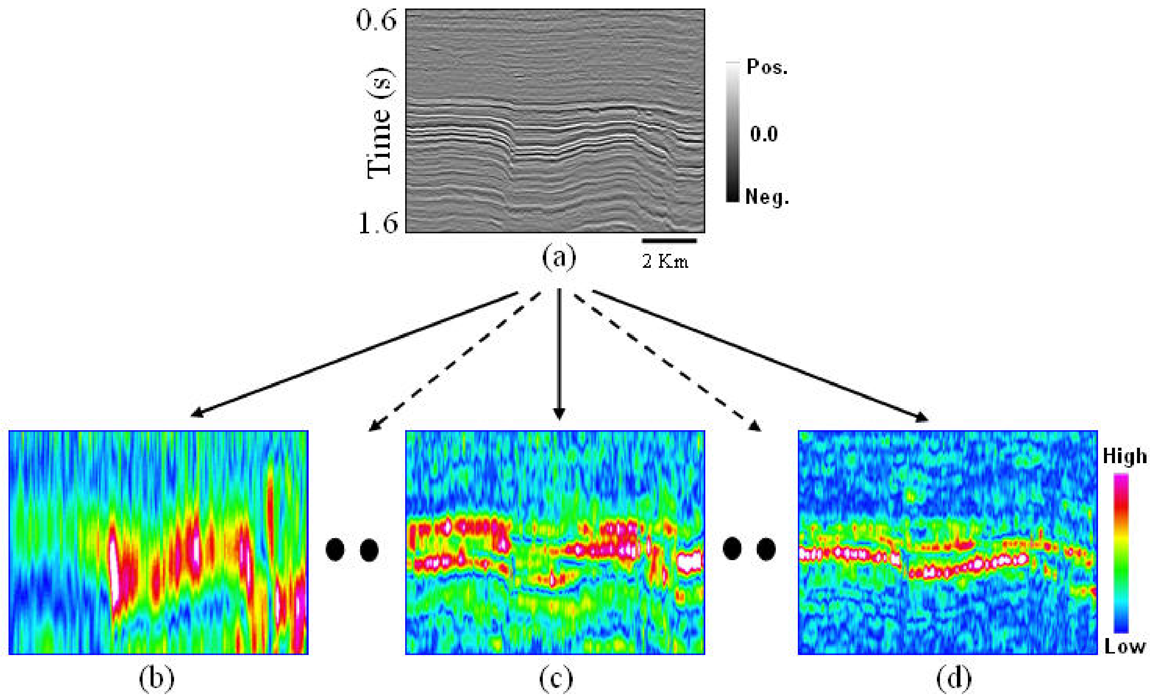

Figure 1.9 Seismic section and single frequency sections. (a) Seismic section. Single frequency section of (b) 10 Hz, (c) 30 Hz, and (d) 50 Hz. (Seismic data courtesy of Burlington Resources)

1.4 SUMMARY

Spectral decomposition using projection techniques including the short window discrete Fourier transform and the S-transform is both computationally efficient and easy to implement. Since these are projection rather than least-squares techniques, the resulting details of the two decompositions will not only be different from each other, but will also depend on the size of the window length used. The S-transform provides improved spectral resolution by using variable window length as a function of frequency. A synthetic example demonstrates that both the SWDFT and the S-transform can be used to estimate the local time-frequency variation.

CHAPTER 2

SPECTRAL DECOMPOSITION USING LEAST-SQUARES

2.1 INTRODUCTION

There are two general families of spectral decomposition algorithms – those that use a simple projection method, and those that use a more computationally intensive least-squares approach. Even with careful tapering, spectral decomposition using the SWDFT has window effects (Cohen, 1995). For this reason, Castagna *et al.* (2003) looked at alternative time-frequency decomposition methods based on wavelet transforms to compute what is commonly called instantaneous spectral attributes (ISA). Since most of the details of this approach were not published in the open literature, and since knowing the details and approximations of algorithm implementation was important to my interpretational objectives, I implemented what I thought a matching pursuit spectral decomposition algorithm should be (Mallat and Zhang, 1993), first using Ricker wavelets (Liu *et al.*, 2004) followed later by using Morlet wavelets (Liu and Marfurt, 2005).

The objective of this chapter is to describe this new spectral decomposition which combines the benefits of both matching pursuit and least-squares concept. I first introduce the theory of this new spectral decomposition. Then I discuss how I have turned this theory into a computationally-efficient algorithm. Next I use both synthetic examples and field examples to demonstrate the decomposition results. Finally, I introduce spectral balancing using the average amplitude spectrum for the seismic survey.

2.2 DECOMPOSITION THEORY

I begin the analysis by assuming that each seismic time trace, *u(t)*, is band-limited and can be represented by a linear combination of either Ricker or Morlet wavelets

$$u(t) = \sum_j a_j \cdot w(t - t_j, f_j, \varphi_j) + Noise, \tag{2-1}$$

where a_j, t_j, f_j and φ_j represent the amplitude, center time, peak frequency, and phase of the j^{th} wavelet w, respectively. I exploit complex attribute analysis and estimate the center time of each candidate wavelet by peaks of amplitude in the instantaneous envelope. The average frequency, f_{avg}, of the wavelet is estimated by the instantaneous frequency at the envelope peak [called the response frequency by Bodine (1984) and the wavelet frequency by Taner (2000).] The peak frequency, f_j, shown in equation 2-1, can be computed for the Ricker wavelet by

$$f_j = (\sqrt{\pi}/2) f_{avg} \quad , \tag{2-2}$$

and for the Morlet wavelet by

$$f_j = f_{avg} \ . \tag{2-3}$$

The temporal expression of the Ricker wavelet is given by (Sheriff, 2002)

$$w_R(t, f_j) = (1 - 2\pi^2 f_j^2 t^2)\exp(-\pi^2 t^2 f_j^2) \quad , \tag{2-4}$$

while its spectrum is given by

$$\bar{w}_R(f, f_j) = \frac{2}{\sqrt{\pi}} \frac{f^2}{f_j^3} \exp(-\frac{f^2}{f_j^2}) \ . \tag{2-5}$$

The temporal expression of the Morlet wavelet is given by (Morlet, *et al.*, 1982)

$$w_M(t, f_j) = \exp(-t^2 f_j^2 \cdot \ln 2 / k) \cdot \exp(i2\pi f_j t) \ , \tag{2-6}$$

while its spectrum is given by:

$$\bar{w}_M(f, f_j) = \frac{\sqrt{\pi / \ln 2}}{f_j} \cdot \exp[-k \cdot \frac{\pi^2 (f - f_j)^2}{\ln 2 \cdot f_j^2}] \ . \tag{2-7}$$

where f_j is the peak frequency, and k is a constant value that controls the wavelet breadth. If I use smaller values of k, I will include more cycles in the Morlet wavelet. In our process, I choose k=0.5 (such that the cosine Morlet wavelet has three lobes).

To efficiently solve for both the amplitude and phase of each wavelet, I use the Hilbert transform, and form both an analytic data trace

$$U(t) = u(t) + iu^H(t) , \tag{2-8}$$

and a table of complex wavelets

$$W(t, f_j) = w(t, f_j) + iw^H(t, f_j) \ , \tag{2-9}$$

where w are symmetric cosine wavelets and w^H are antisymmetric sine wavelets. Figures 2.1a and 2.2a show both zero-phase and 90 degree phase Ricker wavelets and Morlet wavelets, respectively. Figures 2.1b and 2.2b display their corresponding amplitude spectra with a peak frequency at 30 Hz.

Before I decompose the seismic trace, I precompute a wavelet dictionary which is composed of zero-phase wavelets and 90 degree phase wavelets with different peak frequencies (Figure 2.3). The zero-phase and 90 degree phase Ricker wavelets with different peak frequencies are shown in Figures 2.3a and 2.3b. The zero-phase and 90 degree phase Morlet wavelets with different peak frequencies are shown in Figures 2.3c and 2.3d. Combining the zero-phase and 90 degree phase wavelets, I can build the complex wavelet dictionary, $W(t, f_j)$ using equation 2-9.

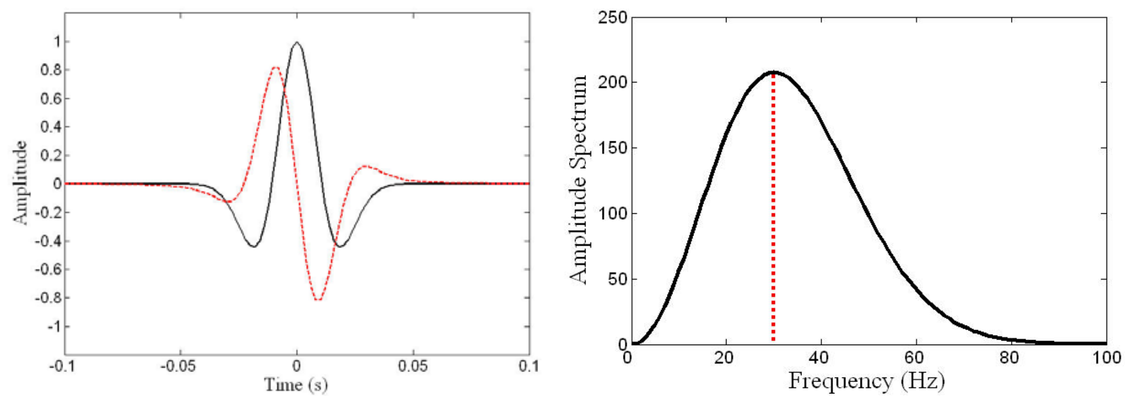

(a) (b)

Figure 2.1 30 Hz Ricker wavelets and corresponding amplitude spectrum. (a) Zero phase Ricker wavelet (black) and 90 degree phase Ricker wavelet (red). (b) Amplitude spectrum of (a).

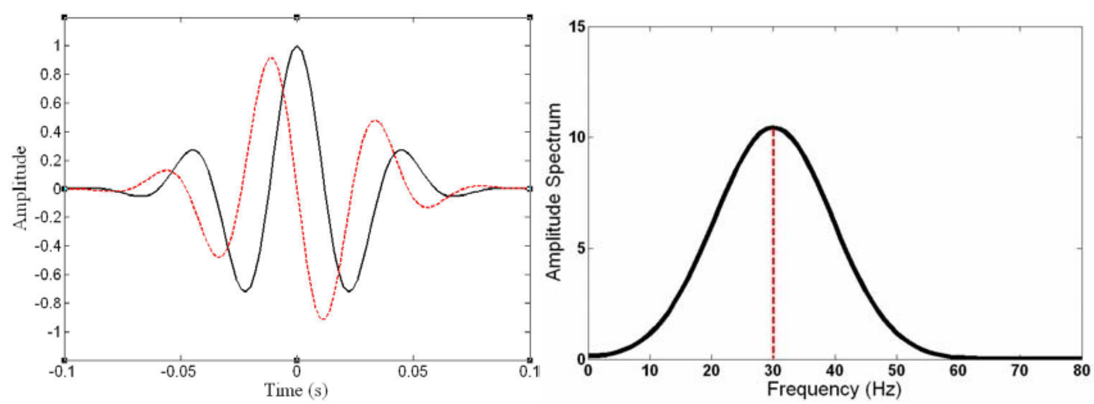

(a) (b)

Figure 2.2 30 Hz Morlet wavelets and corresponding amplitude spectrum. (a) Zero phase Morlet wavelet (black) and 90 degree phase Morlet wavelet (red). (b) Amplitude spectrum of (a).

The analytic analogue of equation 2-1 then becomes

$$U(t) = \sum_j A_j \cdot W(t - t_j, f_j) + Noise, \tag{2-10}$$

where by writing complex amplitude A_j as $a_j e^{i\varphi_j}$, the amplitude a_j in equation 2-1 is represented by the magnitude of A_j, and the phase φ_j is represented by the phase of A_j.

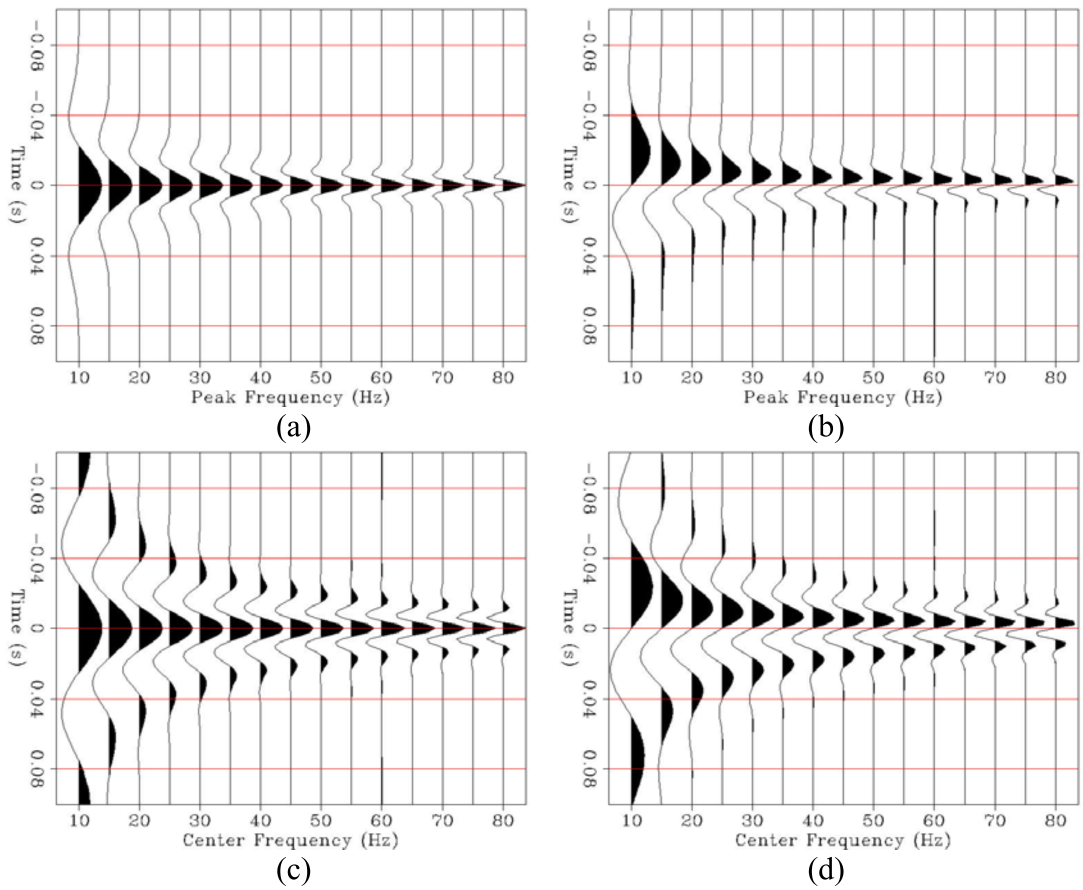

Figure 2.3 The Ricker wavelet dictionary is composed by (a) zero-phase Ricker wavelets and (b) 90 degree phase Ricker wavelets. The Morlet wavelet dictionary is composed by (c) zero-phase Morlet wavelets and (d) 90 degree phase Morlet wavelets. In practice, the wavelets will be sampled at 0.1 Hz rather than the 5.0 Hz increment shown here.

My objective is to minimize the energy of the residual analytic trace, *R(t),* defined as the difference between the analytic seismic trace and the matched wavelets

$$R(t) = \{U(t) - \sum_{1}^{J}[A_j * W(t - t_j, f_j)]\}^2 \ . \tag{2-11}$$

The wavelet coefficients in equation 2-11 are in matrix form and can be obtained by solving the normal equation

$$\mathbf{A} = [\mathbf{W^H W} + \varepsilon \mathbf{I}]^{-1} \mathbf{W^H U} \quad , \tag{2-12}$$

where $\mathbf{U}$ is an n-length vector of all seismic samples in the trace, $\mathbf{A} = (A_1, A_2, ...A_m)$ is an m-length vector of unknown complex wavelet amplitudes, $\mathbf{W}=[W(t,f_1), W(t,f_2), ..., W(t,f_m)]$ is an N by m matrix of wavelets, each row of which corresponds to a wavelet centered at each envelope peak, $\mathbf{I}$ is an $m \times m$ identity matrix and ε is a small number which makes the solution stable. For seismic data, $[\mathbf{W^H W} + \varepsilon \mathbf{I}]^{-1}$ will be a complex-symmetric banded matrix, with the bandwidth proportional to the number of samples used to define the lowest frequency wavelet used, and therefore amenable to efficient solution. I display a graphical image of equation 2-11 which is illustrated in Figure 2.4 where the black lines are the real part of complex values (the complex trace or complex wavelets), and the red lines represent the imaginary part.

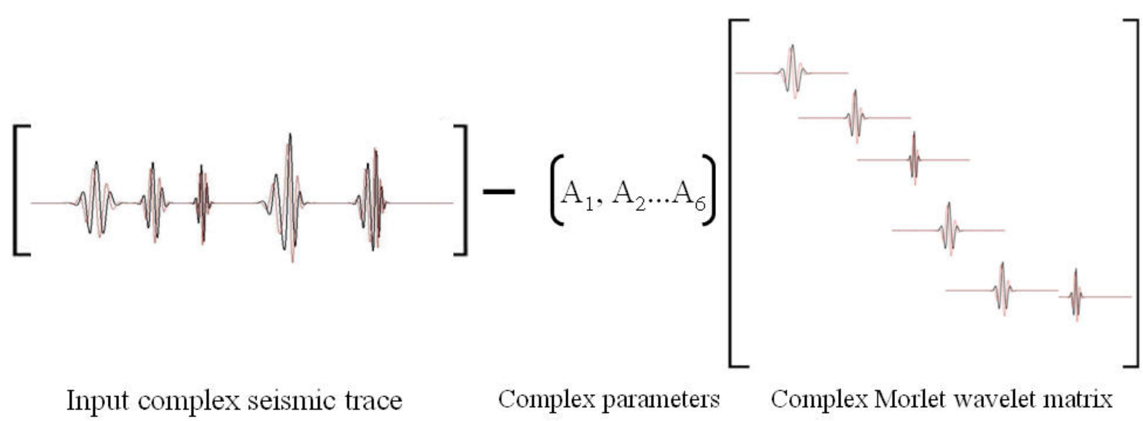

Figure 2.4 Complex matrixes and their geophysical meaning. (Black line means the real part and red line means the imaginary part of complex values)

To obtain improved time-frequency resolution, I locally scan for an improved peak frequency and wavelet center time location. Brute force scans over all times and frequencies are key components of conventional matching pursuit algorithms. In my implementation, I only need to perform a residual search over a user-defined range of frequencies and time samples about the pre-computed peak frequency and peak envelope time to obtain the wavelet frequency-time pair that best cross-correlates with the data. For instance, I can search the frequency range 20 Hz around the pre-computed peak frequency and 20 ms around the time location of wavelet. I will use this 'best' wavelet in the subsequent least-squares complex amplitude calculation. The same process will be repeated for the next iteration. These extra scanning steps increase the run time but result in a better time frequency distribution.

Using equations 2-5 or 2-7, I compute the complex spectrum by summing the complex spectrum of the constituent wavelets

$$\bar{u}(t,f)=\sum_{j=1}^{J}A_j\cdot\bar{w}_j(f,f_j)\mathrm{env}[w(t-t_j,f_j)]e^{i2\pi f(t-t_j)}, \tag{2-13}$$

where

$$\mathrm{env}[w(t-t_j,f_j)]=[w^2(t-t_j,f_j)+w^{H^2}(t-t_j,f_j)]^{1/2} \tag{2-14}$$

is the envelope of the complex wavelets. The amplitude spectrum is thus simply the magnitude of equation 2-13, while the phase is the angle between its real and imaginary parts.

2.3 DECOMPOSITION FLOW

I summarize the decomposition flow in Figure 2.5. After pre-computing the wavelet dictionary, I begin by calculating the instantaneous envelope and frequency for each input trace. I then identify key seismic events by picking a suite of envelope peaks that fall above a user-specified percentage of the largest peak in the current (residual) trace. I have found that this implementation converges faster and provides a more balanced spectrum of interfering thin beds than the alternative ‘greedy’ matched pursuit implementation that fits the wavelet having the largest envelope, one at a time. I interpret such a greedy matching pursuit algorithm as being closer to an L1 minimization process in contrast to fitting all events which would be an L2 fit. I assume that the frequency of the wavelet is approximated by the instantaneous frequency of the residual trace at the envelope peak. The amplitudes and phases of each selected wavelets are computed together using a simple least-squares algorithm, such that the computed amplitudes and phases result in a minimum difference between seismic trace and matched wavelets. Each picked event has a corresponding Ricker or Morlet wavelet. I compute the complex spectrum of the modeled trace by simply adding the complex spectrum of each constituent wavelet. This process is repeated until the residual falls below a desired threshold which is considered as the noise level.

To better illustrate the flow shown in Figure 2.5, I test it on a real seismic trace extracted from 3-D seismic survey acquired on the offshore Louisiana Shelf, Gulf of Mexico, U.S.A. This spectral decomposition example is based on Ricker wavelets. Figure

2.6 represents the input seismic trace and five different iteration modeled traces which include 1st, 2nd, 4th, 8th and 16th iterations. The five different iteration residual traces are shown in Figure 2.7. Figure 2.8 shows the corresponding amplitude spectra of the modeled traces. We can see that after the 16th iteration that the modeled trace is very close to the original input trace, and the residual trace is quite small and can be considered as at or below the noise level.

The Fortran90 spectral decomposition using least-squares algorithm is called "*spec_cmp*". The UNIX "man page" of this algorithm is provided as Appendix B.

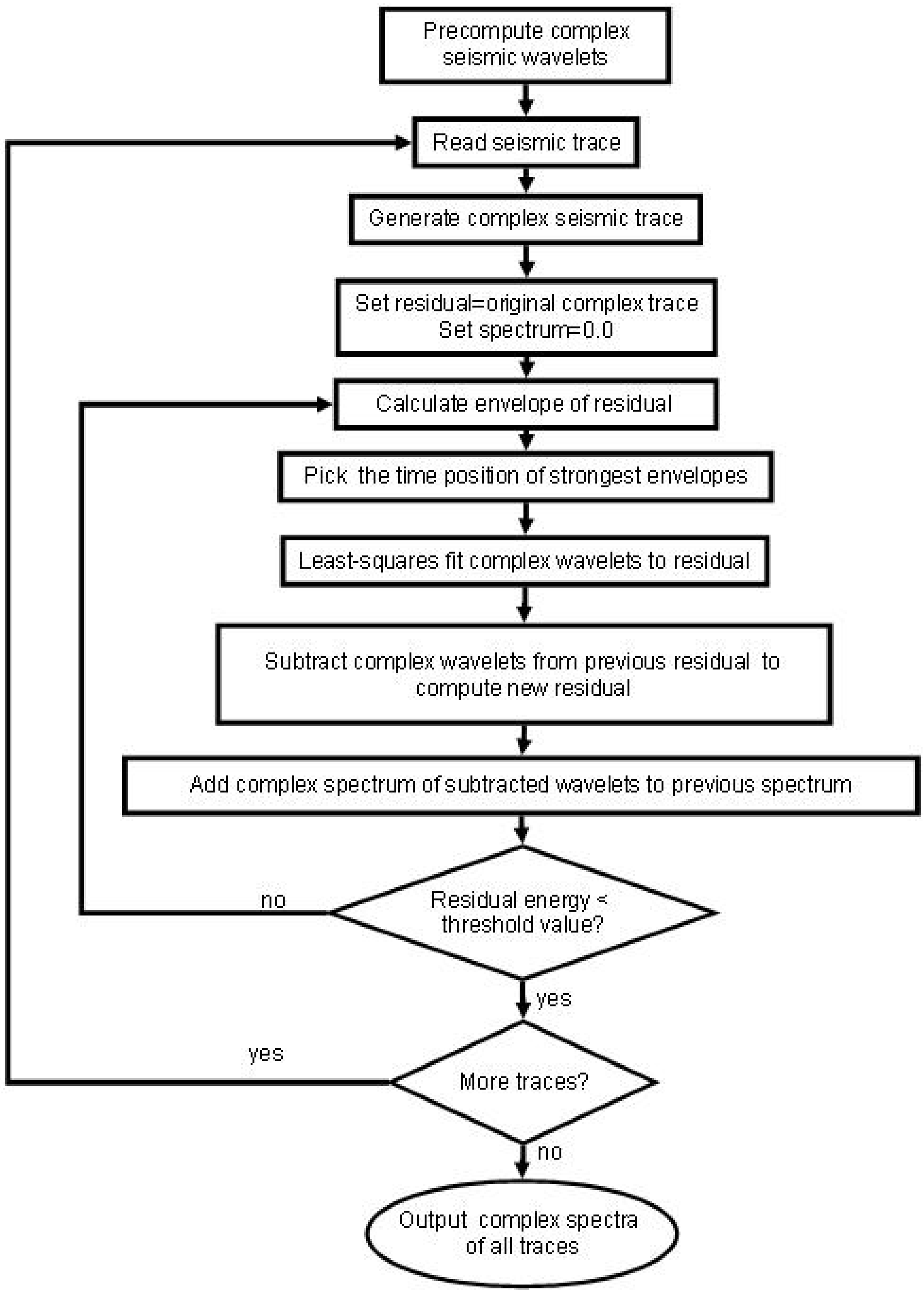

Figure 2.5 The flowchart for spectral decomposition using least-squares.

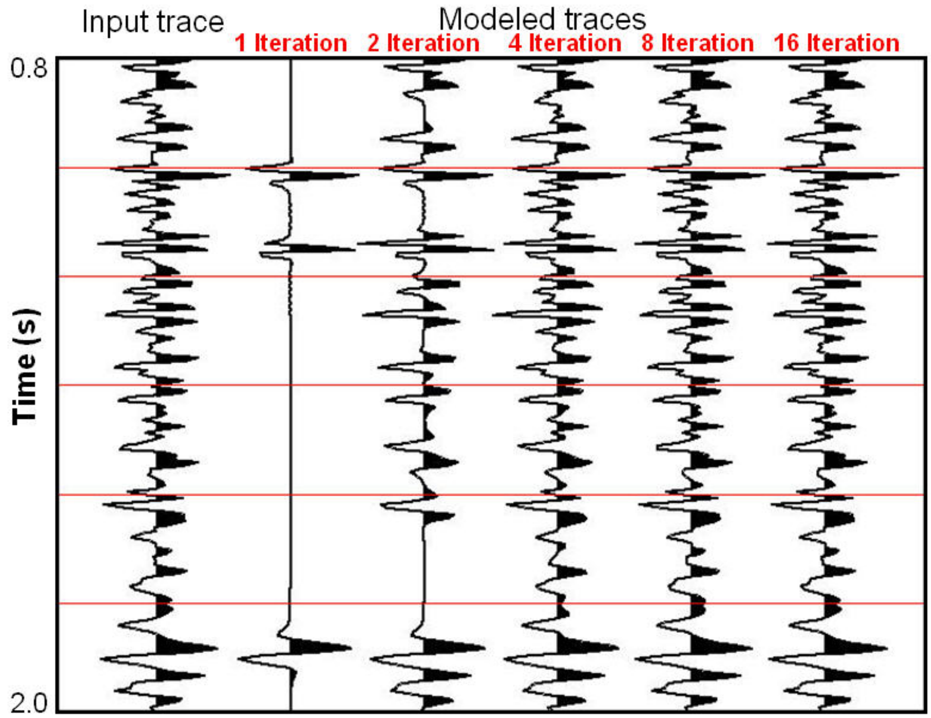

Figure 2.6 Input seismic trace and modeled traces of different iterations.

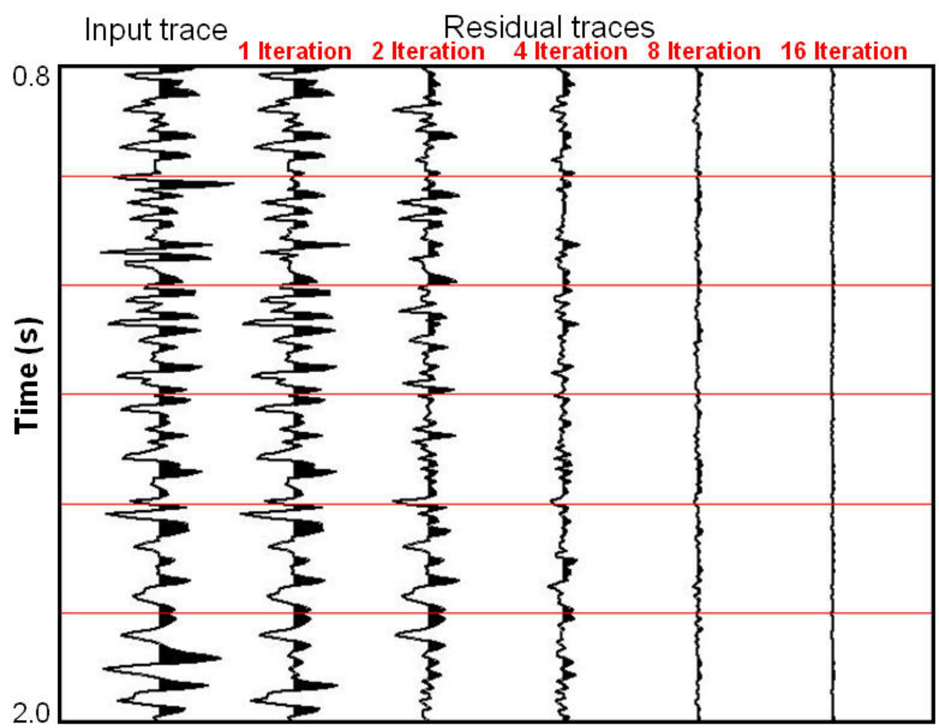

Figure 2.7 Input seismic trace and residual traces of different iterations.

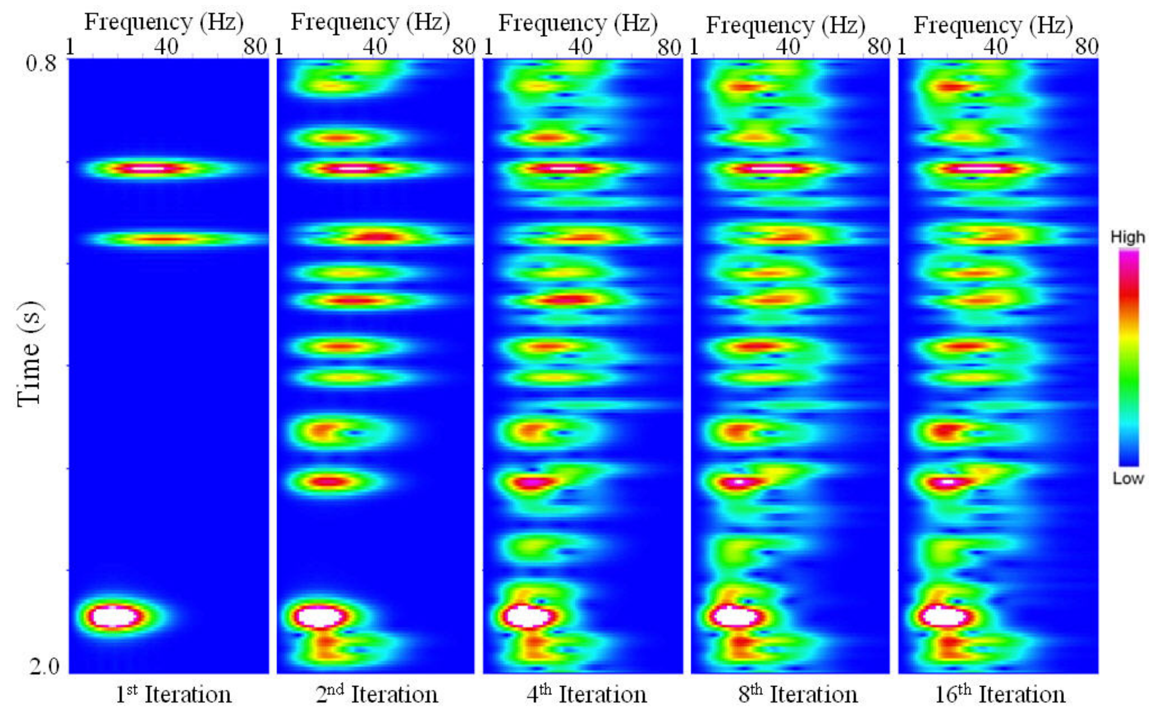

Figure 2.8 Amplitude spectra of different iterations corresponding to the modeled traces shown in Figure 2.6.

2.4 DECOMPOSITION EXAMPLES

I generated the single synthetic trace shown in Figure 2.9 to test the spectral decomposition algorithm using least-squares. The source wavelets used to generate this synthetic are 10 Hz, 30 Hz and 50 Hz Morlet wavelets with phase angles of 0^o, 45^o and 90^o. All the wavelets have the same amplitude. Figure 2.10 shows the modeled or reconstructed trace as well as the original trace. The residual trace in this figure is the difference between the original trace and the modeled trace. From Figure 2.10, we see that this spectral decomposition method provides a good match for well-separated wavelets. For composite wavelets such as at time 1.2 s, my approach still shows a good match even though it has some errors. Intuitively, I expect the decomposition to work best if the real wavelets are similar to the wavelets that compose the wavelet dictionary. Once I have extracted all the matched Morlet wavelets, it is very easy to calculate the time-frequency distribution of the seismic trace, which I show in Figure 2.11.

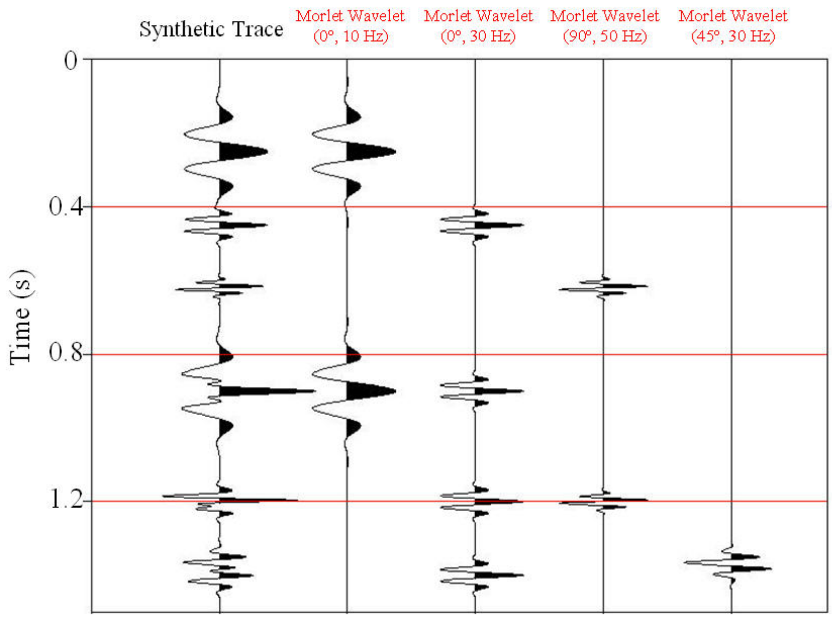

Figure 2.9 Synthetic traces composed by Morlet wavelets with different phases and mean frequencies.

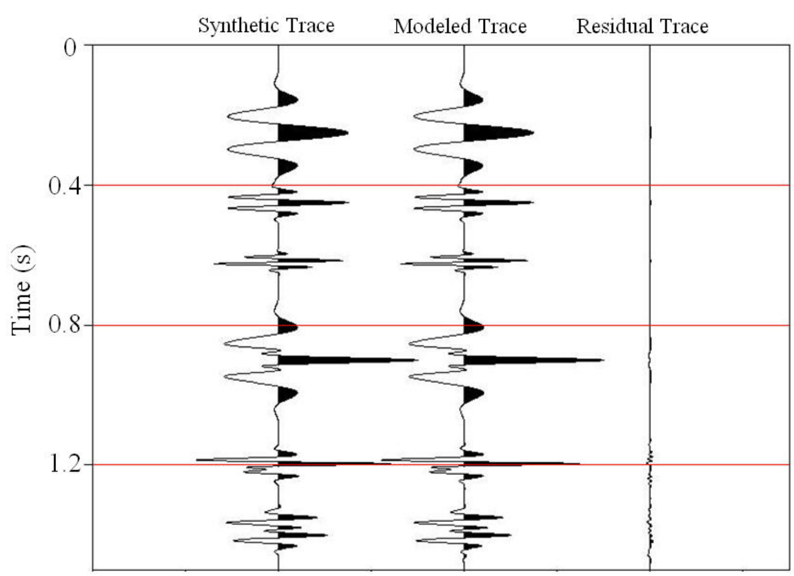

Figure 2.10 Modeled trace and residual trace obtained using the least-squares algorithm.

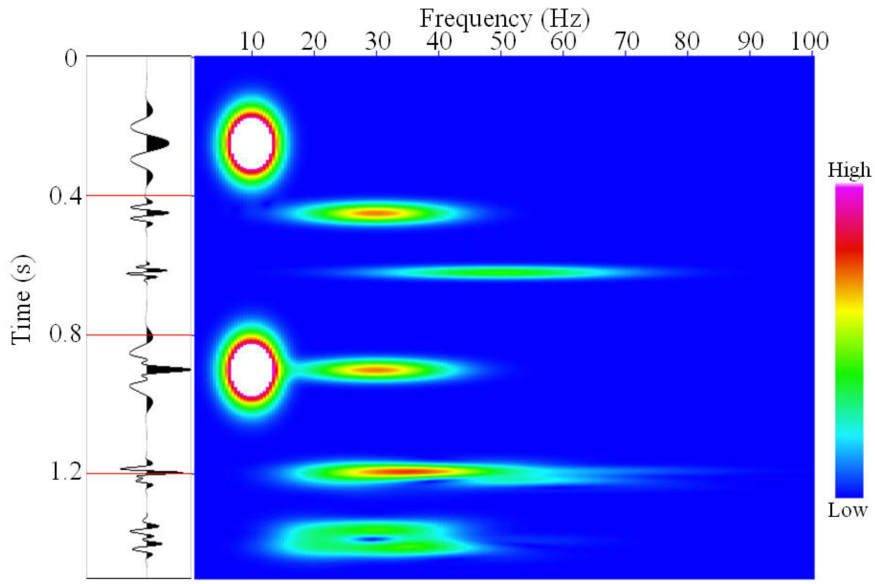

Figure 2.11 Time-frequency distribution of the synthetic trace shown in Figure 2.10.

Fitting a synthetic trace generated using the same wavelet dictionary which is used to fit it is the simplest problem. In general, real seismic source wavelets will not be exactly represented by any pre-computed wavelet dictionary. In addition, since I have two different wavelet dictionaries to do spectral decomposition, I also need to determine if the resulting spectra are similar. For this reason, in Figure 2.12a I extract a real seismic trace from the offshore Louisiana survey discussed above. The Ricker wavelet based and Morlet wavelet based spectral decomposition spectra are shown in Figures 2.12b and 2.12c. Comparing Figures 2.12b and 2.12c, we can see that the Morlet wavelet decomposed spectrum has a similar decomposition spectrum as the Ricker wavelet, but has broader temporal extension than the Ricker wavelet decomposed spectrum (based on the Morlet wavelet defined by equation 2-6). If we go back to Figure 2.3, we note that the Morlet wavelet has a longer time-domain envelope than the corresponding Ricker wavelet with the same mean frequency. In section 2.2, I represented the time variation of the spectrum by the envelope of the matched wavelet. Thus, the Morlet wavelet based time-frequency distribution has a longer temporal spread than that computed using the Ricker wavelet. One way to determine which wavelet dictionary is best is to examine the rate of convergence. I therefore plot the residual energy for each iteration in Figure 2.13. In this decomposition test I used a 'greedy' implementation of the matching pursuit technique, whereby each iteration only subtracts one wavelet from the seismic trace. From Figure 2.13, we note that the Ricker wavelet based spectral decomposition and Morlet wavelet based spectral decomposition have similar residual energy and rates of convergence for this input seismic trace.

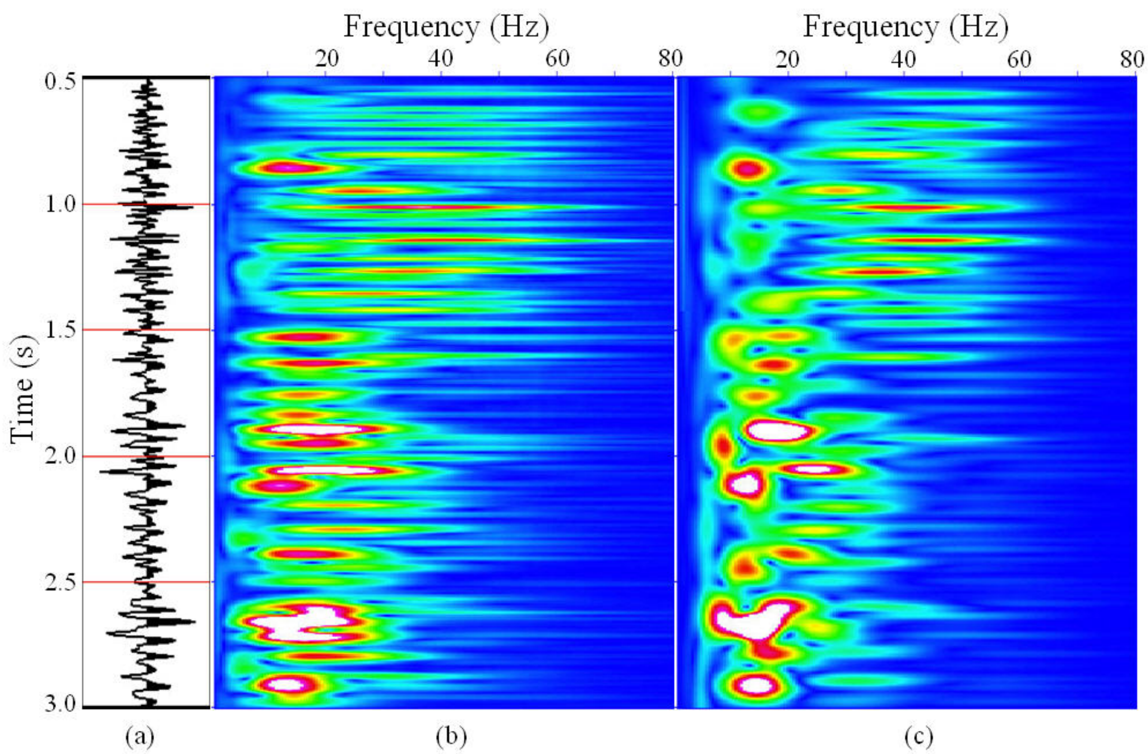

Figure 2.12 The comparison of spectral decomposition results using different wavelet dictionaries. (a) Input seismic trace, (b) the decomposed spectrum using Ricker wavelets, and (c) the decomposed spectrum using Morlet wavelets.

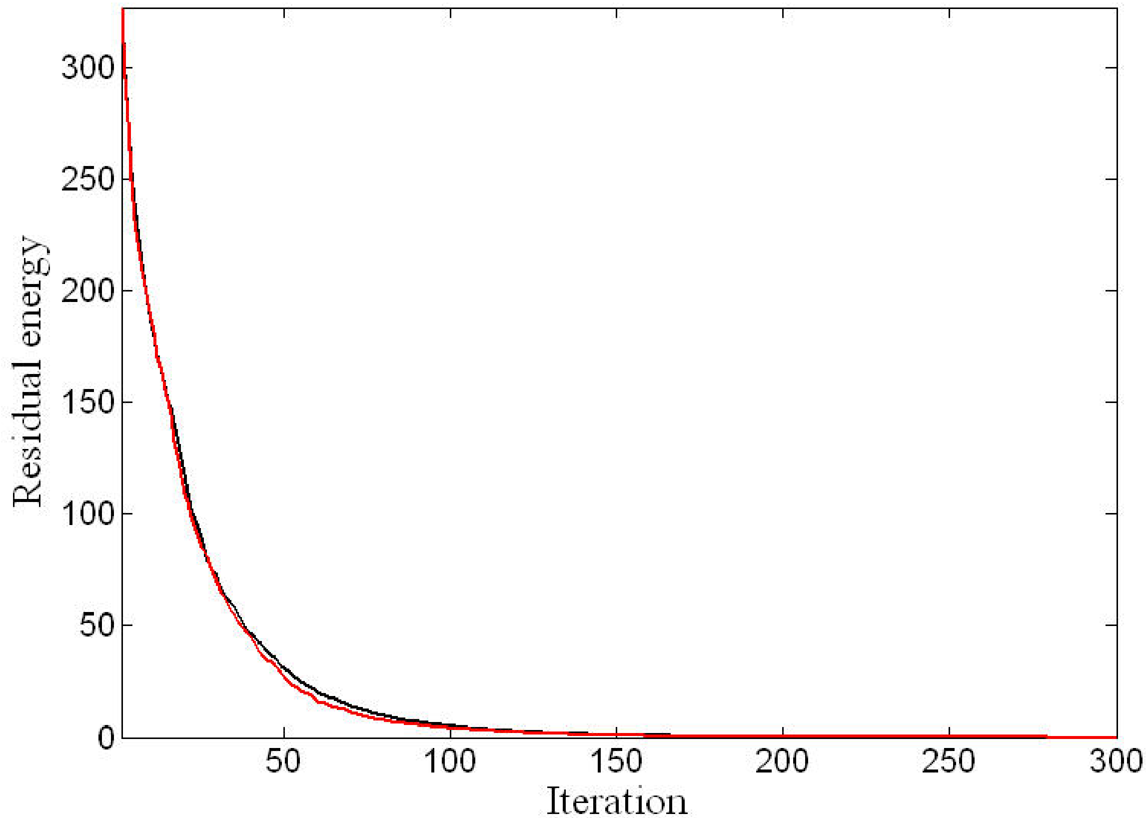

Figure 2.13 The residual energy of each iteration. (Black line is Ricker wavelet, red line is Morlet wavelet)

I now apply spectral decomposition to a seismic line extracted from a 3D survey acquired over the Central Basin Platform, West Texas, U.S.A. At each iteration, I generate the corresponding seismic wavelets and add them to the previously modeled data (Figure 2.14a), compute a new data residual (unmodeled data) (Figure 2.14b), and accumulate the complex spectrum, the 40-Hz component of which I display in Figure 2.14c. The amplitude and time of the chosen wavelets are displayed in Figure 2.14d. Figure 2.14 only shows 3 different iterations, 1st iteration, 4th iteration and 16th iteration. I can continue the iteration process until the final residue is below a user defined threshold value.

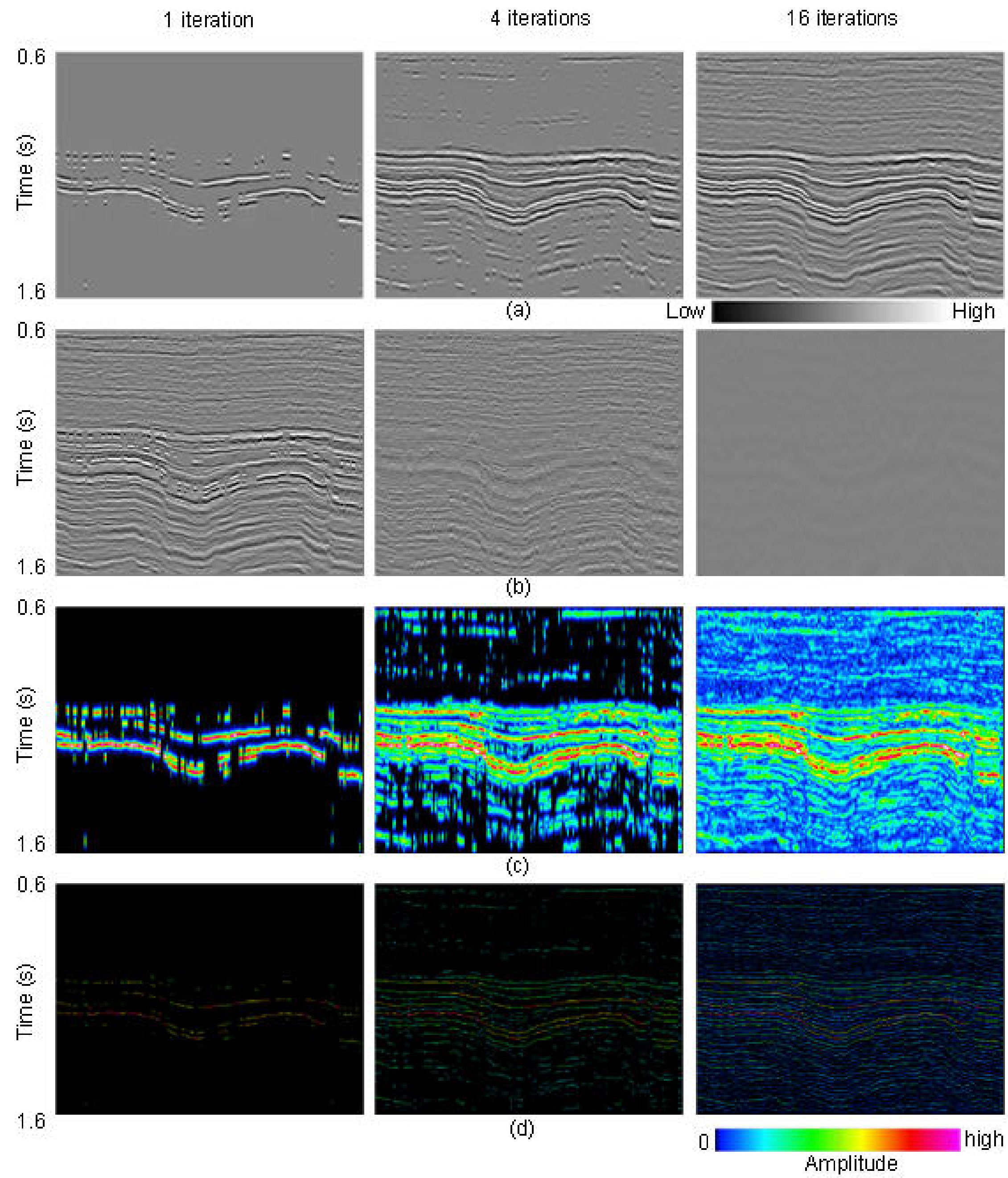

Figure 2.14 Illustration of the spectral decomposition using least-squares applied to a survey acquired over the Central Basin Platform, west Texas, U.S.A. Columns represent algorithm results after the first, fourth, and 16th iteration of (a) modeled data, (b) residual (unmodeled) data, (c) the 40-Hz component of the modeled data, and (d) the wavelet location and envelope of the modeled data. The peak frequency and phase of the modeled wavelets are not displayed. (Data courtesy of Burlington Resources)

2.5 SPECTRAL BALANCING

If the seismic data have not been previously spectrally balanced, it is common practice to do so within the spectral decomposition algorithm. Following Partyka *et al.* (1999), I assume that reflectivity has a white spectrum and balance the spectrum within a user-defined bandwidth as shown in Figure 2.15. Spectral balancing accounts for a non-flat source spectrum as well as changes in the source wavelet with depth. The average amplitude spectrum over the entire survey at a given time before balancing is shown in Figure 2.15a. The balanced average amplitude spectrum is displayed in Figure 2.15b. If I define the average spectrum as $<\alpha(f)>$ which is a function of frequency f, and its maximum, as $\alpha_{\max}$, I estimate a noise level as a fraction, ε, of the peak spectral amplitude. Then I rescale each spectral component by $1/[<a(f)>+\varepsilon \cdot a_{\max}]$ thereby obtaining a 'balanced' average amplitude spectrum. Figure 2.16 shows the average spectra before spectral balancing and after spectral balancing for the seismic survey from Louisiana Shelf, for a time range from 0.0 s to 4.0 s. The average spectra at three different time locations 1.0 s, 2.0 s, and 3.0 s are shown in Figure 2.17. Balancing the median rather than the mean spectrum has been found to provide better results in the presence of bright spots (Partyka, personal communication). Such spectral balancing is important for isolating tuning effects (such as the peak spectral frequency) of the geology, from that of the input seismic wavelet.

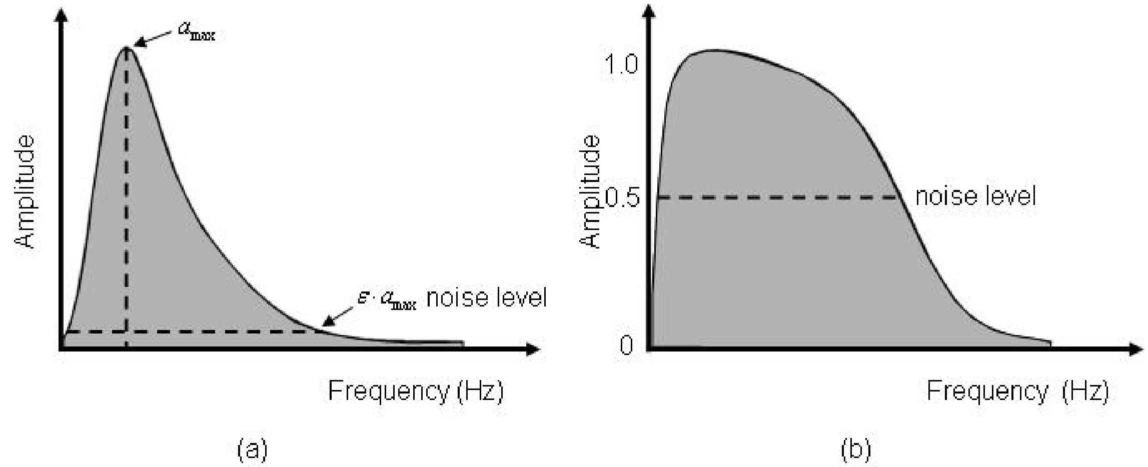

Figure 2.15 Spectral balancing to account for changes in the source wavelet with depth by rescaling each spectral component by $1/[< a(f) > +\varepsilon \cdot a_{max}]$): (a) the average spectrum before balancing, and (b) the average spectrum after balancing.

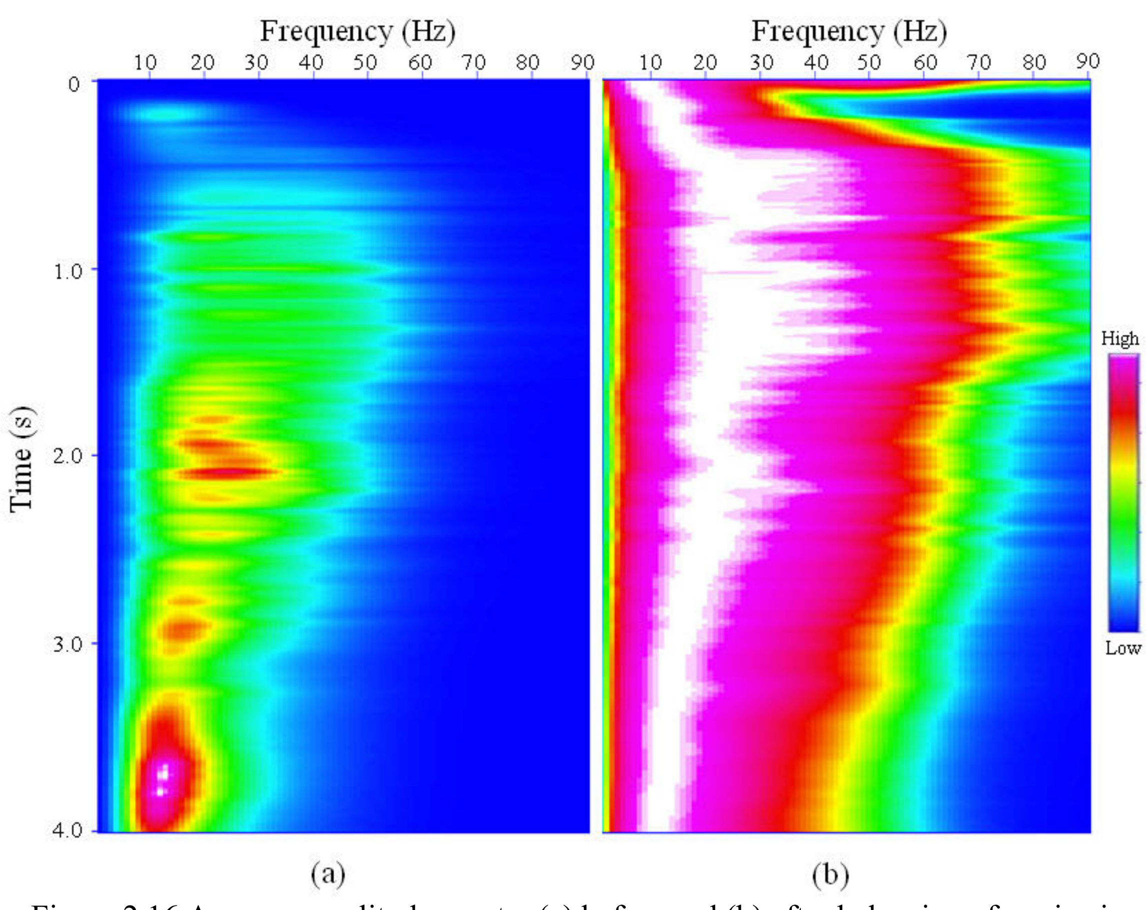

Figure 2.16 Average amplitude spectra (a) before and (b) after balancing of a seismic survey over Louisiana Shelf, Gulf of Mexico.

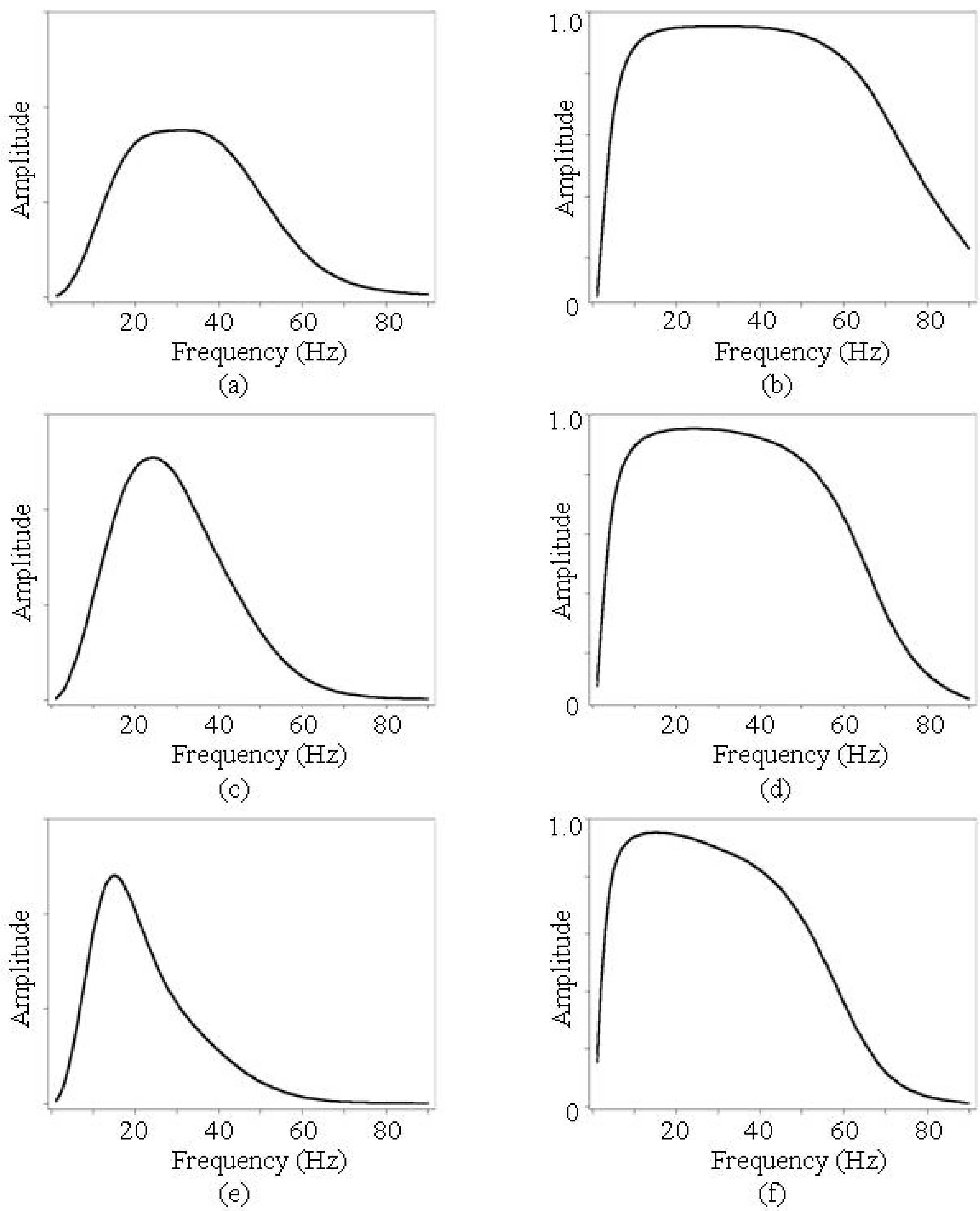

Figure 2.17 Average amplitude spectra at different time locations. (a), (c) and (e) are average amplitude spectra at time 1.0 s, 2.0 s and 3.0 s before spectral balancing; (b), (d) and (f) are average amplitude spectra at time 1.0 s, 2.0 s and 3.0 s after spectral balancing.

Once balanced, I can animate through time or horizon slices of discrete spectral components, interpret selected volumes of discrete spectral components, or alternatively, generate composite volumes of peak frequency and peak amplitude.

2.6 SUMMARY

I have developed a wavelet-based spectral decomposition technique by combining the matching pursuit and least-squares algorithms. The wavelet dictionary can be Ricker, Morlet or other wavelets. Not surprisingly, when the real seismic wavelet is similar to the wavelet dictionary used, the method gives a good decomposition result. By using the envelope and response frequency of complex trace analysis, I can greatly accelerate the matching pursuit algorithms. Using least-squares allows me to simultaneously solve for coefficients of wavelets having comparable amplitudes that overlap. Synthetic and field examples show that this new spectral decomposition method yields good time frequency distributions.

CHAPTER 3

MULTI-COLOR DISPLAY OF SPECTRAL ATTRIBUTES*

3.1 INTRODUCTION

Current spectral decomposition techniques typically generate a suite of tightly sampled instantaneous spectral attribute volumes (Castagna *et al.*, 2003; Liu and Marfurt, 2005; Partyka *et al.*, 1999). While there is useful information in these instantaneous spectral attribute volumes, it is not easy for seismic interpreters to inspect each one of them individually. Typical volumetric analysis will generate between 10 and 100 output volumes of both magnitude and phase, which can easily fill up the limited disk space available on an interpretation workstation. As a partial solution to this challenge, Liu and Marfurt (2005) combined peak frequency and peak amplitude to highlight channel systems.

In this chapter, I will discuss three different display techniques to delineate subtle depositional and structural patterns. The first technique simply animates through single frequency volumes and is the simplest way to show spectral variation. The second technique is a composite plot of peak frequency, peak amplitude and coherence using a

* Jianlei Liu and Kurt Marfurt, to appear in The Leading Edge

hue-lightness-gray colormap that is able to delineate both lateral discontinuities and vertical changes in thickness in a single image. The advantage of such a composite image is that the peak frequency is sensitive to thin bed vertical thickness variations, while coherence is sensitive to lateral discontinuities. The analogous composite plot of phase (rather than amplitude) at peak frequency can also highlight stratigraphic and structural features. While several workers have co-rendered three spectral components by plotting them against Red-Green-Blue (RGB) color model components, the optimum choice of these frequencies is not clear. For the third display technique, I partially circumvent this problem by using RGB to display the coefficients of three predetermined basis functions. When added together, these coefficient-weighted basis functions approximate the computed spectrum in a least-squares sense. This display method provides moderate details of the full amplitude spectrum. More importantly, instead of outputting 100 different single spectral components, I can output a single RGB volume. Onstott *et al.* (1984) firstly introduced the "ColorStack" which used RGB to plot near-, mid-, and far-offset seismic data. Stark (2006) used a similar RGB plotting technique, which assigns the average amplitude of three non-overlapping spectral bands to RGB rather than the somewhat more continuous, overlapping spectral bands that I will use. I use ocean bottom data from the Louisiana Shelf, Gulf of Mexico to illustrate the value of the three display techniques to convey the spectral information.

3.2 PLOTTING TECHNIQUES

Spectral attributes can be viewed in different ways. I will list three different methods to plot spectral attributes. After time-frequency decomposition, a single 3D seismic volume is decomposed into a suite of single frequency 3D volumes (or alternatively, a 4D volume). Since most seismic interpretation software is designed to analyze 3D data volumes, the most common interpretation method is either to directly view one single spectral component at a time, or alternatively, to interleave spectral components along a horizon slice and interpret the spectra as a new 3D volume with x, y, and f axes through which I animate.

The second method is to represent the spectrum with a few statistically important parameters. I find that composite volume of peak frequency (or alternatively, the phase at peak frequency), peak amplitude (or peak amplitude above average amplitude) and coherence attributes to be particularly useful. Other workers propose estimating the spectrum by its bandwidth and kurtosis, though I have seen little published in this area. However they are computed, the main advantage of a composite plot is that I only have one 3D composite volume to investigate. Coherence attributes can detect the structural discontinuities while the peak frequency can predict vertical variations in thickness.

The third plotting method of representing 100 or more spectral components is to use Red-Green-Blue (RGB) to display sub spectral estimates of the data using predetermined basis functions. The following is the detail of RGB plotting. I first define three different basis functions which represent Red, Green and Blue (RGB) functions (Figure 3.1). I have chosen three simple raised cosine basis functions with well-defined center frequencies.

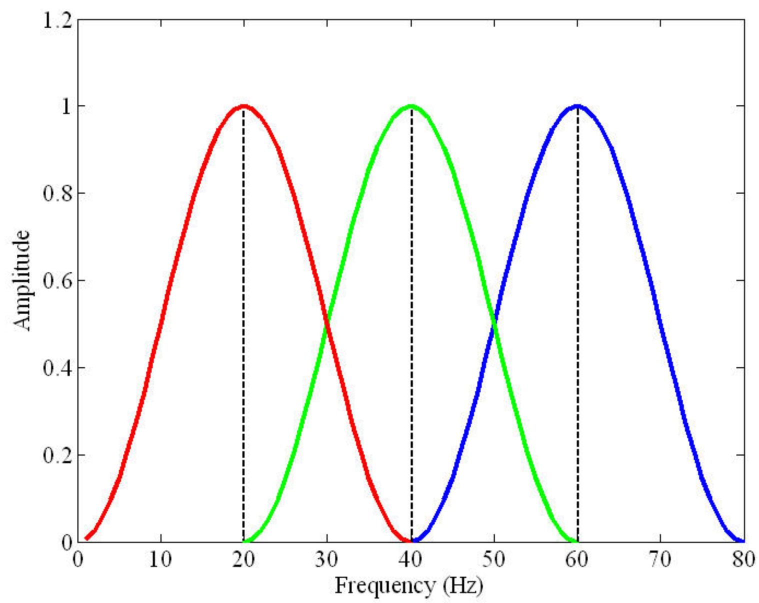

Figure 3.1 Red, Green and Blue basis functions.

The equations I used to describe RGB functions are

$$b_R(f) = 0.5 \cdot (1.0 + \cos(\pi \frac{f - f_R}{k \cdot f_{Bandwidth}})) \quad , \tag{3-1}$$

$$b_G(f) = 0.5 \cdot (1.0 + \cos(\pi \frac{f - f_G}{k \cdot f_{Bandwidth}})) \quad , \tag{3-2}$$

$$b_B(f) = 0.5 \cdot (1.0 + \cos(\pi \frac{f - f_B}{k \cdot f_{Bandwidth}})) \quad , \tag{3-3}$$

where $b_R(f)$, $b_G(f)$, and $b_B(f)$ are Red, Green and Blue basis functions, respectively, f_R, f_G, and f_B are the center frequencies for Red, Green and Blue basis functions, $f_{Bandwidth}$ is the frequency bandwidth of the input seismic data, and k is a constant value which controls the bandwidth of the basis functions. From equations 3-1, 3-2 and 3-3, we can define different RGB functions when we provide different RGB center frequencies and bandwidth values.

After I define the three RGB basis functions, I can use least-squares solutions to match the three basis functions to the amplitude spectrum at each time location which is decomposed by spectral decomposition methods. The objective is to minimize the residual energy between amplitude spectrum and the RGB basis functions. The residual energy is defined as

$$R(f) = \{u(f) - [c_R b_R(f) + c_G b_G(f) + c_B b_B(f)]\}^2 \ , \tag{3-4}$$

where $R(f)$ is the residual energy, $u(f)$ is the amplitude spectrum, c_R, c_G, and c_B are the three coefficients corresponding to Red, Green and Blue basis functions, and f is the frequency. I write these three basis functions as a $m \times 3$ matrix, $\mathbf{B}$, where

$$\mathbf{B} = \begin{bmatrix} b_R(f_1) & b_G(f_1) & b_B(f_1) \\ b_R(f_2) & b_G(f_2) & b_B(f_2) \\ \cdots & \cdots & \cdots \\ b_R(f_m) & b_G(f_{m1}) & b_B(f_m) \end{bmatrix} \ , \tag{3-5}$$

and the coefficients and spectral components as vectors $\mathbf{C} = \begin{pmatrix} c_R \\ c_G \\ c_B \end{pmatrix}$, and $\mathbf{U} = \begin{pmatrix} u(f_1) \\ u(f_2) \\ \ldots \\ u(f_m) \end{pmatrix}$,

then the least-squares solution of $\mathbf{C}$ will be

$$\mathbf{C} = [\mathbf{B}^{\mathbf{T}}\mathbf{B} + \boldsymbol{\varepsilon}\mathbf{I}]^{-1}\mathbf{B}^{\mathbf{T}} \cdot \mathbf{U} \quad , \tag{3-6}$$

where $\mathbf{I}$ is a 3×3 identity matrix and ε is a small number which makes the solution stable.

After solving equation 3-6, I map the three coefficients corresponding to Red, Green and Blue basis functions directly against Red, Green and Blue in readily-available display algorithms. Figure 3.2 demonstrates the least-squares fit coefficients of the three basis functions of an instantaneous frequency amplitude spectrum (Black line). The maximum amplitude values of Red, Green and Blue dash-lines correspond to the RGB coefficients, c_R, c_G, and c_B. Figure 3.3 shows an example of the RGB plot applied to a single synthetic trace. Figure 3.3b is the time-frequency distribution of the input synthetic trace shown in Figure 3.3a. Figure 3.3c is the least-squares fit of the RGB basis function of the time-frequency distribution shown in Figure 3.3b. Figure 3.3d is the final RGB plot of the three RGB coefficients displayed in Figure 3.3c. By exploiting the well-established color mixing model, it is easy for an interpreter to associate red with a lower frequency, green with a middle frequency, and blue with a higher frequency. Likewise, most interpreters know that cyan falls between blue and green, yellow between green and red, and then a bi-modal spectrum of low and high frequencies will appear as magenta. Flat spectra will appear as shades of gray. Least-squares RGB plots have the same advantage as composite plots of peak frequency and peak amplitude. Based on the decomposed time-frequency distributions, I can represent the gross spectral behavior with a single multi-attribute display. For more details, we still need to look through the single frequency volumes.

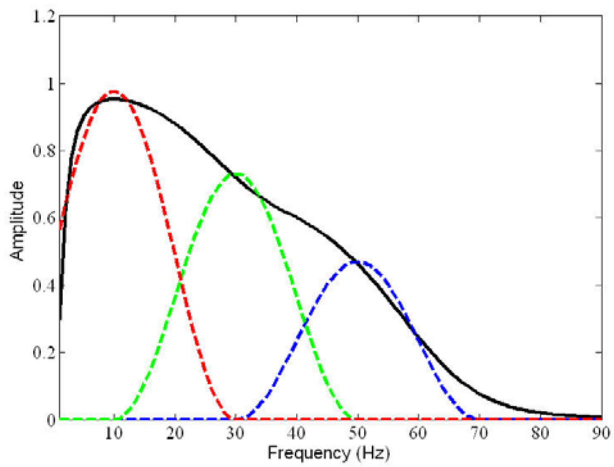

Figure 3.2 Red, Green and Blue coefficients calcuated by least-squares fit with instatneous frequency distribution.

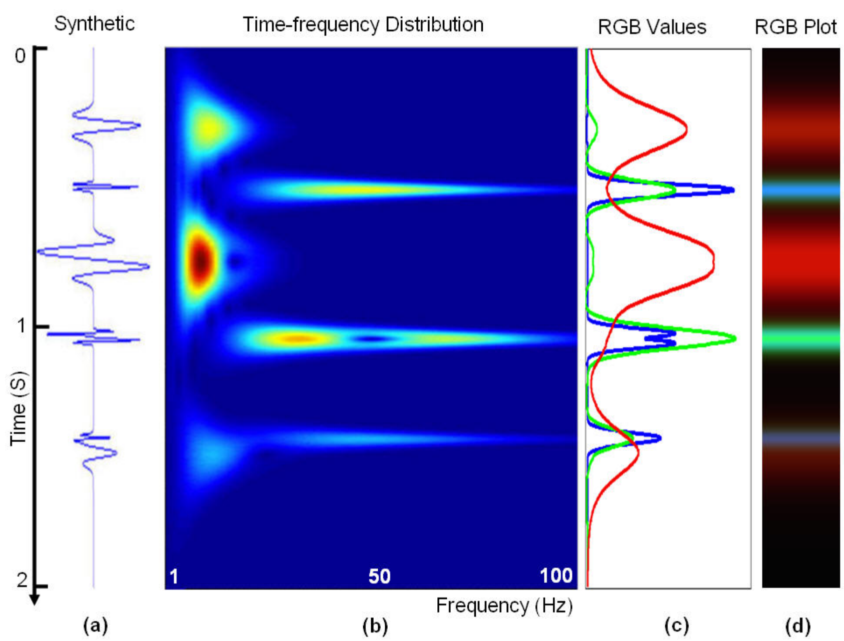

Figure 3.3 (a) Synthetic trace; (b) time-frequency distribution of (a); (c) Red, Green and Blue coefficients of least-squares fit of (b); (d) RGB plot of (c).

3.3 FIELD DATA EXMAPLES

The field data used for color displays is from the Louisiana Shelf, Gulf of Mexico, U.S.A.

3.3.1 *Single Frequency Volume Plot*

I use the wavelet based least-squares spectral decomposition method described in Chapter 2 to decompose seismic data into a suite of 80 single frequency volumes ranging between 10 and 90 Hz. Figure 3.4 shows the input seismic volume. The 30 Hz volume in Figure 3.5 is representative of the data quality. A black arrow indicates a meandering channel. Since channels may have different spectral response than the neighboring data points, different single frequency volumes will in general delineate or highlight different thickness channels.

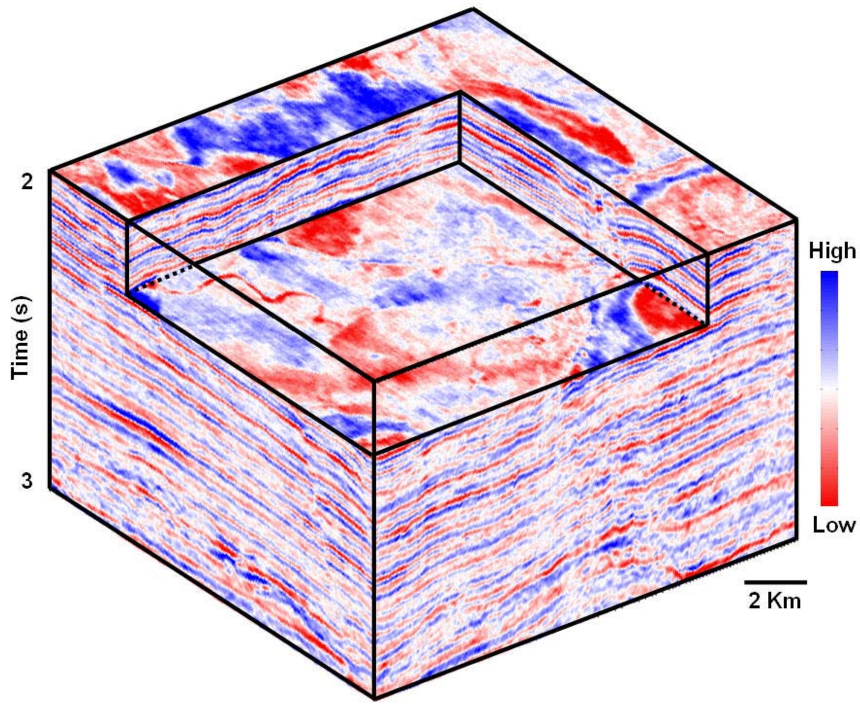

Figure 3.4 Seismic volume. (Seismic data courtesy of Fairfield Industries)

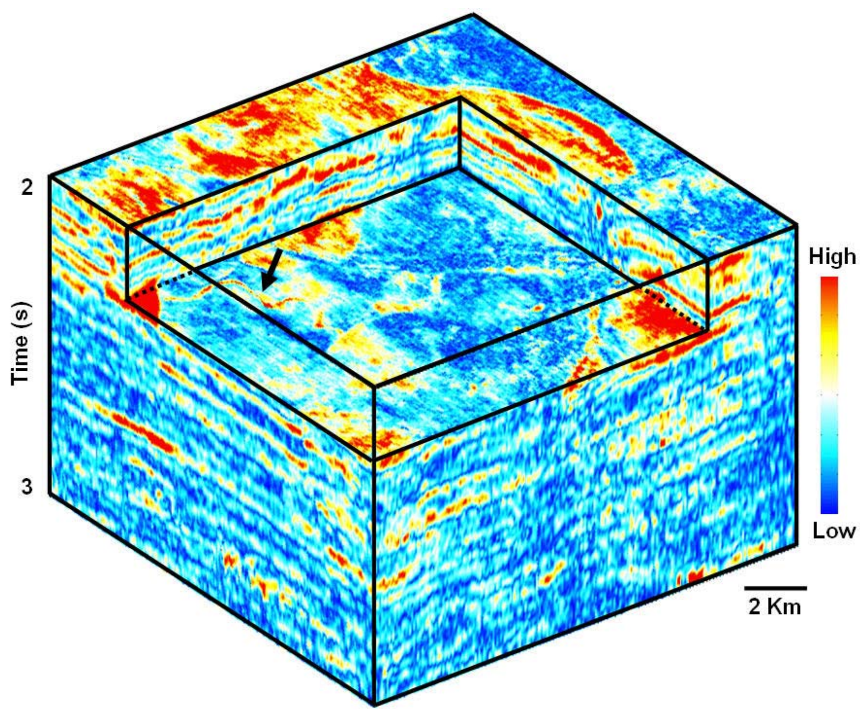

Figure 3.5 Single frequency 30 Hz volume.

3.3.2 *Composite Plot of Spectral Attributes and Coherence*

I will generate two multi-attribute volumes using composite color-maps. The first composite volume is a combination of peak frequency, peak amplitude and coherence attributes. Figure 3.6 shows the work flow used to generate composite volume by combining peak frequency, peak amplitude and coherence attributes (the time slice at 2.220 second). Figures 3.6a, b, and d show time slices of peak frequency, peak amplitude, and coherence. Figure 3.6c is the initial composite slice of peak frequency and peak amplitude. Combining peak frequency and peak amplitudes, we can easily find the frequency variation at strong amplitudes. Figure 3.6e demonstrates the final composite slice of peak frequency, peak amplitude and coherence. The advantage of the composite plot shown in Figure 3.6e is that both structural discontinuities and bed thickness are shown in a single image. Coherence attributes can detect discontinuities, while peak frequency indicates the bed thickness changes. Bright (higher values of lightness) colors indicate a highly tuned (non flat) spectrum. A higher peak frequency (a red hue) indicates a thinner layer, while a lower peak frequency (a blue hue) indicates a thicker layer. The yellow channel indicated by the upper left white arrow in Figure 3.6e is tuned in at 50 Hz. The lower right white arrow points to the fault (Figure 3.6e).

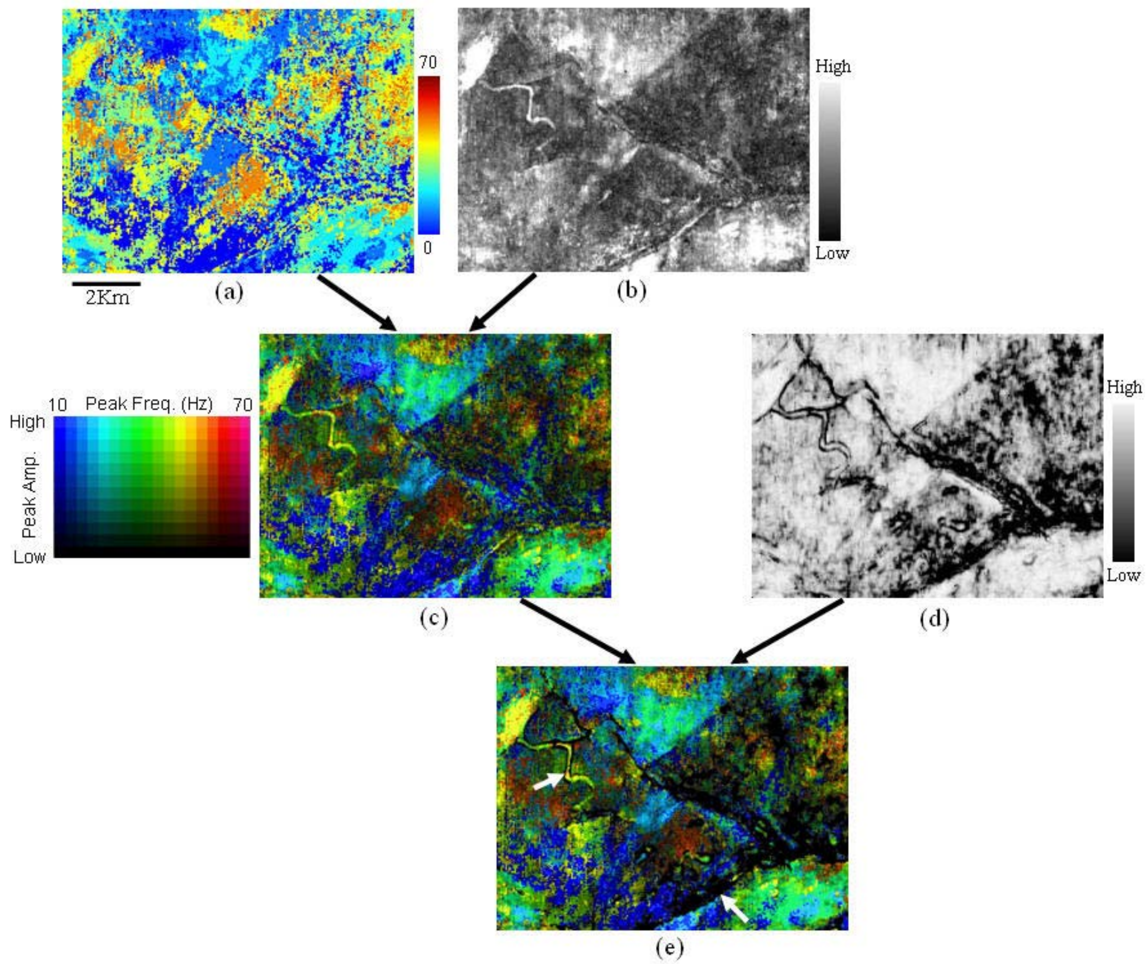

Figure 3.6 Plot showing the composite volume (time slice at 2.220 s). (a) Time slice of peak frequency, (b) time slice of peak amplitude, (c) time slice of composite volume of peak frequency and peak amplitude, (d) time slice of coherence, and (e) time slice of composite volume of peak frequency, peak amplitude and coherence. (Data courtesy of Fairfield Industries)

The second composite volume is a combination of phases at the peak frequency, peak amplitude above background, and coherence attributes. Taner, Koehler and Sheriff (1979) stated that instantaneous phase may indicate discontinuities. After time-frequency decomposition, I also compute a suite of phase as well as amplitude volumes at each frequency. In Figure 3.7 only phases at the peak frequency are used to generate the composite volume. Comparing Figure 3.6e and 3.7, we note that the sinuous channel at the upper left of figures is visible in both figures. Figure 3.7 shows the channel because of the different phase information as compared to the background response, while in Figure 3.6e the channel and background have different frequency tuning.

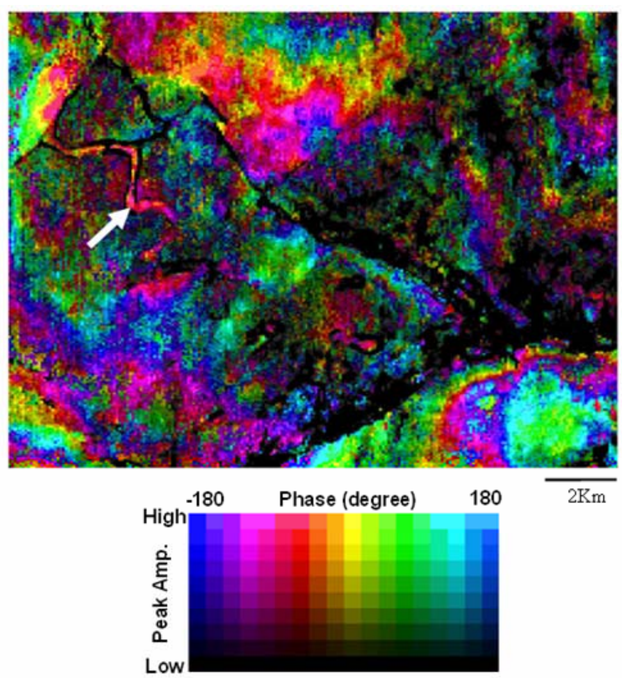

Figure 3.7 Time slice of composite volume of phase at peak frequency, peak amplitude and coherence at 2.220 s. The magenta channel has a -90 degree phase, consistent with thin bed tuning (white arrow).

3.3.3 *Red-Green-Blue Plot*

I am now ready to apply the least-squares Red-Green-Blue basis function technique to the same data volume. Figure 3.8 shows the process of RGB display on a 2-D seismic line. Figure 3.8a shows a vertical section through the seismic data. A red arrow indicates a pay reservoir. The eight single frequency sections shown in Figure 3.8b represent the 70 different frequencies computed between 10 to 80 Hz. The Red-Green-Blue curves which represent three basis functions are shown in Figure 3.8b. After using least-squares fitting on these three different basis functions with decomposed frequency values, I obtain the Red, Green and Blue sections shown in Figure 3.8c, 3.8d and 3.8e. The final RGB plot is given in Figure 3.8f. A white arrow points to the red zone which indicates a low frequency zone. Figure 3.9 displays the time slice of RGB plot at 2.220 s. It is clear to see that the channel (cyan) has a different frequency response compared to background frequency response.

Fortran90 program *generate_ppm,* generates the RGB plotting format file based on three input Red, Green and Blue files. I provide the UNIX 'man page' of this algorithm as Appendix C.

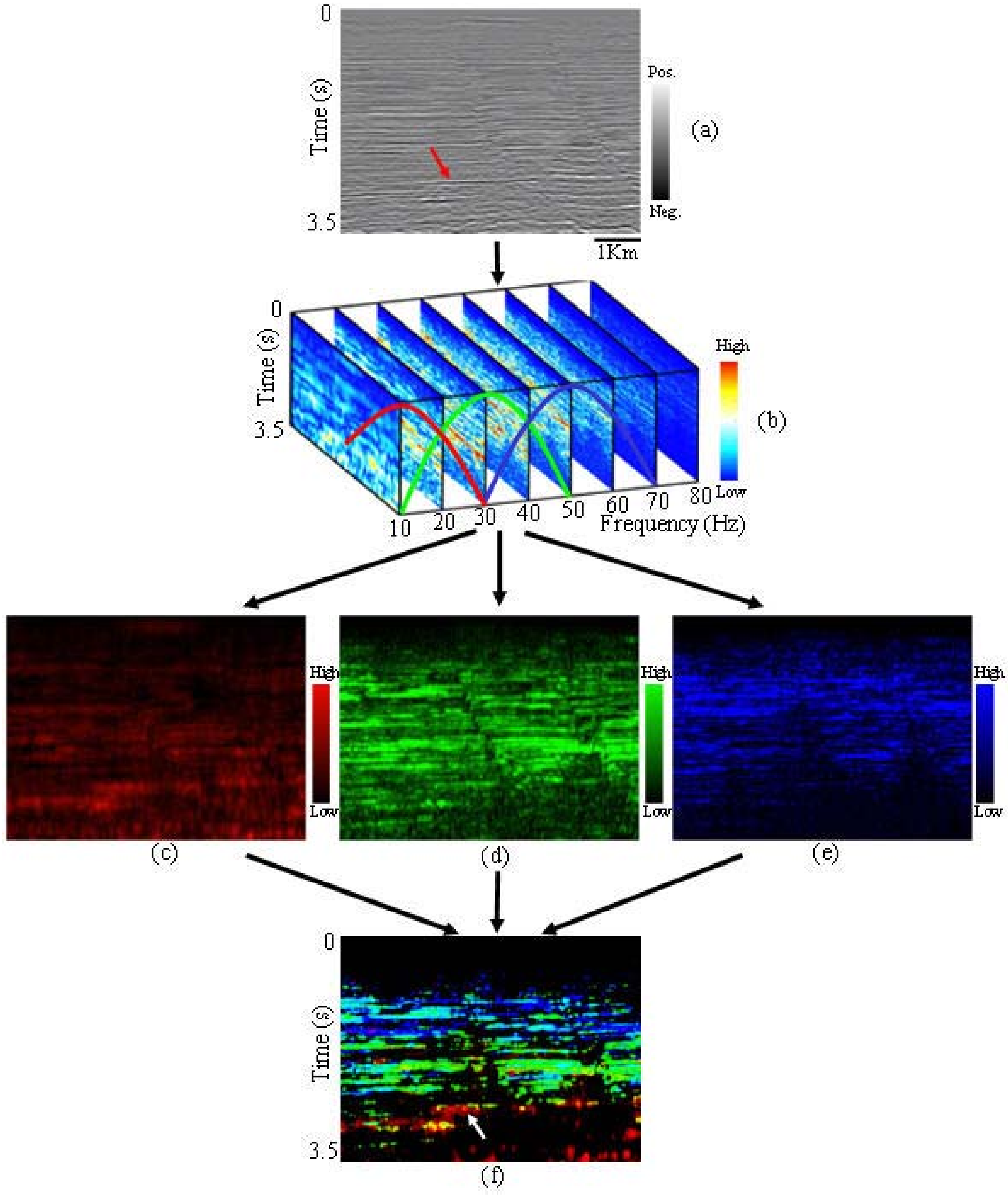

Figure 3.8 Red-Green-Blue plotting technique. (a) Seismic section; (b) single frequency slices; (c) , (d) and (e) are Red, Green and Blue values calculated by three basis functions; (f) RGB plot of (c), (d) and (e). (Data courtesy of Fairfield Industries)

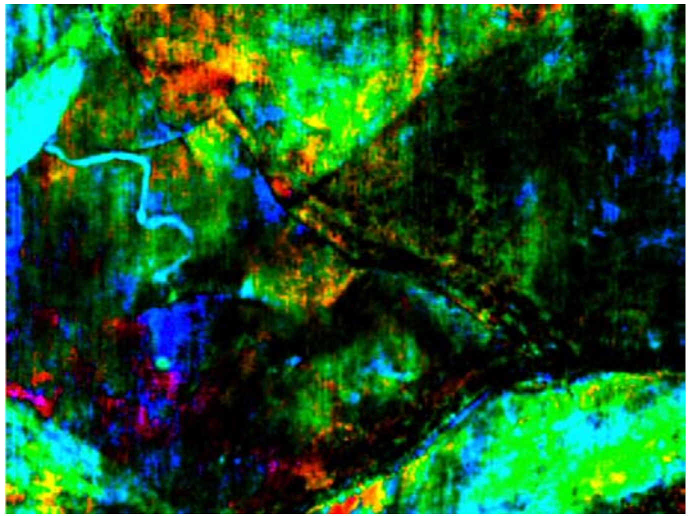
Figure 3.9 Time slice of Red-Green-Blue plot at 2.220 s.

3.4 SUMMARY

I have applied three different color display techniques to a suite of 80 spectral components in an attempt to summarize key information in a single image. The direct color plot of single frequency volume is the simplest way to view decomposed frequency attributes, but given time constraints, it is generally infeasible for a seismic interpreter to view all the frequency volumes for more than a few horizons of interest. The alternative composite color display of peak frequency, peak amplitude and coherence can highlight the discontinuities and thickness variation. The third Red-Green-Blue plot can represent the general frequency changes of seismic data. Both the composite color plot and the RGB plot can save time for the seismic interpreter when viewing spectral attributes quickly and can be considered as the first step when displaying instantaneous spectral attributes.

CHAPTER 4

THIN BED THICKNESS PREDICTION USING PEAK INSTANTANEOUS FREQUENCY

4.1 INTRODUCTION

Widess (1973) showed that we can estimate the thickness of a thin layer (one whose thickness is less than ¼ wavelength, or the tuning thickness) by exploiting the linear relation between thickness and reflection amplitude. In addition, the tuning thickness itself is inversely proportional to the peak spectral frequency of a broadband spectral response. Robertson and Nogami (1984) discussed the combination of envelope and instantaneous frequency to predict thin bed thickness. Chuang and Lawton (1995) studied four different wedge models to show that peak frequency slowly decreases as layer thickness increases. Based on instantaneous attributes (Taner *et al.*, 1979), Partyka (2001) compared Widess's amplitude method simple measurements of peak to trough travel time as well as discrete Fourier transform (spectral decomposition) components to predict thickness. Nissen (2002) demonstrated the relationship between instantaneous frequency and "D" sand thickness of Sooner unit in Colorado. Unfortunately, the instantaneous frequency obtained using complex trace analysis can become unstable and unreliable when seismic data has a low signal-to-noise ratio. Instead, I propose using peak instantaneous frequency to predict thin bed thickness. Peak instantaneous frequency is calculated in a small window which is around the thin bed response. The general concept is that thicker thin bed has lower peak instantaneous frequency, while thinner bed has higher peak instantaneous frequency. I assume that the thin bed reservoir's thickness is less than or around tuning thickness.

In this chapter, I begin with the theoretical formulation for thin bed thickness prediction using the peak instantaneous frequency. Next I construct two simple wedge models to verify the relationship between peak instantaneous frequency and thin bed thickness. Finally I use 3D seismic data from the Fort Worth basin with 16 wells to calibrate this method to predict the thickness of the Pennsylvanian age Caddo limestone. For the field example, I find that the peak instantaneous frequency is well-correlated with the layer thickness measured in the wells which can be used to predict Caddo limestone thickness.

4.2 THEORY OF THIN BED THICKNESS PREDICTION

Instantaneous frequency is the first derivative of instantaneous phase (Taner *et al.*, 1979). It can also be defined as a conditional average frequency in a range of time (Robertson and Nogami, 1984; Barnes, 1993; Cohen, 1995)

$$\bar{f}_i = \frac{\int_0^\infty fA(f)df}{\int_0^\infty A(f)df} \quad , \tag{4-1}$$

where $\bar{f}_i$ is instantaneous frequency in Hz, f is frequency of the spectral component in Hz, and $A(f)$ is the amplitude spectrum.

I can replace $A(f)$ with the thin bed response of a Ricker wavelet $R(f) \cdot W(f)$, where $R(f)$ and $W(f)$ are the spectral components of the reflection series and the Ricker wavelet, respectively. The amplitude spectrum $W(f)$ of a zero-phase Ricker wavelet is

$$W(f) = \frac{2}{\sqrt{\pi}} \frac{f^2}{f_p^3} e^{-(\frac{f}{f_p})^2} \quad , \tag{4-2}$$

where f_p is peak frequency of the Ricker wavelet.

The amplitude spectrum $R(f)$ of the thin bed reflection response is

$$R(f) = \sqrt{r_1^2 + r_2^2 + 2r_1 r_2 \cos(2\pi f \Delta t)} \quad , \tag{4-3}$$

where, r_1 and r_2 are top and bottom reflection coefficients, respectively, and Δt is the two way travel time thickness of the thin bed.

Using equations 4-2 and 4-3, I obtain the final amplitude spectrum $A(f)$

$$A(f) = R(f)W(f) = \frac{2}{\sqrt{\pi}} \frac{f^2}{f_p^3} e^{-(\frac{f}{f_p})^2} \sqrt{r_1^2 + r_2^2 + 2r_1 r_2 \cos(2\pi f \Delta t)} \quad . \tag{4-4}$$

Substituting this expression for $A(f)$ from equation 4-4 into equation 4-1 and assuming that both magnitude of r_1 and r_2 equal to r, I obtain

$$\bar{f}_i = \frac{\int_0^\infty fA(f)df}{\int_0^\infty A(f)df}$$

$$= \frac{\int_0^\infty f \frac{2}{\sqrt{\pi}} \frac{f^2}{f_p^3} e^{-(\frac{f}{f_p})^2} \cdot 2r\left|\sin(\pi f\Delta t)\right| df}{\int_0^\infty \frac{2}{\sqrt{\pi}} \frac{f^2}{f_p^3} e^{-(\frac{f}{f_p})^2} \cdot 2r\left|\sin(\pi f\Delta t)\right| df} \quad . \tag{4-5}$$

As Δt approach zero, $\left|\sin(\pi f\Delta t)\right|$ approaches $\pi f\Delta t$.

Following Cohen (1995) and Barnes (1993) the peak instantaneous frequency of a Ricker wavelet convolved with a wedge is

$$\bar{f}_i \approx \frac{\int_0^\infty f \frac{2}{\sqrt{\pi}} \frac{f^2}{f_p^3} e^{-(\frac{f}{f_p})^2} \cdot 2r\pi f\Delta t df}{\int_0^\infty \frac{2}{\sqrt{\pi}} \frac{f^2}{f_p^3} e^{-(\frac{f}{f_p})^2} \cdot 2r\pi f\Delta t df}$$

$$= \frac{\Gamma(\frac{5}{2})}{\Gamma(2)} f_p = \frac{3}{4}\sqrt{\pi} f_p \approx 1.3293 f_p \quad . \tag{4-6}$$

This estimate differs slightly from Robertson and Nogami (1984), who predict the peak instantaneous frequency of single zero-phase Ricker wavelet to be

$$\bar{f}_i \approx 1.1283 f_p \quad . \tag{4-7}$$

Equation 4-6 is valid only when the top and bottom reflection coefficients have equal magnitude and opposite polarity. The other assumption is that Δt is close to zero.

Equations 4-6 and 4-7 tell us that the peak instantaneous frequency of a thin bed seismic response is somewhat higher than Robertson and Nogami's (1984) thick bed seismic response. This phenomenon may be used to find the relationship between peak instantaneous frequency and thickness.

4.3 WEDGE MODEL EXAMPLE

I built two wedge models to test this method. The top and bottom reflection coefficients of the first wedge model have the same magnitude but opposite polarity (-0.01 and +0.01). The second wedge model has different magnitude top and bottom reflection coefficients (-0.01 and +0.009).The input wavelet is a zero-phase Ricker wavelet with peak frequency 35 Hz. Both wedge thicknesses increase from 0.3 m (first trace) to 25 m (last trace). Figure 4.1 shows the synthetic seismic response of the first wedge model. Figure 4.2 represents maximum amplitude and peak instantaneous frequency versus wedge thickness for the two wedge models. I plot the peak frequency against thickness for these two models and note that the peak instantaneous frequency has an inverse relationship with wedge thickness with peak instantaneous frequency decreasing when the wedge thickness increases. For the second model (red dash line) this pattern is repeated except for a change at very small thicknesses (less than one-eighth wavelength).

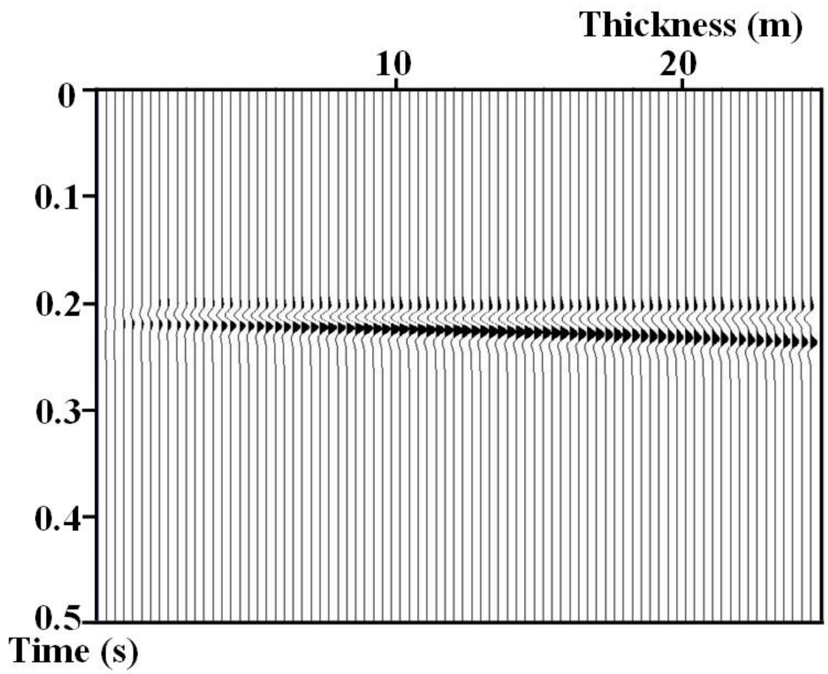

Figure 4.1 Synthetic seismic response of wedge model with top and bottom reflection coefficients -0.01 and 0.01.

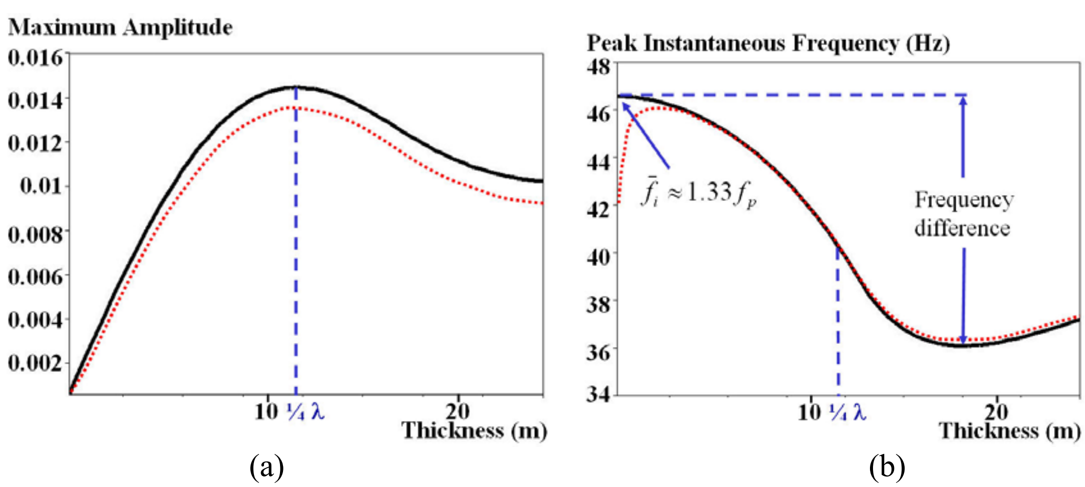

Figure 4.2 (a) Maximum amplitude versus wedge thickness for the two models. (b) Peak instantaneous frequency versus wedge thickness for the two wedge models. (First wedge model with -0.01 and 0.01 is black solid line, second wedge model with -0.01 and 0.009 is red dash line)

4.4 FIELD DATA EXAMPLE

My field data are from the Fort Worth Basin, TX, U.S.A. and consist of a 3-D seismic dataset and 25 wells. The Caddo limestone is present across the entire 3-D survey and is thinner than the dominant wavelength of the seismic data (Figure 4.3). The P-wave velocity of Caddo limestone is around 18000 ft/s (or around 5600 m/s), and the quarter wavelength of Caddo limestone is around 80 ft or a frequency of 56 Hz. Using the Hilbert transform to calculate the complex seismic attributes, I can easily compute the instantaneous frequency of all the traces. In a 9 ms window around the zero-crossing of Caddo limestone event, I extract the peak instantaneous frequency and display it as a map (Figure 4.4). Since the whole survey is composed of three surveys of different data quality, I did not use the two old small seismic surveys which are denoted by the dashed red lines. Only 16 wells of the biggest survey are used for following thickness prediction.

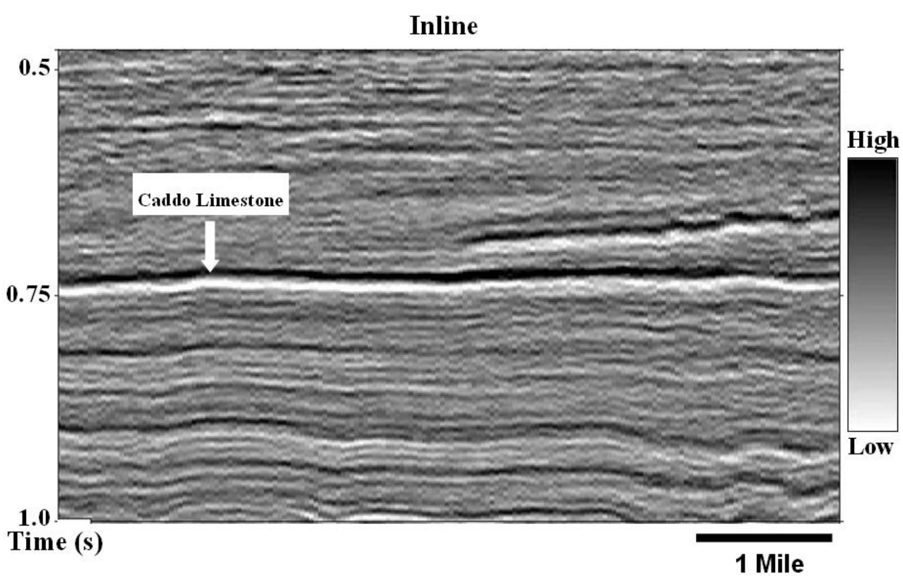

Figure 4.3 Seismic vertical section with Caddo limestone thin bed response just above 0.75 s. (Seismic data courtesy of Devon Energy)

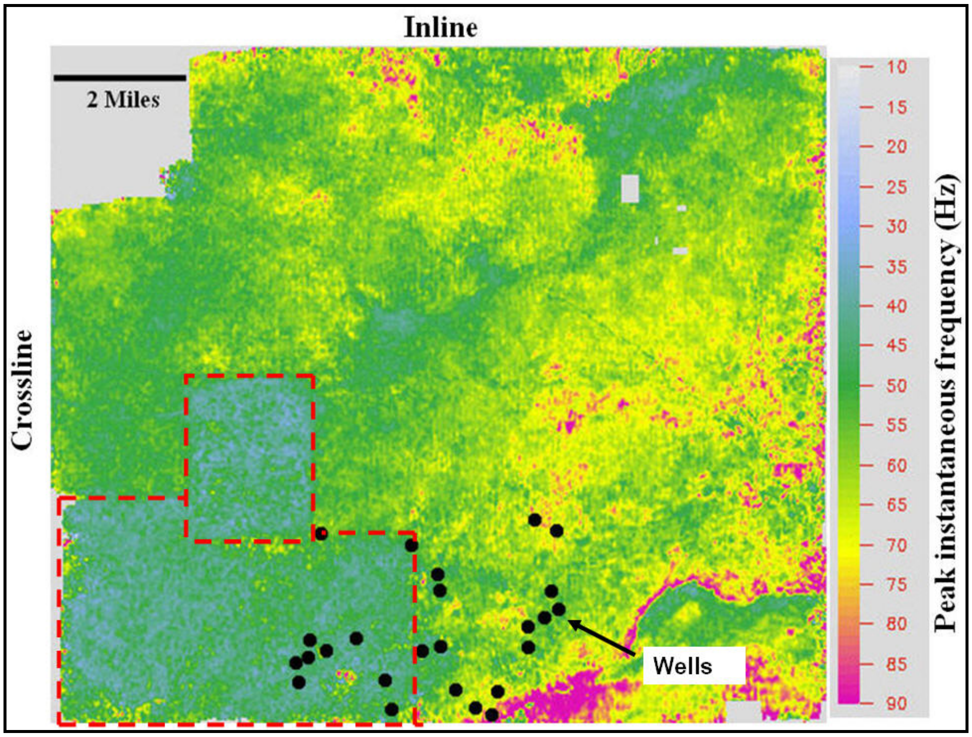

Figure 4.4 Peak Instantaneous frequency map of Caddo limestone (Black dots are well locations; areas inside dashed red lines are two old surveys). (Data courtesy of Devon Energy)

Next I measure the Caddo limestone thickness from logs at each of the 16 wells and cross-plot it against the peak instantaneous frequency (Figure 4.5). To simplify the problem, I use a simple inverse linear trend to define the relation between peak instantaneous frequency and thickness. Based on this inverse linear trend, we can estimate the Caddo limestone thickness throughout the whole survey (Figure 4.6). The cold colors (blue) indicate thinner areas, while the hot colors (red) indicate thicker areas. Figure 4.7 represents the RMS amplitude around the limestone horizon. Comparing Figures 4.6 and 4.7, they have good matches for the thin bed zones and thick zone indicated by black arrows. From amplitude tuning curves, we know that amplitude increases as thickness increases when the thin bed thickness falls below the tuning thickness (quarter wavelength).

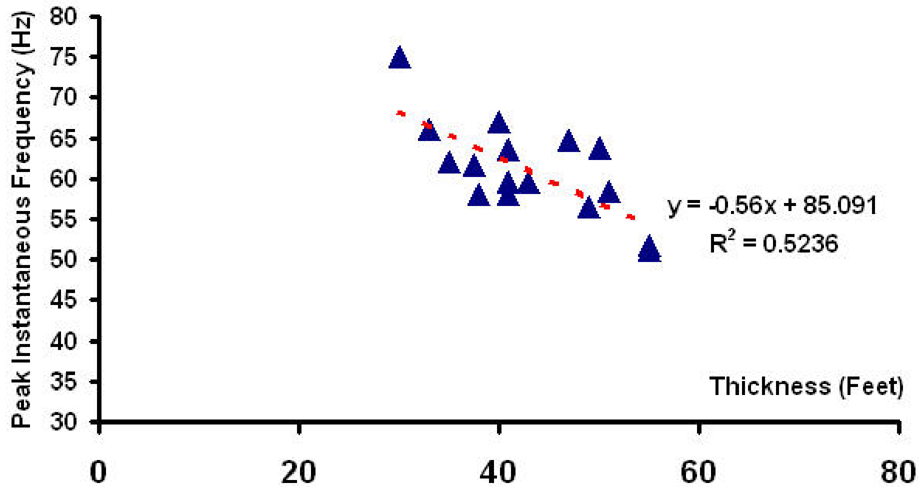

Figure 4.5 Cross-plot of peak instantaneous frequency and Caddo limestone thickness.

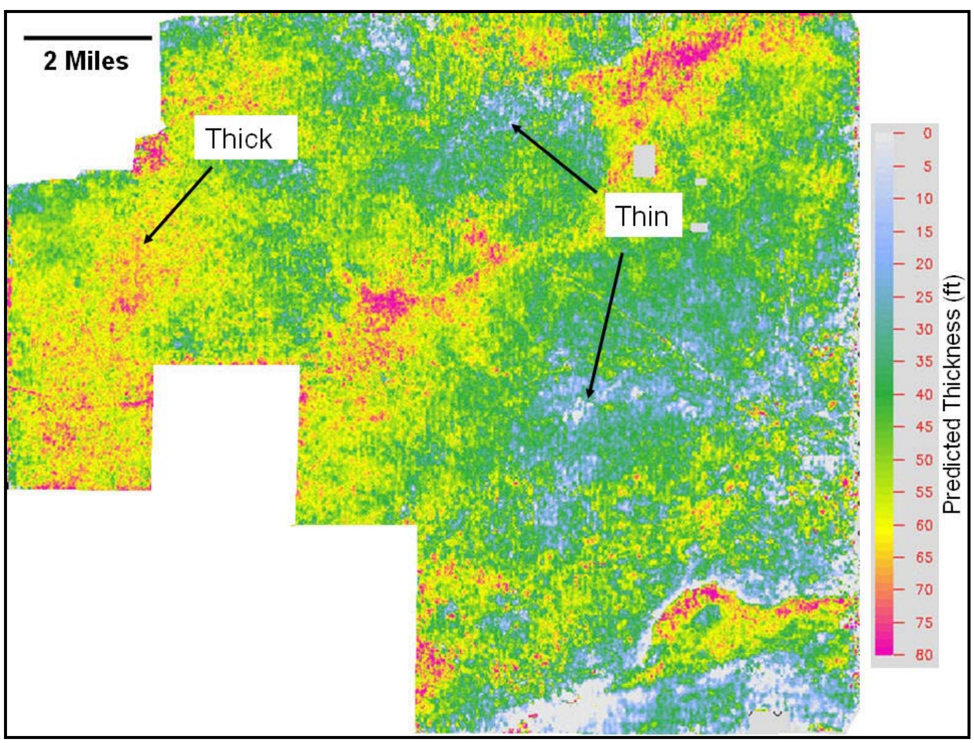

Figure 4.6 Predicted Caddo limestone thickness through simple inverse linear trend of Figure 4.5.

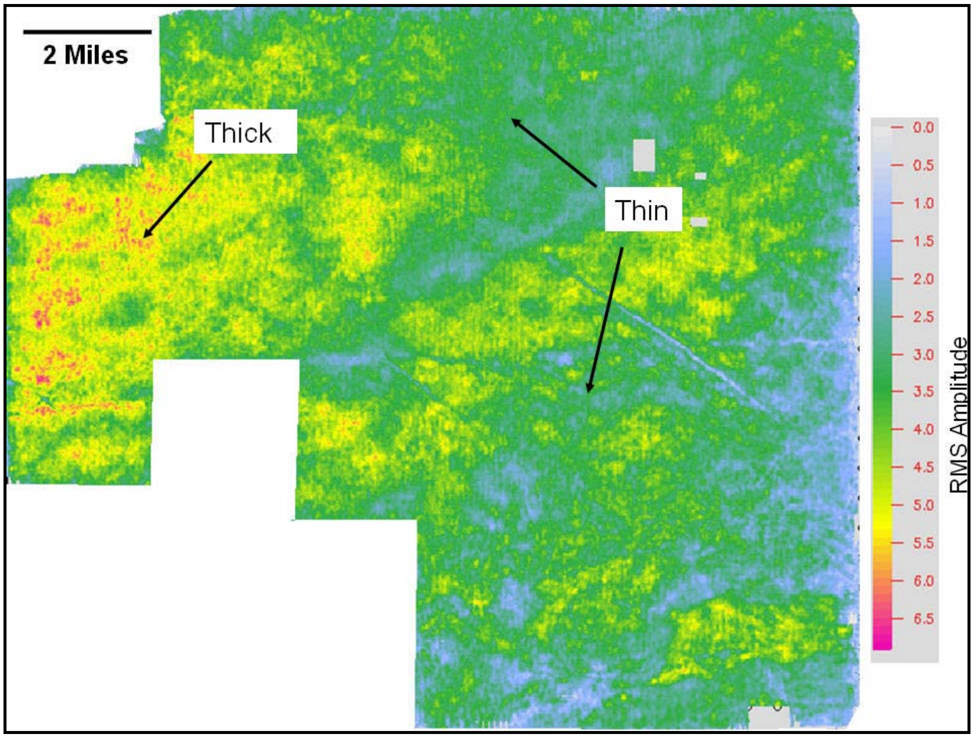

Figure 4.7 RMS amplitude around Caddo limestone horizon.

To better understand the processes that gave rise to these variations in thickness, I examine a horizon slice along the Caddo horizon through the most negative curvature volume (Figure 4.8). The collapse features and structural control through basement faulting is discussed by Sullivan *et al.* (2006). Although these processes began as early as the Ordovician, the Caddo was assumed to be deposited as a thin, flat layer, the curvature that we see in Figure 4.8 was induced after Caddo deposition (or during or after Pennsylvanian). Hardage *et al.* (1996) document how these collapse features provide increased accommodation space for the Atoka sands that lie just below the Caddo limestone. Therefore, I interpret the thicker areas of Caddo accumulation to correspond to increased accommodation space through a combination of tectonics and deeper diagenesis during Pennsylvanian time. Given the thickness of the Caddo, it should not be surprising that only some of these potential depocenters were active.

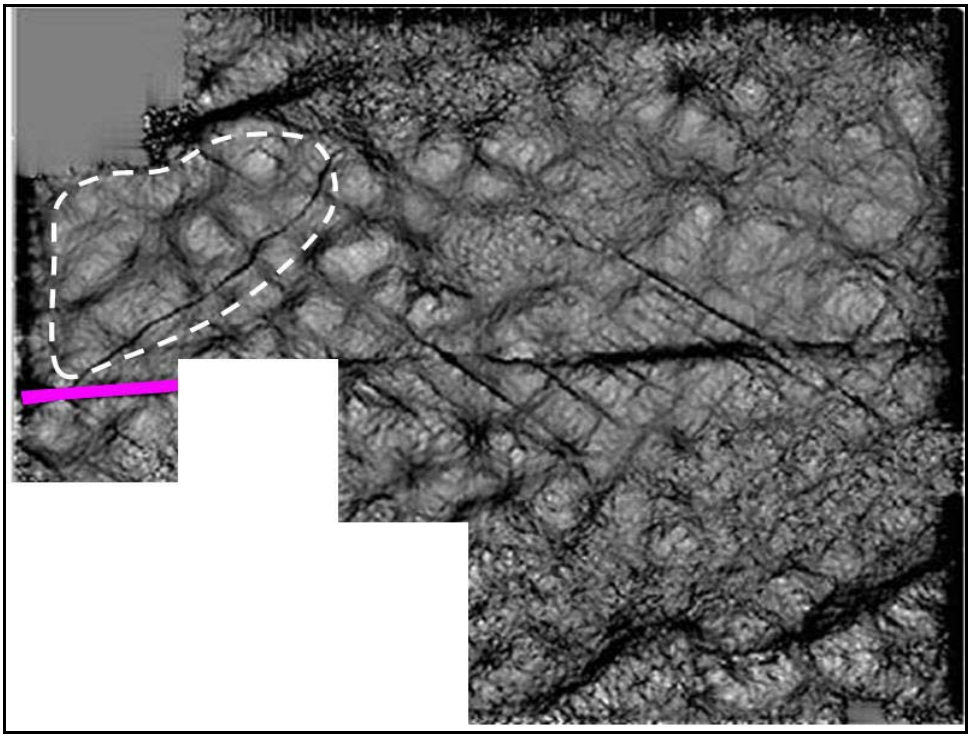

Figure 4.8 Horizon slice along the Caddo through the most negative curvature volume. Thick zone denoted by magenta is controlled by a strike slip fault and Riedel shear seen in curvature. Thicker areas (in Figure 4.7) denoted by white lines correspond to collapse features seen in curvature.

4.5 SUMMARY

Thin bed thickness can be predicted by peak instantaneous frequency when the thin bed response has small interference effects from other layers. Based on a simple wedge model, the peak instantaneous frequency is inversely proportional to the layer thickness such that thinner layers exhibit a higher peak instantaneous frequency. However, when the top and bottom reflection coefficients are different, this inverse trend becomes more complicated for layers less than one eighth wavelength thick. I have shown that given adequate well control that the peak instantaneous frequency can provide a good estimate of reservoir thickness of layers below thin bed tuning such as the Caddo limestone in the Fort Worth Basin. This prediction method can be considered an alternative thickness prediction technique to calibrate the thickness predicted by the popular amplitude technique presented by Widess (1973).

CHAPTER 5

INSTANTANEOUS SPECTRAL ATTRIBUTES TO DETECT CHANNELS*

5.1 INTRODUCTION

Channels filled with porous rock and encased in a nonporous matrix comprise one of the more important stratigraphic exploration plays. However, detailed mapping of channels has a much broader impact. By using modern and paleo analogs, mapping channels helps map the paleo depositional environment, and helps interpret less obvious prospective areas such as fans and levees. By mapping the width, tortuousity, and spatial relation of meandering channels, avulsions, braided streams, among others, geomorphologists are able to infer channel depth and fluid velocity during the time of formation, and thus better risk whether the fill is sand or shale prone.

Seismic coherence and other edge-sensitive attributes (Bahorich and Farmer, 1995, Luo *et al.*, 2003) are among the most popular means of mapping channel boundaries. Although these attributes can easily detect channel edges, they cannot indicate the channel's thickness. As channels become very thin (well below ¼ wavelength) their waveform becomes constant, such that coherence measures based on waveform shape cannot see the channel at all (Chopra and Marfurt, 2006).

---

* Jianlei Liu and Kurt Marfurt, to appear in Geophysics

Spectral decomposition has been used to highlight channels (Partyka *et al.*, 1999; Peyton *et al.*, 1999). The spectral decomposition images are complementary to coherence and edge-detection attribute images in that they are sensitive to channel thickness rather than to lateral changes in seismic waveform or amplitude. Spectral decomposition analysis can be done within a fixed sized analysis window (using a short-window discrete Fourier transform, or SWDFT) following a picked stratigraphic horizon, thereby generating a suite of constant frequency spectral amplitude maps. Most commonly, the interpreter animates through these maps and chooses those maps with spatial patterns corresponding to reasonable geological models. There is a strong correlation between channel thickness and spectral amplitude (Laughlin *et al.*, 2002).

Widess (1973) showed that for thin beds below the tuning frequency, the composite seismic amplitude decreases linearly with thickness. Chuang and Lawton (1995) generalized this work using a frequency spectrum and observed that the peak frequency slightly increases as the layer thickness decreases. Marfurt and Kirlin (2001) exploited this observation and applied it to a SWDFT of a data set for the Plio-Pleistocene Mississippi River in the Gulf of Mexico. They found that the frequency corresponding to the peak spectral amplitude is an excellent means of summarizing the information content of the full spectrum, with a low peak frequency corresponding to thick channels, and a high peak frequency corresponding to thin channels.

Even with careful tapering, spectral decomposition using the SWDFT has window effects (Cohen, 1995). For this reason, Castagna *et al.* (2003) looked at alternative time-frequency decomposition methods based on wavelet transforms to compute what is commonly called instantaneous spectral attributes (ISA). Much of their work has been used to identify channels (e.g. Sinha *et al.*, 2005; Matos *et al.*, 2005), but to my knowledge, little has been published on the use of peak-frequency volumes based on these techniques, although Liu *et al.* (2004) showed how the ISA peak frequency significantly increases with decreasing layer thickness.

In this chapter, I will show how instantaneous spectral attributes can be used to generate composite volumes of both peak spectral frequency and the amplitude at that peak spectral frequency. I show how these algorithms behave on simple synthetics. I then show how the peak frequency and the amplitude of the peak frequency can be effectively co-rendered using a 2D color map (or palette). By generating a composite of this 2D color map with a gray scale we can also co-render coherence. Finally, I apply this workflow to two channels systems – one seen in a marine survey acquired over Tertiary channels acquired in Gulf of Mexico, and the other seen in a land survey acquired over Paleozoic channels in Central Basin Platform, West Texas, U.S.A.

5.2 SYNTHETIC MODEL

In Figure 5.1a, I built a simple wedge model to test the relation between thickness and instantaneous spectral attributes. Figures 5.1b-d represent the instantaneous spectral component at 20 Hz, 30 Hz and 40 Hz, respectively. The source wavelet is a zero-phase Ricker wavelet with a peak frequency at 30 Hz. The P-wave velocity of the wedge is

(2200 m/s) and the thickness linearly increases from 0 m to 30 m. Comparing Figures 5.1b-d, we note that the maximum amplitude of single frequency component section moves to the left or narrower side of the wedge, indicated by red arrows. This movement shows how ISA components respond to the thin bed tuning effect reported by Widess (1973), who noted that the peak amplitude response will occur at 1/4 wavelength of dominant period.

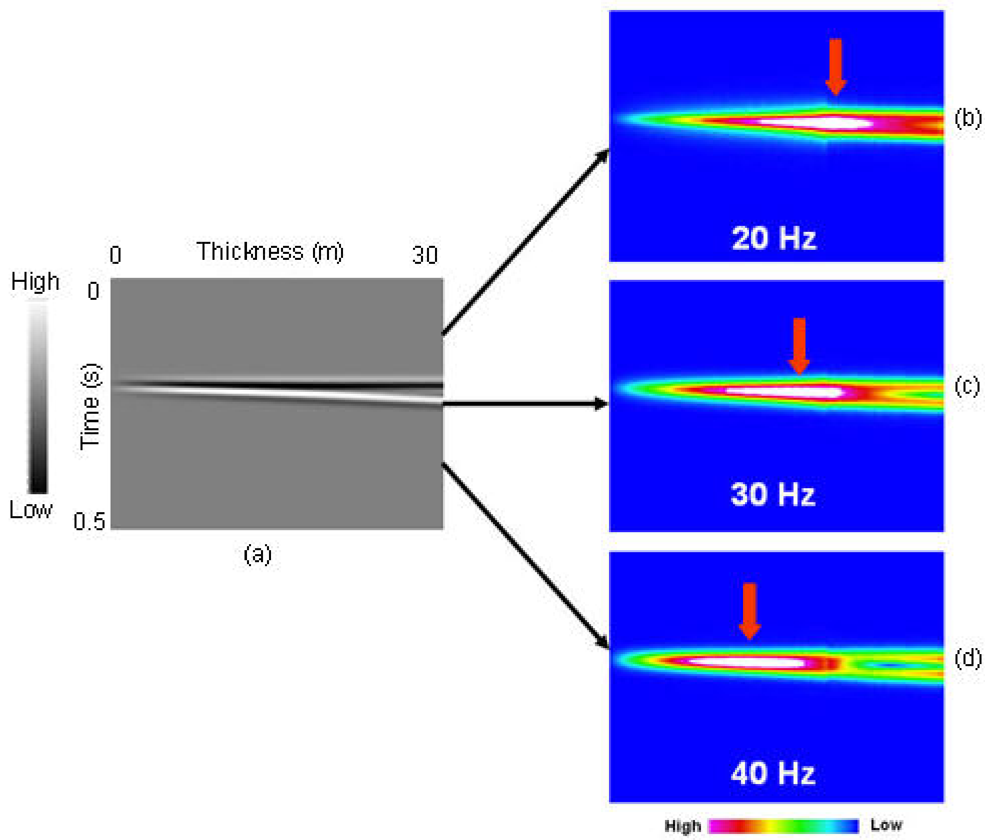

Figure 5.1 (a) Synthetic seismic response of wedge model; (b) spectral component 20 Hz; (c) spectral component 30 Hz; (d) spectral component 40 Hz.

5.3 2D COLOR MAPS

Many seismic attributes are only meaningful when put in the context of a second, independent, attribute. For example, a measurement of reflector azimuth is meaningless if the dip magnitude of the reflector is flat. Similarly, a measure of wavelet phase is meaningless if its amplitude falls below the signal-to-noise level. In this chapter, the value of the peak spectral frequency has meaning only if that peak lies significantly above the average amplitude spectrum. I choose a 2D color map which combines hue and lightness that will be used to represent peak frequency and peak amplitude above average, respectively (Figure 5.2a). Figures 5.2b and 5.2c depict two idealized spectra, one that is high amplitude, highly peaked at a high frequency, and one that is lower amplitude, flatter and peaked at a lower frequency. Since the spectrum shown in Figure 5.2b has a relative higher peak frequency and peak amplitude above average, it will be represented by the bright red color shown in Figure 5.2a. In contrast, the spectrum shown in Figure 5.2c has a lower peak frequency and peak amplitude above average and will represented by the dark green color shown in Figure 5.2a.

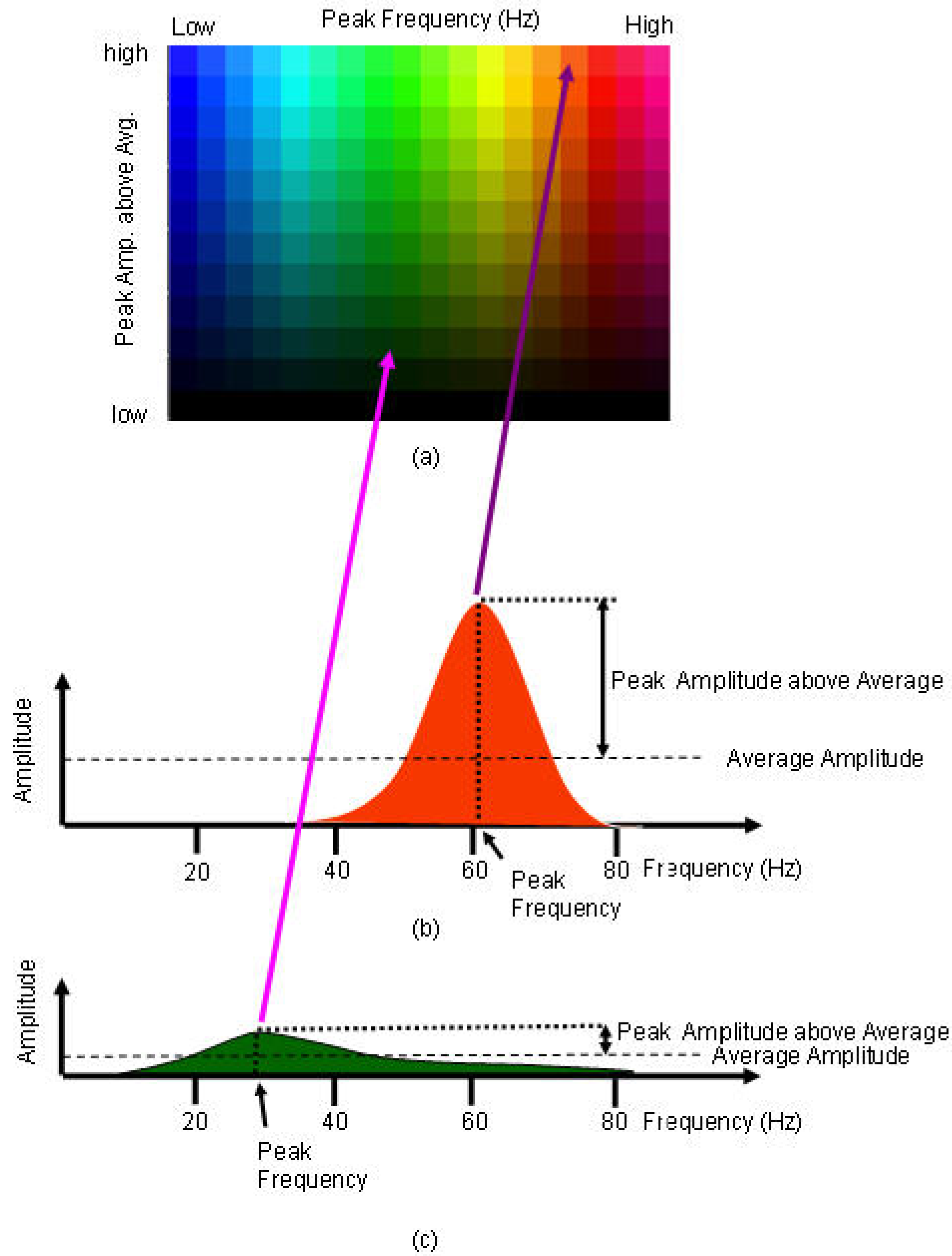

Figure 5.2 (a) 2D color map of peak frequency mapped against hue and peak amplitude above background mapped against lightness (After Lin *et al.*, 2003). Two idealized spectra include (b) a spectrum with a high peak frequency and high amplitude above average maps to a bright orange color, and (c) a spectrum with a low peak frequency and low amplitude above average maps to a dark green color.

To display coherence, I turn to the concept of composite displays discussed by Chopra (2001) and Lin *et al.* (2003) (Figure 5.3). If the coherence is above a threshold, I will display the peak frequency and amplitude using the 2D color table displayed in Figure 5.2a. If the coherence falls below a threshold, I will display the coherence against a 1D gray scale. In this manner, coherence defines the edges (and thus width) of the channels, while the peak frequency defines the relative thickness.

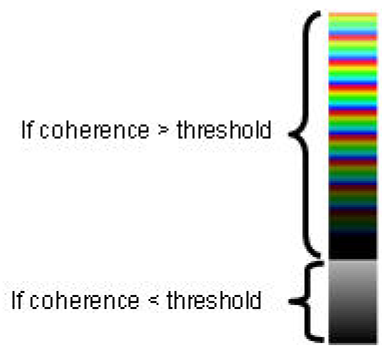

Figure 5.3 Color map showing compositing of coherence and spectral component volumes. For high values of coherence (indicating good reflectors) I plot peak frequency and peak amplitude above average using the 2D color table shown in Figure 5.2a. For low values of coherence I plot coherence against a simple gray scale. For use with conventional color display tools, the color bar needs to be mapped to the traditional 1D color bar indicated in this figure. The composite image is generated by first creating an output attribute volume with values ranging between 0 and 255. Each of these values map to a corresponding RGB triplet shown in this Figure.

Figure 5.4 shows a map view and a cross section of an idealized channel system. From this image, the thick main channel is statistically wider and indicates a low peak frequency response. The narrower channel is statistically thinner, and therefore tunes at a higher peak frequency.

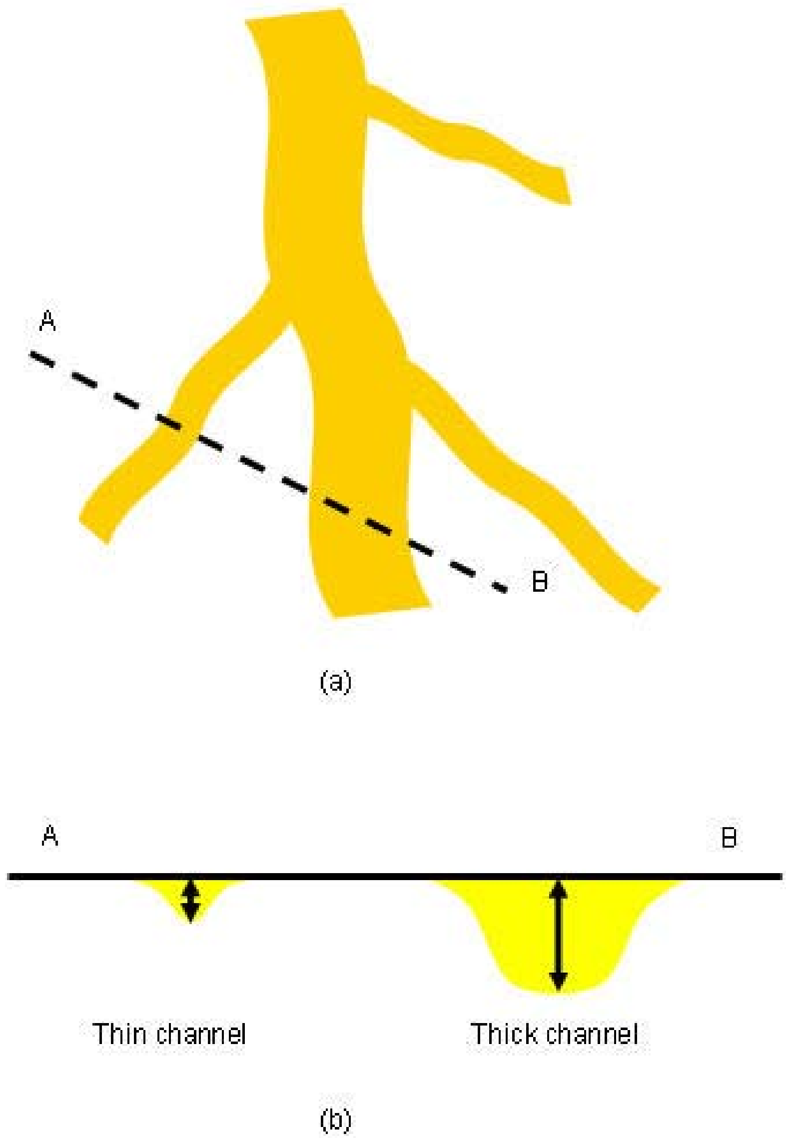

Figure 5.4 (a) Map view and (b) cross section view of idealized channels.

5.4 FIELD DATA EXAMPLES

5.4.1 *A Marine Survey over Tertiary Channels: South Marsh Island, Gulf of Mexico*

Conventional analysis through animation of spectral components as described by Partyka *et al.* (1999) works very well when applied to a horizon. This methodology breaks down, however, when analyzing volumes of seismic data, such as the one shown in Figure 5.5 for a South Marsh Island survey. Generation of eighty output volumes at 1 Hz increments between 10 and 90 Hz quickly fills the available disk space. The computational effort of spectral decomposition is greatly outweighed by shear amount of output data. Even though we can reduce the output volumes by sampling every 10 Hz, it is still awkward to simultaneously deal with 9 common frequency volumes. For this reason, I propose generating only the peak frequency and peak amplitude volumes by time-frequency decomposition, and combining them with coherence, thereby providing an image that can be used to rapidly identify features of stratigraphic interest. If appropriate, the individual spectral components can be regenerated and examined either along constrained zones of interest, or for a constrained range of frequencies (such as done for reservoir illumination by Fahmy *et al.*, 2005).

Figure 5.6a shows the time slice of coherence volume at t = 1.416 s. White arrows indicate a wide main channel and yellow arrows indicate a narrow branch channel. In the time slice through the 20 Hz spectral component, Figure 5.6b, only the main channel shows up. In contrast, in the time slice through the 60 Hz spectral component, Figure 5.6c, only the branch channel shows up. This phenomenon implies that the main channel is thicker than its branch.

The following examples will be applied to a composite volume of peak frequency, peak amplitude and coherence, for the same data set of Louisiana shelf, Gulf of Mexico. The plot uses a composite color map of hue-lightness-gray.

Figure 5.7a shows a time slice of coherence volume at t = 1.230 s. The meandering channels are easily interpreted in the coherence time slice (white arrows). Figure 5.7b demonstrates the time slice of composite volume of peak frequency, peak amplitude and coherence of the same slice time. In Figure 5.7b, white arrows point to the meandering channels. Comparing Figures 5.7a and 5.7b, we see that the composite plot can highlight channels from background color. For instance, most of the channels are plotted by green color. The coherence can detect the discontinuity of seismic events corresponding to the edge of the channel, while the peak frequency and peak amplitude can highlight channel in different color. Figures 5.8a and 5.8b show another time slice of coherence and composite volume at 1.482 second. The meandering channel is apparently shown in both time slices (white arrows). The advantage of the composite plot is that peak frequency and peak amplitude can add additional information to predict variation of thickness. For instance, in upper section (triangular section) of Figure 5.8b, the color of peak frequency changes from blue to green and red which may indicate the thickness changes from thick to thin. Higher peak frequency tuning indicates thinner thickness.

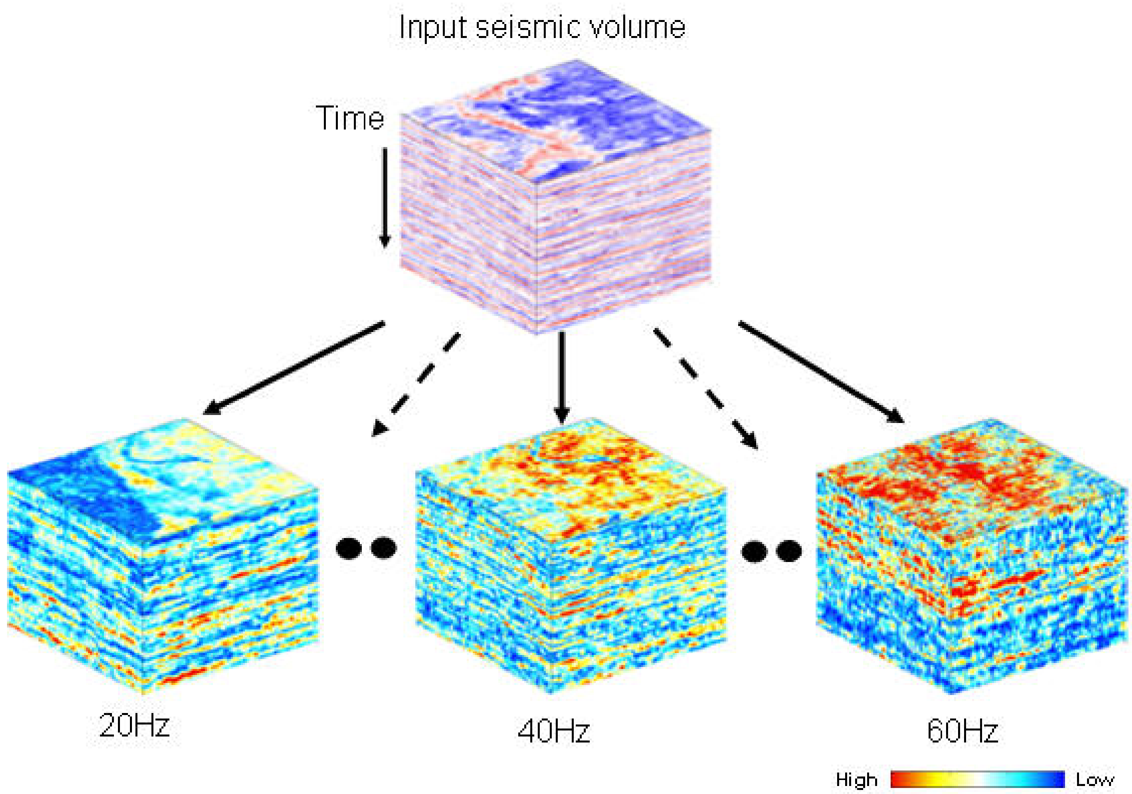

Figure 5.5 An example of 3D time-frequency decomposition showing one input seismic volume and multiple decomposed single frequency volumes of 20 Hz, 40 Hz and 60 Hz for an OBC data volume acquired over South Marsh Island, Gulf of Mexico. (Data courtesy of Fairfield Industries)

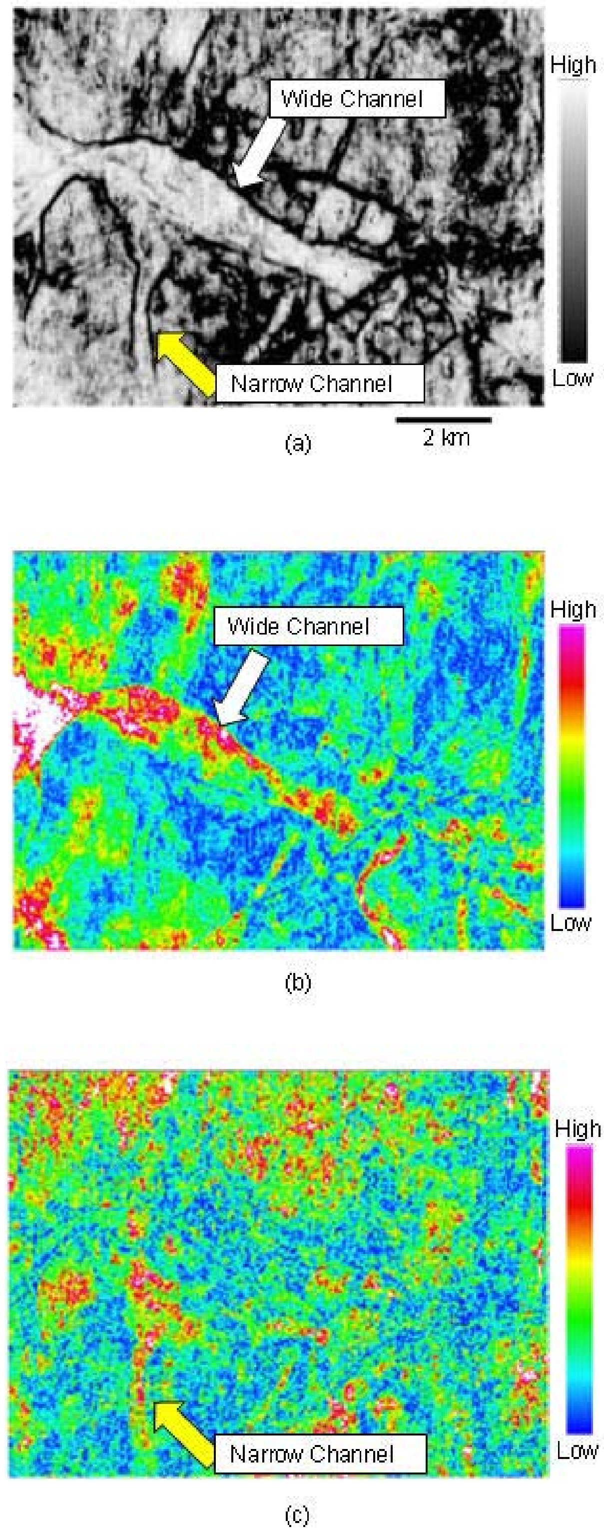

Figure 5.6 Time slices at t = 1.416 s through (a) coherence, (b) the 20 Hz spectral component, and (c) the 60 Hz spectral component for the same input volume shown at the top of Figure 5.5.

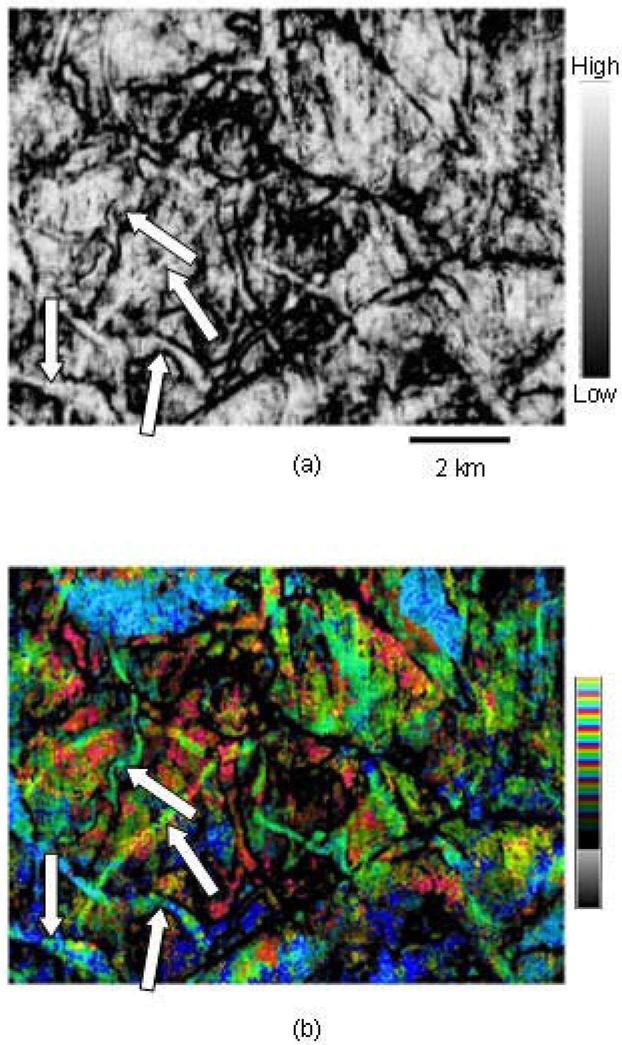

Figure 5.7 (a) Time slice of coherence volume at t = 1.230 s; (b) time slice of composite volume of peak frequency, peak amplitude and coherence at t = 1.230 s.

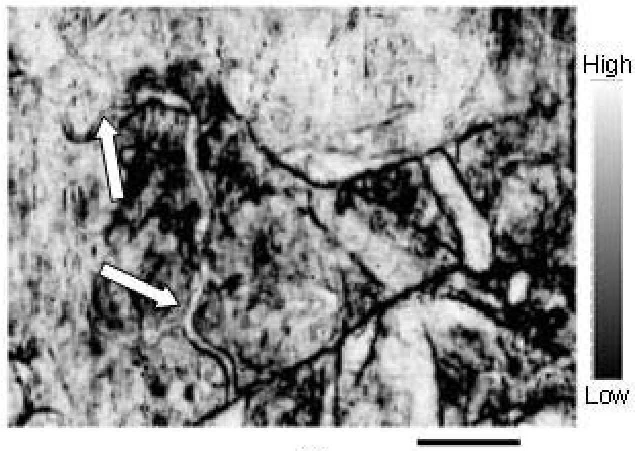

(a)

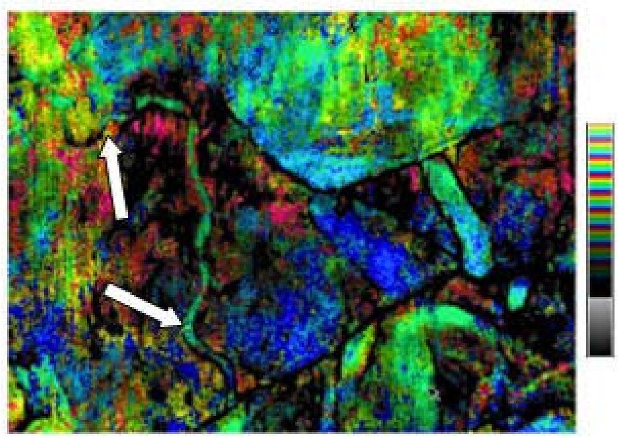

(b)

Figure 5.8 (a) Time slice of coherence volume at t = 1.482 s; (b) time slice of composite volume of peak frequency, peak amplitude and coherence at t = 1.482 s.

5.4.2 *A Land Survey over Paleozoic Channels: Central Basin Platform, West Texas, U.S.A.*

I now apply this same technique, to older, indurated rocks imaged in the second field data example from West Texas, USA. Figure 5.9 shows the time slice of seismic volume at t = 1.060 s. The arrows point to Pennsylvanian age channels. Figures 5.10 and 5.11 show two time slices at t = 1.060 and 1.096 s of peak frequency and peak amplitude above average (peak amplitude subtract average amplitude value) using the color bar described in Figure 5.2a. The channels are clearly shown up in these two time slices. We note that the channel has a green color while background has blue color, implying that the channel has a higher peak frequency than the background response. In this image I did not use coherence to identify the edges of the channel, so the color itself highlights the channels. In order to view all the channels in one slice, I flatten the horizon along the Atoka unconformity (the blue pick shown in Figure 5.13a). Figure 5.12a shows the phantom horizon slice 44 ms above the Atoka unconformity. Figures 5.12b-d are amplitude spectra corresponding to the points indicated by the magenta arrows. Figure 5.12b shows a high amplitude peak frequency at about 55 Hz and is thus mapped as bright yellow. Figure 5.12c shows a high amplitude peak frequency at about 43 Hz pointing to the channel mapped as bright green. Figure 5.12d shows a low amplitude peak frequency at about 28 Hz pointing to the background response mapped as a dark blue. Figure 5.13a shows the seismic section of line AB from Figure 5.12a. Figures 5.13b-d show the same amplitude spectrums as Figure 5.12. In the seismic section, the notches in Figure 5.13b are due to bed interferences. Figure 5.13c corresponds to the amplitude spectrum of the channel's response with relatively higher peak frequency compared to the background response plotted in Figure 5.13d. These three graphs show that bed interferences may cause frequency notches (which depend on the bed thickness and geometry), some of which can be individually resolved (as in Figure 5.13b) and others can not (Figure 5.13c).

At present, I interpret these images in three steps. First I use principles of geomorphology together with modern and paleo analogues to identify stratigraphic features of interest. Second, I calibrate these patterns through conventional interpretation of the vertical seismic section, coupled with our understanding of the physics of thin bed interference phenomena. Finally, I use colors to provide a quantitative estimate of relative channel thickness, and coherence to provide a similar quantitative estimate of channel width. These tools can unravel stratigraphic features of interest preserved in the geologic record.

Fortran90 program *flatten,* flattens the horizon slice along the picked horizon time. I provide the UNIX 'man page' of this algorithm as Appendix D.

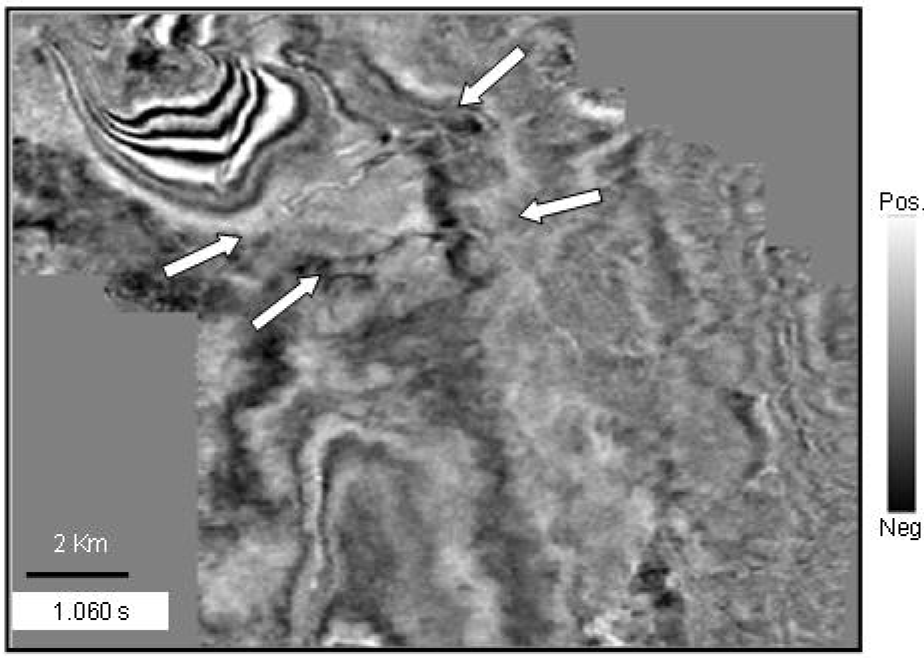

Figure 5.9 Time slice of seismic volume at t = 1.060 s through a survey acquired over the Central Basin Platform, west Texas, U.S.A. White arrows point to two different channel branches. (Seismic data courtesy of Burlington Resources)

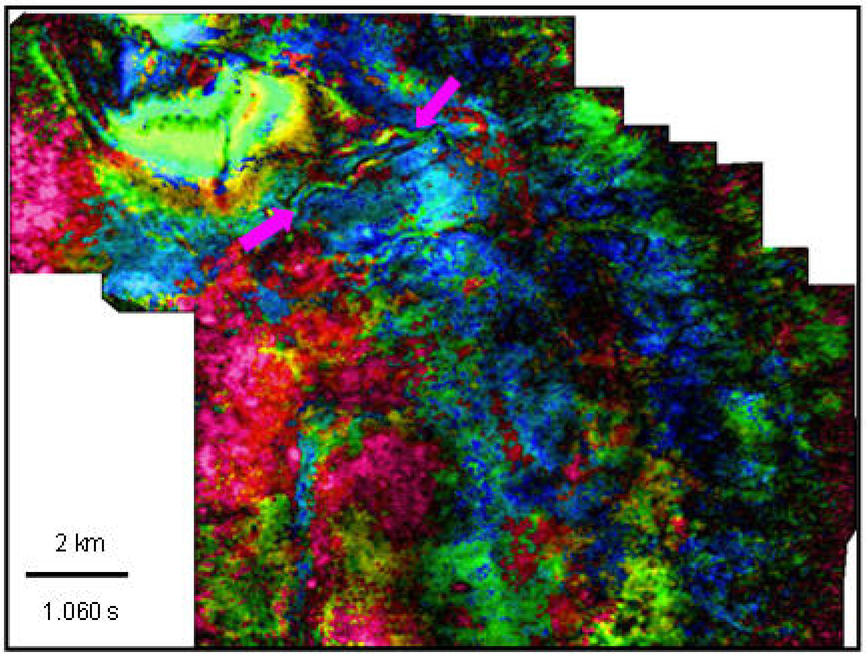

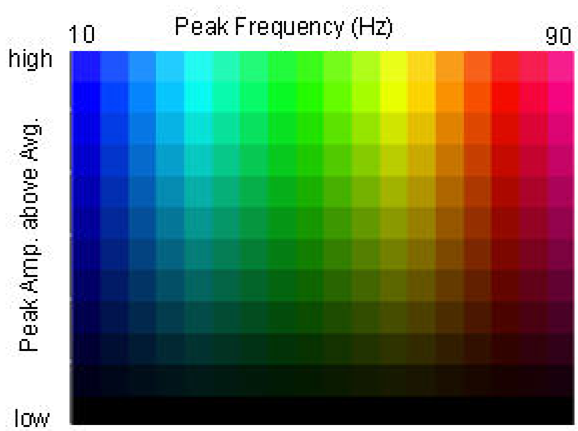

Figure 5.10 Time slice of composite volume of peak frequency and peak amplitude above average with 2D color map at t = 1.060 s. (Magenta arrows point to channel)

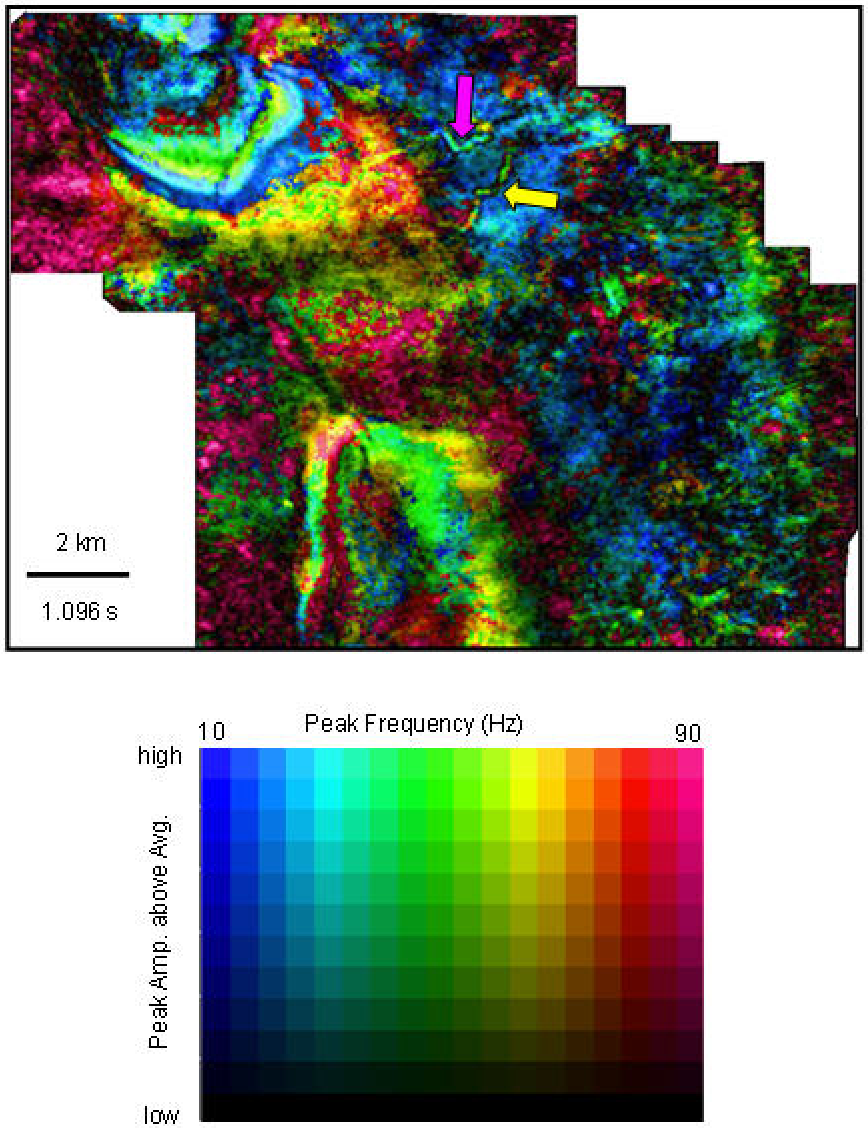

Figure 5.11 Time slice of composite volume of peak frequency and peak amplitude above average with 2D color map at t = 1.096 s. (Magenta and yellow arrows point to channels)

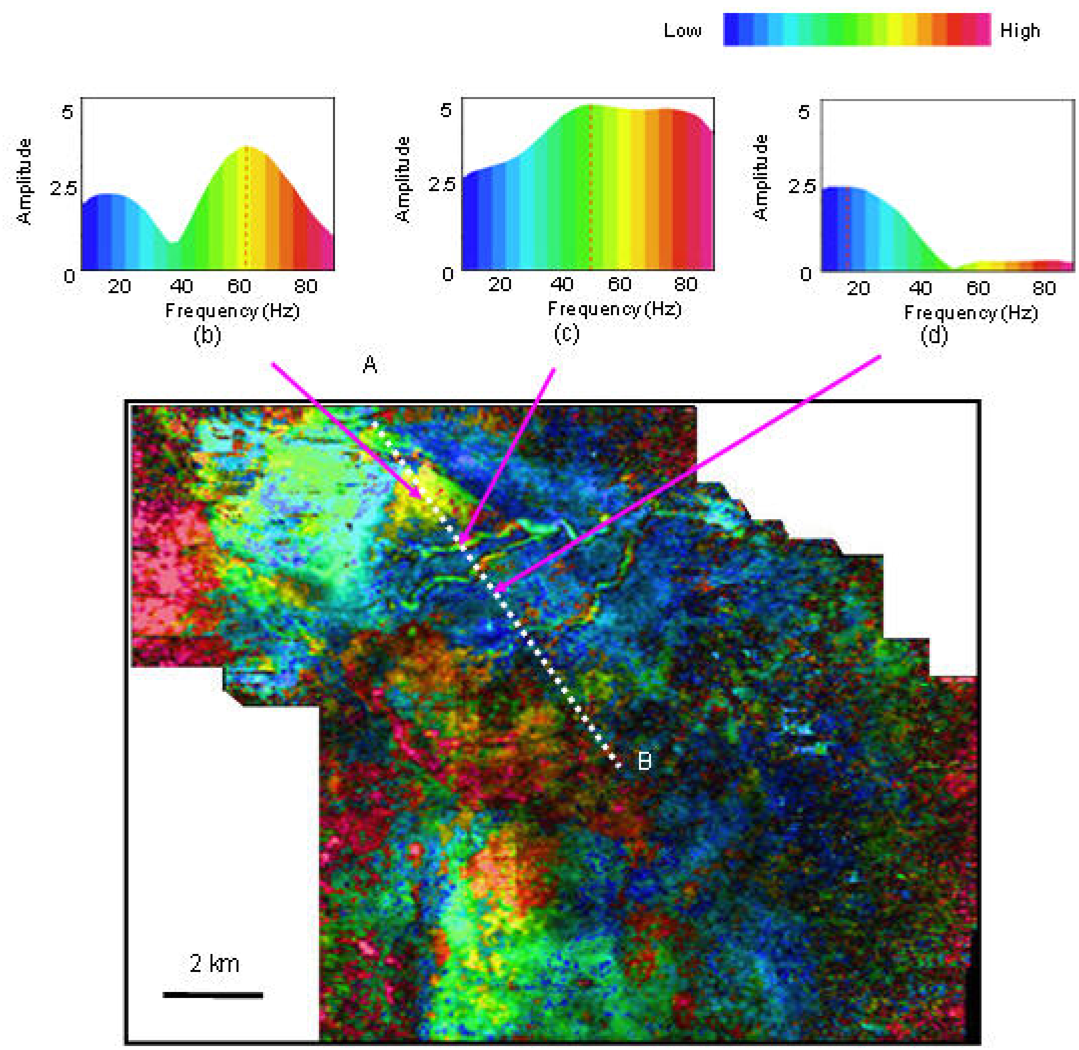

(a)

Figure 5.12 (a) Phantom horizon slice 44 ms above the Atoka unconformity through a composite volume of peak frequency and peak amplitude above average and coherence; (b) amplitude spectrum of the erosional unconformity which appears as bright yellow; (c) amplitude spectrum of the Pennsylvanian age channels draining the erosional unconformity which appear as bright; (d) amplitude spectrum of channel matrix which appears as a lower amplitude spectrum and appears as dark blue.

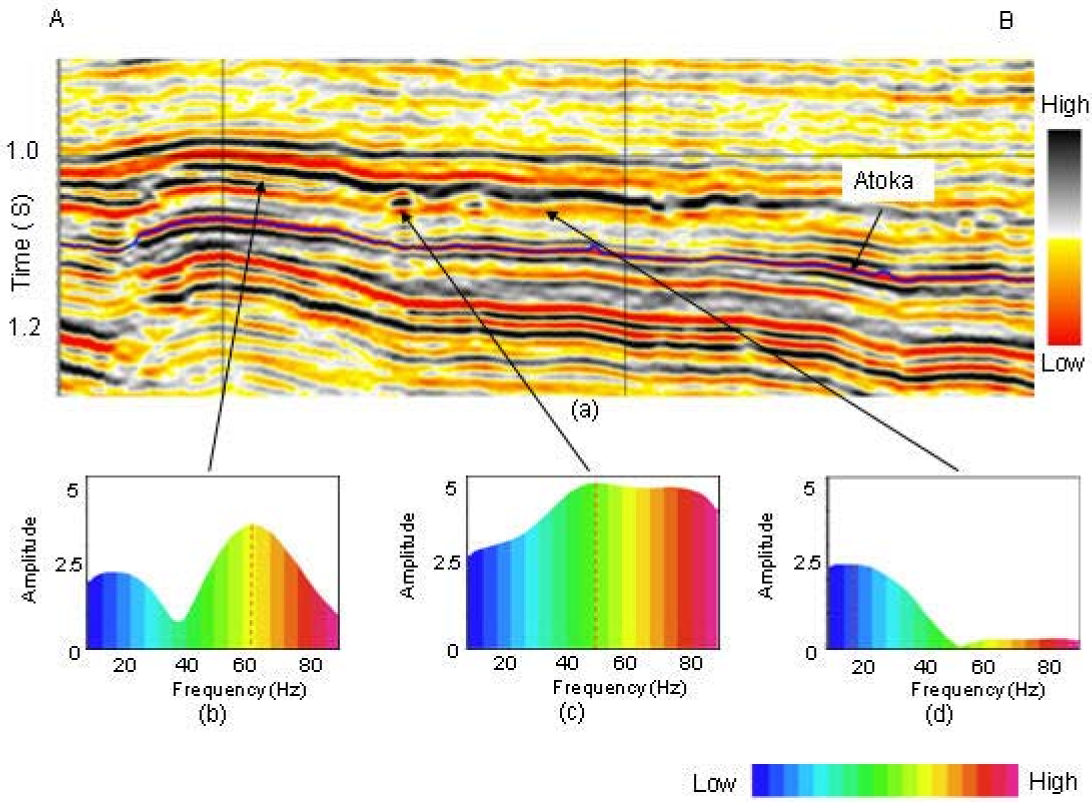

Figure 5.13 (a) Seismic section of line AB from Figure 5.12; (b), (c) and (d) the same amplitude spectrum as Figure 5.12.

5.5 SUMMARY

Through the use of instantaneous spectral analysis based on wavelet-based spectral decomposition, I have extended the concept of using peak spectral frequency of mapped horizons to full 3D volumes. I find that these peak spectral frequencies are most useful if modulated by some measure of the corresponding spectral amplitude. For channels where I expect lateral changes in thin-bed tuning, I find that the peak spectral amplitude above the average spectral amplitude is particularly useful by deemphasizing the appearance of strong-amplitude flat spectral responses.

While spectral decomposition is a good indicator of channel thickness, coherence and other edge detectors are good indicators of channel width. For this reason, I advocate displaying the both attributes in a composite image. I have shown the effectiveness of this technique in mapping Tertiary channels in marine survey. I find this technique to be an excellent tool for rapidly mapping channels that may be of importance both for prospect evaluation and for quantifying reservoir heterogeneity. I am encouraged to believe that by using these three measures together that we can develop improved geostatistics and/or neural net work flows that with well control, can help us quantitatively estimate reservoir thickness.

CHAPTER 6

LOW FREQUENCY HYDROCARBON INDICATORS

6.1 INTRODUCTION

In Chapter 3, I introduced three different spectral attributes display techniques. In Chapters 4 and 5, I applied the spectral attributes to predict thin bed thickness and to detect channels. In this chapter, I will investigate the use of spectral attributes as a hydrocarbon indicator.

After introducing instantaneous frequency, Taner *et al.* (1979) noted that low frequency shadow zones are often associated with gas reservoirs and hypothesized that it could be caused by anomalous attenuation. Barnes (1993) recommended using the average frequency rather than instantaneous frequency, since instantaneous frequency often provides inaccurate spikes where waveforms interfere. Dilay and Eastwood (1995) showed the high frequency loss due to high attenuation. Mitchell *et al.* (1997) discussed that identifying low frequency shadows is useful, but unreliable. Castagna *et al.* (2003) improved on this DHI by using instantaneous spectral analysis. Ebrom (2004) listed ten different stack related and non-stack related mechanisms which may cause low frequency shadow zones. Yang (2003) proposed that low frequency AVO can be used to differentiate between packed and blocky sands. Fahmy *et al.* (2005) showed a field example from offshore West Africa with a low frequency oil reservoir around 11 Hz. Goloshubin *et al.* (2006) proposed that there is a low frequency sensitivity to relative fluid mobility based on double porosity model. Odebeatu *et al.* (2006) proposed that low frequency anomalies associated with a gas reservoir could be due to dispersion.

I apply the RGB display technique introduced in Chapter 3 to a seismic survey from the Louisiana Shelf, Gulf of Mexico, over a known oil and gas field.

6.2 LOW FREQUENCY ZONE DETECTION

In Chapter 3, I introduced the Red-Green-Blue display technique using least-squares fitting with three different basis functions. Now we examine the same field example shown in Figure 3.8 from the Louisiana Shelf, Gulf of Mexico. Figure 6.1 shows two seismic vertical sections A-A' and B-B' as well as a time slice at 2.7 s through the 3-D seismic volume. The white arrow on seismic line A-A' shown in Figure 6.2 indicates an oil reservoir with a gas cap. I plot a representative trace through the reservoir in Figure 6.3 along with its corresponding amplitude spectrum decomposed using the S-transform. At t=2.7 s, we can easily see the low frequency response (black arrow) just below the reservoir around t=2.6 s. I display the amplitude spectra at two different time locations in Figure 6.4. Figure 6.4a shows the amplitude spectrum at t=2.61 s, while Figure 6.4b shows the amplitude spectrum at t=2.7 s. Comparing Figures 6.4a and 6.4b, we note that the amplitude spectrum at t=2.7 s has a relatively lower peak frequency.

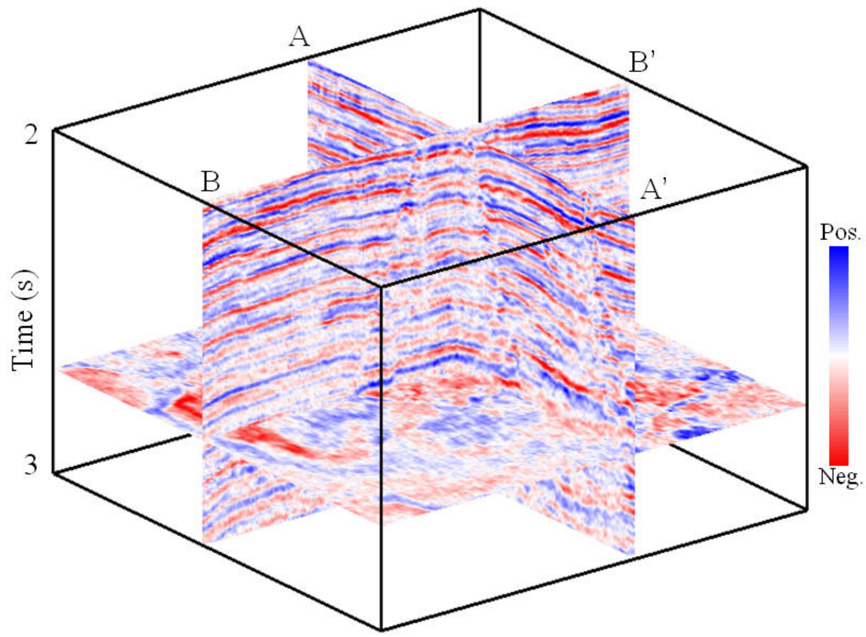

Figure 6.1 Slice view of 3-D seismic volume. (Seismic data courtesy of Fairfield Industries)

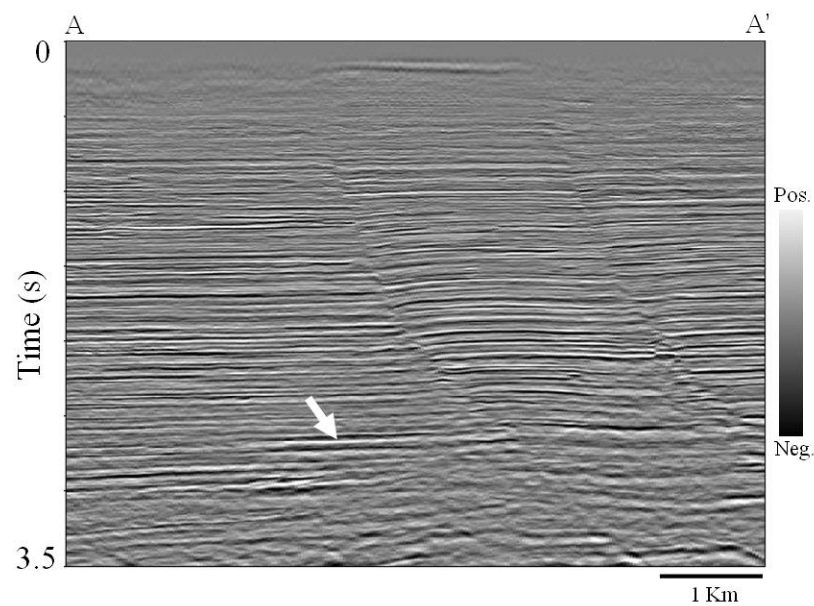

Figure 6.2 Seismic line A-A'. (Seismic data courtesy of Fairfield Industries)

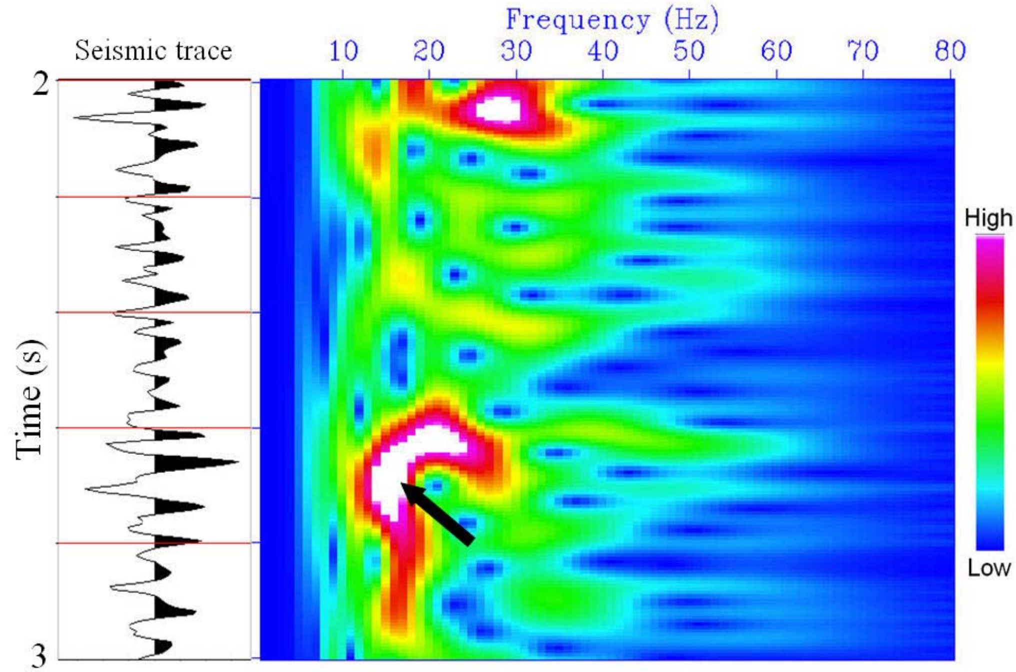

Figure 6.3 One seismic trace and its corresponding amplitude spectrum.

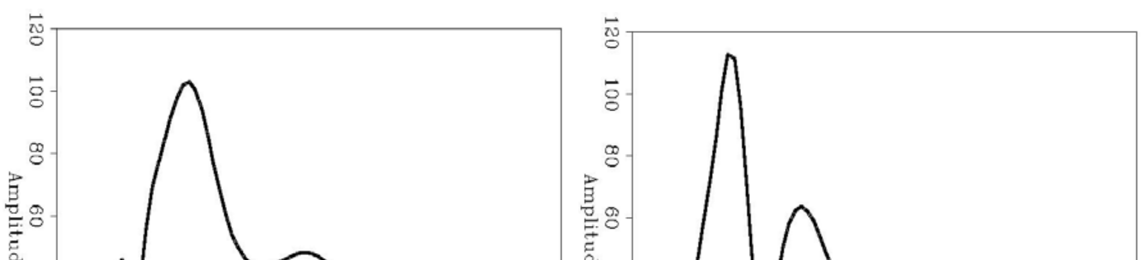

Figure 6.4 Amplitude spectra extracted from Figure 6.3 at (a) t=2.61 s and (b) t=2.7 s. Note the loss of high frequencies below the reservoir level of t=2.61 s.

Figure 6.5 demonstrates the coherence section of seismic line A-A’ (Figure 6.2). From the coherence section, we can easily see two faults. Figures 6.6a and 6.6b show the single frequency sections of 10 Hz and 60 Hz generated by spectral decomposition. The black arrow points to the hydrocarbon reservoir with high amplitude below it (Figure 6.6a). The RGB plot of decomposed spectra is shown in Figure 6.7. The white arrow points to the reservoir level which appears as red, indicating a spectrum richer in lower frequencies.

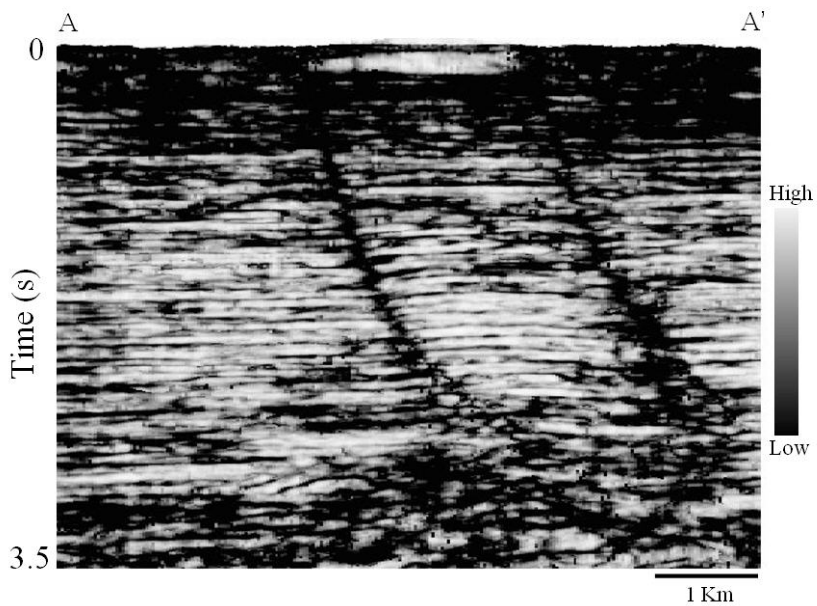

Figure 6.5 The coherence section of seismic line A-A’ shown in Figure 6.2.

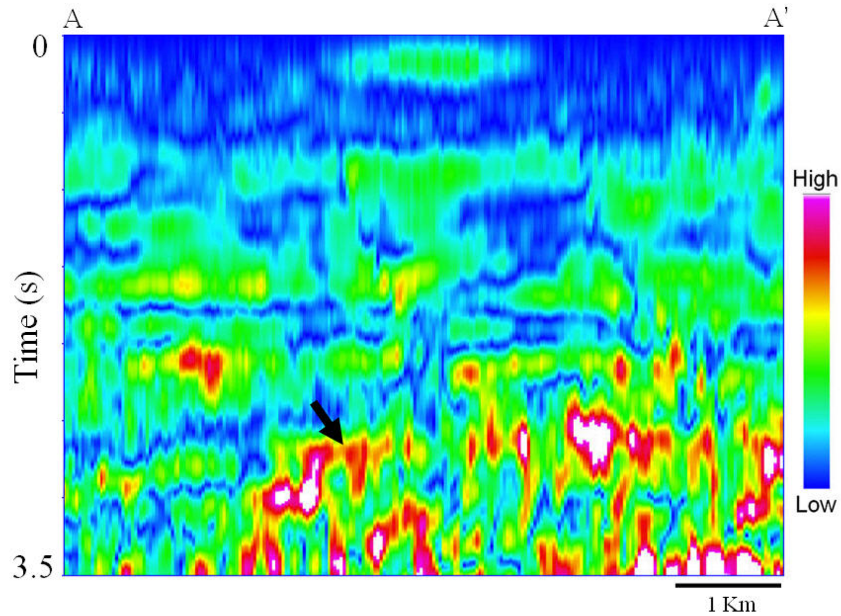

(a)

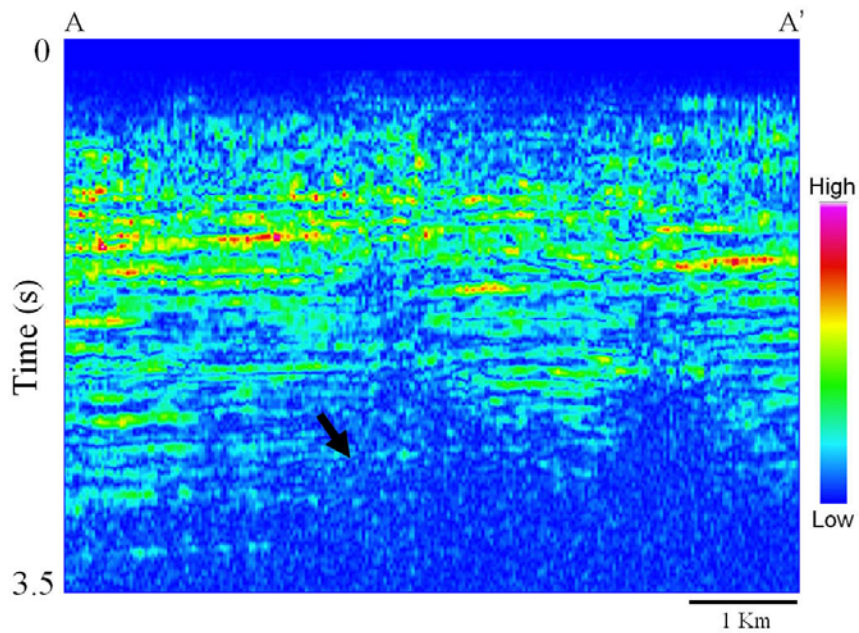

(b)

Figure 6.6 Single frequency sections (a) 10 Hz and (b) 60 Hz of seismic line A-A' (Black arrow point to the hydrocarbon reservoir shown in Figure 6.2).

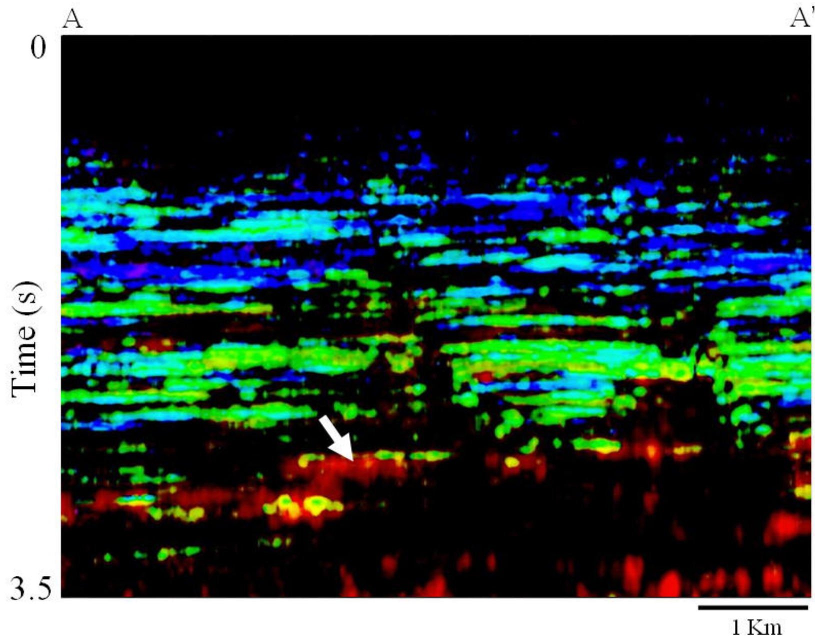

Figure 6.7 RGB plot of decomposed amplitude spectra of seismic line A-A'. (White arrow points to the low frequency zone)

The vertical section of seismic line B-B' is shown in Figure 6.8 where again the white arrow indicates the hydrocarbon reservoir. The corresponding coherence section is shown in Figure 6.9. Figure 6.10 shows the RGB plot of seismic line B-B'. The white arrow in Figure 6.10 indicates the low frequency zone associated with the hydrocarbon reservoir.

A horizon was picked along the peak amplitude of pay reservoir response around 2.6 s. This horizon slice RGB plot of the spectral amplitudes is shown in Figure 6.11. In Figure 6.11, we can easily see the low frequency zones indicated by the white arrow. From the field example, it appears that the RGB display technique is a good tool to detect low frequency zones.

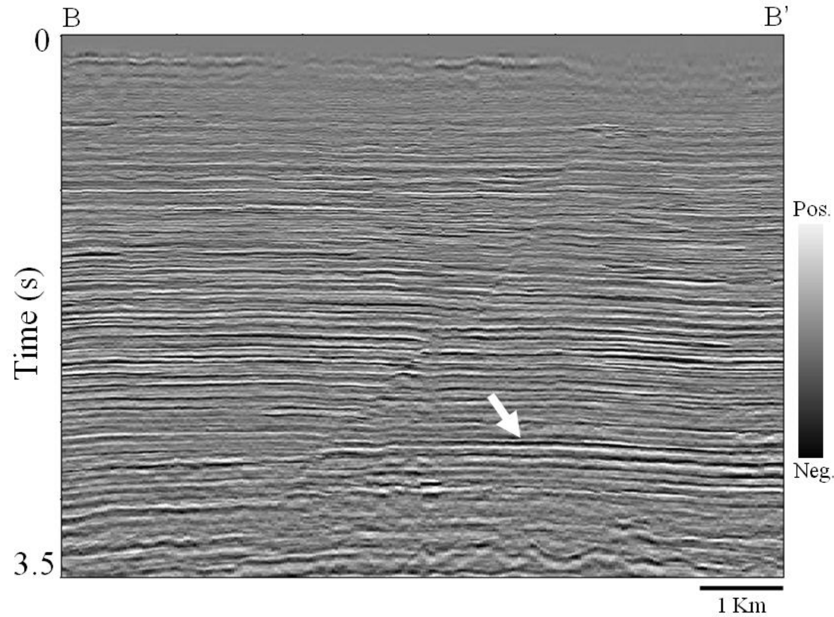

Figure 6.8 Seismic line B-B'. (Seismic data courtesy of Fairfield Industries)

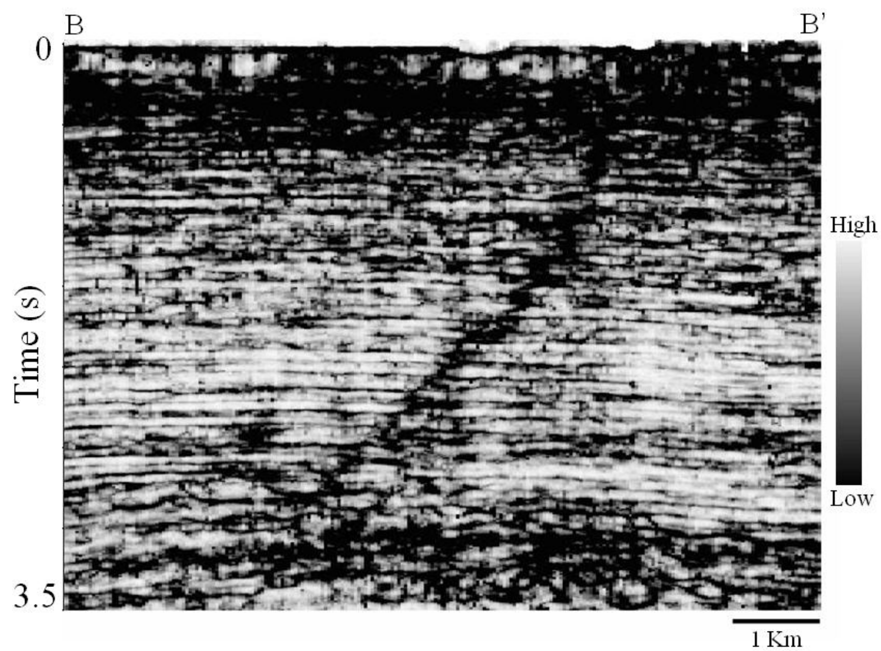

Figure 6.9 The coherence section of seismic line B-B' shown in Figure 6.8.

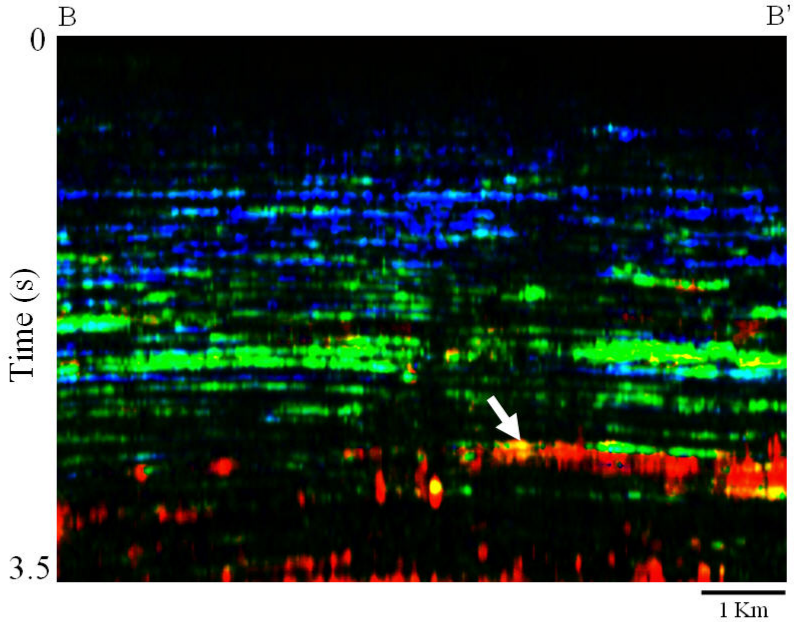

Figure 6.10 RGB plot of decomposed spectral amplitude spectra of seismic line B-B'.

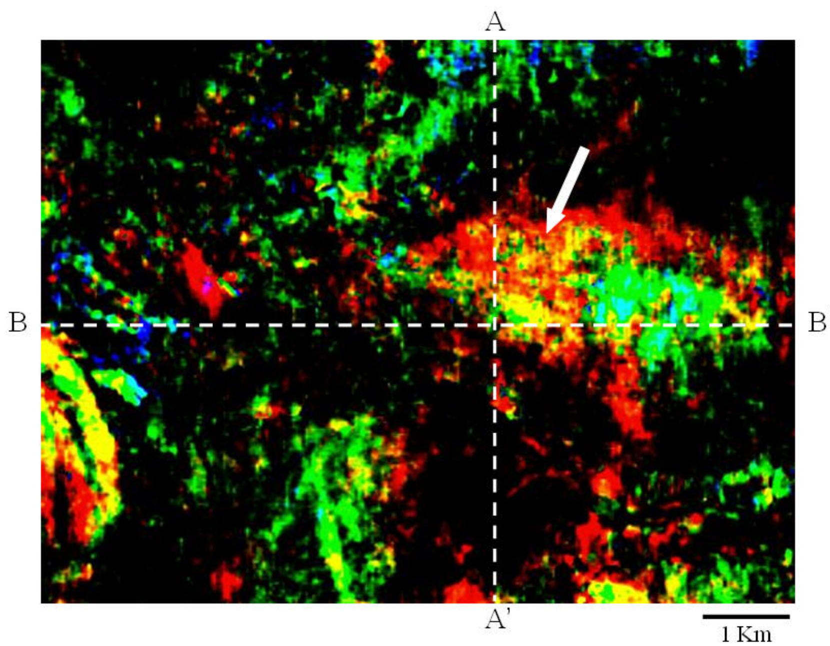

Figure 6.11 RGB plot of decomposed spectral amplitude along the picked horizon slice around 2.6 s.

6.3 PETROPHYSICAL MODELING OF LOW FREQUENCY ANOMALIES

From the section above, we note a spectral shift to lower frequency. To test which petrophysical parameter contributes to the spectral shift, I make the following numerical tests. The petrophysical parameters include velocity change, density change, and constant quality factor “Q” model.

Taner and Treitel (2003) made a constant Q model to generate synthetic responses and proposed a new attenuation prediction method. Modified from their five-layer model, I built a simple three layer model to generate the synthetic traces. The top and bottom layers are shale with sandstone in the middle. The parameters of the gas-saturated sandstone reservoir are shown in Figure 6.12. The sandstone thickness is 20 m. The source wavelet is a zero-phase Ricker wavelet with a peak frequency of 30 Hz.

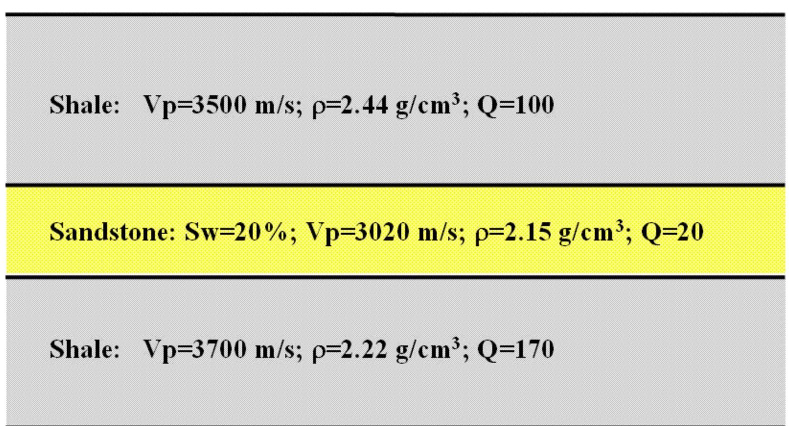

Figure 6.12 Three layer model. (S_w is water saturation, V_p is the P-wave velocity, ρ is the density, and Q is the quality factor)

In my first test I examine the sensitivity to the sandstone's velocity and keep all other parameters the same. The synthetic response is shown in Figure 6.13a (red color refers to velocity 2520 m/s, black refers to 3020 m/s, and blue refers to 3520 m/s,). The corresponding amplitude spectra are shown in Figure 6.13b. We can clearly see the peak frequency shift because of the thin bed response (time thickness changes due to velocity change). The higher velocity means smaller two way traveling time which in turn gives rise to a higher peak frequency if the thickness keeps the same. I also see the amplitude change due to different reflection coefficients calculated from P-wave impedance which is a function of both velocity and density.

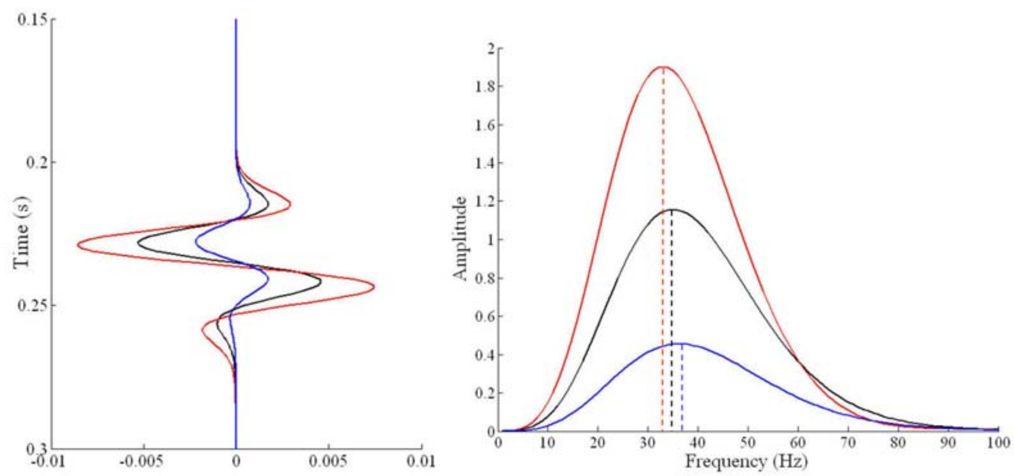

(a) (b)

Figure 6.13 Velocity test showing (a) the synthetic response with different velocities, and (b) the corresponding amplitude spectra with different velocities. (Red is 2520 m/s, black is 3020 m/s, and blue is 3520 m/s)

In my second test I examine the sensitivity to the sandstone's density. Figures 6.14a and 6.14b show the synthetic responses and the corresponding amplitude spectra with different density values. I find that density change will not shift the peak frequency, and it only affects the amplitude magnitude.

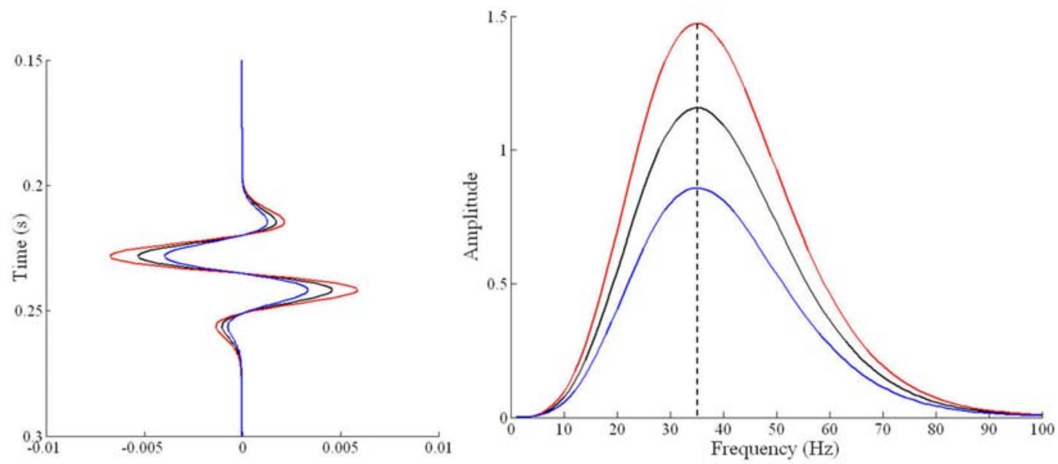

(a) (b)

Figure 6.14 Density test showing (a) the synthetic response, and (b) the corresponding amplitude spectra for different densities: ρ=2.0 g/cm^3 (red), ρ=2.15 g/cm^3 (black) and ρ=2.3 g/cm^3 (blue).

In my third test, I examine the effect of "Quality factor" Q on the spectral component amplitudes. In Figure 6.15a I generate the synthetic response of the thin layer with values of Q ranging from 5 to 60. In Figure 6.15b I plot the corresponding amplitude spectra. The response for Q=60 would be representative of a simple 'structural' or thin bed tuning response. From Figure 6.15b, I find for a 20 m thick thin bed that the peak frequency is relatively insensitive to Q. Even a very small Q value will not explain the shift to low frequencies seen in my real data thin bed response.

In my fourth and final test, I examine the sensitivity to three different fluids corresponding to gas, fizz water, and 100% water saturation. The rock property parameters are shown in Figure 6.16. The fizz water sand has the lowest Q value and P-wave velocity. The water sand has the highest Q value and P-wave velocity. Figures 6.17a and 6.17b show the resulting synthetic response and amplitude spectra, respectively. From Figure 6.17b, I find the peak frequencies have slightly changed which are caused by the combination effects of velocity and Q. The magnitudes of the amplitude spectra are quite different due to the different P-wave impedance contrasts

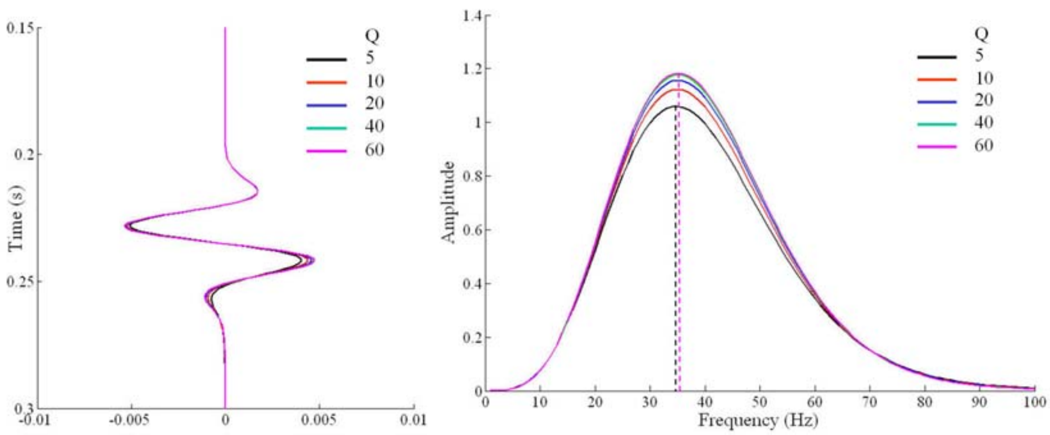

(a) (b)

Figure 6.15 Quality factor Q test showing (a) the synthetic response with different Q values, and (b) the corresponding amplitude spectra with different Q values.

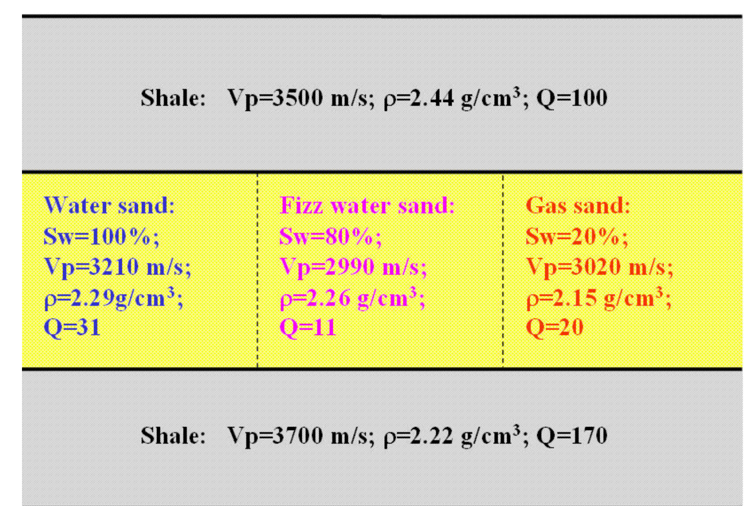

Figure 6.16 Three layer models with gas sand, fizz water sand and water sand. (S_w is the water saturation, V_p is the P-wave velocity, ρ is the density, and Q is the quality factor)

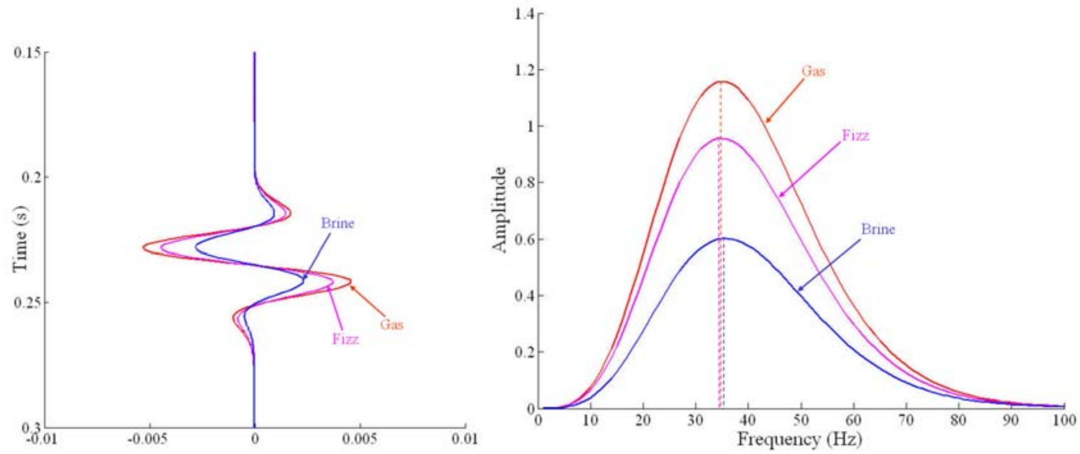

(a) (b)

Figure 6.17 Fluid content test showing (a) the synthetic responses, and (b) the corresponding amplitude spectra for gas sand, fizz water sand and water sand.

6.4 SUMMARY

Low frequency zones can be detected by using Red-Green-Blue display technique. Constant Q tests show that even very small Q value is not enough to shift high frequency to low frequency for a thin bed reservoir. The shift to low frequency is therefore due to either inaccurate seismic imaging, to multiple layers interference, or to some more complex attenuation mechanisms.

REFERENCES

Bahorich, M., and S. Farmer, 1995, 3D seismic discontinuity for faults and stratigraphic features: The coherence cube: The Leading Edge, **14**, 1053-1058.

Barnes, A. E., 1993, Instantaneous spectral bandwidth and dominant frequency with applications to seismic reflection data: Geophysics, **58**, 419-428.

Bodine, J. H., 1984, Waveform analysis with seismic attributes: 54th Annual International Meeting of the Society of Exploration Geophysicists, Expanded Abstracts, 505-509.

Chakroborty, A., and D. Okaya, 1995, Frequency-time decomposition of seismic data using wavelet based methods: Geophysics, **60**, 1906-1916.

Castagna, J., S. Sun, and R. Siegfried, 2003, Instantaneous spectral analysis: Detection of low-frequency shadows associated with hydrocarbons: The Leading Edge, **22**, 120-127.

Chopra, S., 2001, Adding the coherence dimension to 3D seismic data: CSEG Recorder, **26**, no. 1, 5–8.

Chopra, S., and K. J. Marfurt, 2006, Seismic attribute mapping of structure and stratigraphy: Society of Exploration Geophysicists, Tulsa, OK.

Chuang, H., and D. C. Lawton, 1995, Frequency characteristics of seismic reflections from thin beds: Canadian Journal of Exploration Geophysics, **31**, 32-37.

Cohen, L., 1995, Time frequency analysis: Prentic Hall PTR.

Dilay, A., and J. Eastwood, 1995, Spectral analysis applied to seismic monitoring of thermal recovery: The Leading Edge, **14**, Issue 11, 1117-1222.

Ebrom, D., 2004, The low-frequency gas shadow on seismic sections: The Leading Edge, **23**, Issue 8, 772.

Fahmy, W. A., G. Matteucci, D. Butters, and J. Zhang, 2005, Successful application of spectral decomposition technology toward drilling of a key offshore development well: 75th Annual International Meeting of the Society of Exploration Geophysicists, Expanded Abstracts, 262-264.

Goloshubin, G., C. V. Schuyver, V. Korneev, D. Silin, and V. Vingalov, 2006, Reservoir imaging using low frequencies of seismic reflections: The Leading Edge, **25**, Issue 5, 527-531.

Hardage, B. A., D. L. Carr, D. E. Lancaster, J. L. Simmons, Jr., R.Y. Elphick, V. M. Pendelton, and R. A. Johns, 1996, 3-D seismic evidence for the effects of carbonate karst breccia collapse on overlying clastic stratigraphy and reservoir compartmentalization: Geophysics, **61**, 1336-1350.

Laughlin, K., P. Garossino, and G. Partyka, G., 2002, Spectral decomposition applied to 3D: AAPG Explorer, **23**, No. 5, 28-31.

Lin, I., K. J. Marfurt, and O. Johnson, 2003, Mapping 3-D multiattribute data into HLS color space: Applications to Vinton dome, LA: 73rd Annual International Meeting of the Society of Exploration Geophysicists, Expanded Abstracts, 1728–1731.

Liu, J., Y. Wu, D. Han, and X. Li, 2004, Time-frequency decomposition based on Ricker wavelet: 74th Annual International Meeting Society of Exploration Geophysicists, Expanded Abstracts, 1937-1940.

Liu, J., and K. J. Marfurt, 2005, Matching pursuit decomposition using Morlet wavelets: 75th Annual International Meeting Society of Exploration Geophysicists, Expanded Abstracts, 786-789.

Luo, Y., S. al-Dossary, M. Marhoon, and M. Alfaraj, 2003, Generalized Hilbert transform and its application in geophysics: The Leading Edge, **22,** 198-202.

Mallat, S., 1999, A wavelet tour of signal processing: Academic Press, 2nd edition.

Mallat, S., and Z. Zhang, 1993, Matching pursuit with time-frequency dictionaries: IEEE transactions in signal processing, **41**, 3397-3415.

Marfurt, K. J., R. L. Kirlin, S. L. Farmer, and M. S. Bahorich, 1998, 3D seismic attributes using a semblance-based coherency algorithm: Geophysics, **63**, 1150-1165.

Marfurt, K.J., and R. L. Kirlin, 2001, Narrow-band spectral analysis and thin-bed tuning: Geophysics, **66**, 1274-1283.

Matos, M C., P. Osorio, E. C. Mundim, and M. Moraces, 2005, Characterization of thin beds through joint time-frequency analysis applied to a turbidite reservoir in Campos Basin, Brazil: 75th Annual International Meeting Society of Exploration Geophysicists, Expanded Abstracts, 1429-1432.

Mitchell, J. T., N. Derzhi, and E. Lickman, 1997, Low frequency shadows: The rule, or the exception?: 67th Annual International Meeting Society of Exploration Geophysicists, Expanded Abstracts, 685-686.

Morlet, J., G. Arens, E. Fourgeau, and D. Giard, 1982, Wave propagation and sampling theory-Part II: sampling theory and complex waves: Geophysics, **47**, 222-236.

Nissen, S. E., 2002, Seismic Attributes for the Explorationist: Kansas Geological Survey Open-file Report 2002-49: http://www.kgs.ku.edu/PRS/publication/2002/ofr49/page2.html (accessed June 26, 2006).

Odebeatu, E., J. Zhang, M. Chapman, E. Liu, and X. Li, 2006, Application of spectral decomposition to detection of dispersion of anomalies associated with gas saturation: The Leading Edge, **25**, Issue 2, 206-210.

Onstott, G. E., M. M. Backus, C. R. Wilson, and J. D. Phillips, J. D., 1984, Color display of offset dependent reflectivity in seismic data: 54th Annual International Meeting Society of Exploration Geophysicists, Expanded Abstracts, 674-675.

Partyka, G. A., J. Gridley, and J. Lopez, 1999, Interpretational applications of spectral decomposition in reservoir characterization: The Leading Edge, **18**, 353-360.

Partyka, G.A., 2001, Seismic thickness estimation: three approaches, pros and cons: 70th Annual International Meeting Society of Exploration Geophysicists, Expanded Abstracts, 503-506.

Peyton, L., R. Bottjer, and G. Partyka, 1998, Interpretation of incised valleys using new3-D seismic techniques: A case history using spectral decomposition and coherency: The Leading Edge, **17**, 1294–1298.

Robertson, J. D., and H. H. Nogami, 1984, Complex seismic trace analysis of thin beds: Geophysics, **49**, 344-352.

Sheriff, R. E., 2002, Encyclopedic dictionary of applied geophysics: Society of Exploration Geophysicists, Tulsa, OK.

Sinha, S., R. Routh, P. Anno, and J. Castagna, 2003, Time-frequency attribute of seismic data using continuous wavelet transform: 74th Annual International Meeting Society of Exploration Geophysicists, Expanded Abstracts, 1481-1484.

Sinha, S., R. Routh, P. Anno, and J. Castagna, 2005, Spectral decomposition of seismic data with continuous-wavelet transform: Geophysics, **70**, 19-25.

Stark, T. J., 2006, Visualization techniques for enhancing stratigraphic inferences from 3-D seismic data volumes: First Break, **24**, 75-85.

Stockwell, R. G., L. Mansinha, and R. P. Lowe, 1996, Localization of the complex spectrum: The S-Transform: IEEE Transactions on Signal Processing, **44**(4), 998-1001.

Sullivan, E. C., K. J. Marfurt, A. Lacazette, and M. Ammerman, 2006, Application of new seismic attributes to collapse chimneys in the Fort Worth Basin: accepted for publication in Geophysics.

Taner, M.T., F. Koehler, and R. E. Sheriff, 1979, Complex seismic trace analysis: Geophysics, **44**, 1041-1063.

Taner, M. T., 2000, Attributes revisited: http://www.rocksolidimages.com/pdf/attrib_revisited.htm (accessed June 22, 2006).

Taner, M. T., and S. Treitel, 2003, A robust method for Q estimation: 73th Annual International Meeting Society of Exploration Geophysicists, Expanded Abstracts, 710-713.

Taner, M. T., and S. Treitel, 2004, Harmonic attributes: 74th Annual International Meeting Society of Exploration Geophysicists, Expanded Abstracts, 1547-1550.

Widess, M.B., 1973, How thin is a thin bed?: Geophysics, **38**, 1176-1180.

Yang, M., 2003, Monochromatic AVO: An indicator that sees through wave interference: 73th Annual International Meeting Society of Exploration Geophysicists, Expanded Abstracts, 208-210.

APPENDIX A
MANPAGE OF ALGORITHM SPEC_PROJ

NAME

spec_proj - spectral decomposition using short window discrete Fourier transform or S-transform. Short window discrete Fourier transform is using the fixed length Gaussian window, while S-transform is using frequency dependent Gaussian window. The output files can include decomposed spectral magnitude, phase or calculated instantaneous average frequency, dominant frequency and bandwidth. This program can also generate the Red, Green and Blue files for RGB plot.

SYNOPSIS

d_fn=*d_fn* **spec_mag_fn**=*spec_mag_fn* **spec_phase_fn**=*spec_phase_fn* **spec_trace_mag_fn**=*spec_trace_mag_fn* **spec_trace_phase_fn**=*spec_trace_phase_fn* **avg_freq_fn**=*avg_freq_fn* **dom_freq_fn**=*dom_freq_fn* **bandwidth_fn**=*bandwidth_fn* **blue_fn**=*blue_fn* **green_fn**=*green_fn* **red_fn**=*red_fn* **fmin_out**=*fmin_out* **fmax_out**=*fmax_out* **df_out**=*df_out* **first_line_out**=*first_line_out* **last_line_out**=*last_line_out* **first_cdp_out**=*first_cdp_out* **last_cdp_out**=*last_cdp_out* **st**=*st* **kc**=*kc* **f_blue**=*f_blue* **f_green**=*f_green* **f_red**=*f_red*

DESCRIPTION

spec_proj reads in a seismic data volume and decomposes it using short window discrete Fourier transform or S-transform.

Command line arguments

d_fn=*d_fn* (Default - NONE)

Enter the SEP90 format input seismic file to be decomposed. The history file of the input should include the following information:
o1=first time sample in seconds
d1=sample increment in seconds
n1=number of time samples
o2=first cdp number
d2=cdp number increment (usually=1)
n2=number of cdps
o3=first line number
d3=line number increment (usually=1)
n3=number of lines

spec_mag_fn=*spec_mag_fn* (Optional output file)

Enter the string that will form the root of a suite of SEP90 format file names containing the magnitude of the spectral components. For example, if *spec_mag_fn='spec_mag_vinton'*, and if the output frequency parameters are *fmin_out=5, fmax_out=100.,* and *df_out=5*, then the output spectral magnitude components will be named, *spec_mag_vinton___5.H, spec_mag_vinton___10.H, spec_mag_vinton_vinton__15.H,..., spec_mag_vinton__95.H, spec_mag_vinton_100.H.* Each output file contains a 'cube' of spectral magnitudes for a given frequency.

spec_phase_fn=*spec_phase_fn* (Optional output file)

Enter the string that will form the root of a suite of SEP90 format file names containing the phase of the spectral components. For example, if *spec_phase_fn='spec_phase_vinton'*, and if the output frequency parameters are *fmin_out=5, fmax_out=100.,* and *df_out=5*, then the output spectral phase components will be named, *spec_phase_vinton___5.H, spec_phase_vinton___10.H, spec_phase_vinton_vinton__15.H,..., spec_phase_vinton__95.H, spec_phase_vinton_100.H.* Each output file contains a 'cube' of spectral phases for a given frequency.

spec_trace_mag_fn=*spec_trace_mag_fn* (Optional output file)

Enter the file name of the SEP90 format output that contains the magnitude of the spectrum trace by trace (usually for single trace test). The spectrum magnitudes are saved in sequential frequency series, e. g. from 1, 2, 3... 100 Hz.

spec_trace_phase_fn=*spec_trace_phase_fn* (Optional output file)

Enter the file name of the SEP90 format output that contains the phase of the spectrum trace by trace (usually for single trace test). The spectrum phases are saved in sequential frequency series, e. g. from 1, 2, 3 ...100 Hz.

avg_freq_fn=*avg_freq_fn* (Optional output file)

Enter the file name of the SEP90 format output that contains the instantaneous average frequency spectrum. The instantaneous average frequency spectrum is generated for each time location.

dom_freq_fn=*dom_freq_fn* (Optional output file)

Enter the file name of the SEP90 format output that contains the instantaneous dominant frequency spectrum. The instantaneous dominant frequency spectrum is generated for each time location.

bandwidth_fn=*bandwidth_fn* (Optional output file)

Enter the file name of the SEP90 format output that contains the instantaneous bandwidth. The instantaneous bandwidth is generated for each time location.

f_red_fn=*f_red_fn* (Optional output file)

Enter the file name of the SEP90 format output that contains the low frequency basis function coefficients. The high frequency center is defined by the parameter f_red. This file will be used for Red-Green-Blue plot.

f_green_fn=*f_green_fn* (Optional output file)

Enter the file name of the SEP90 format output that contains the middle frequency basis function coefficients. The high frequency center is defined by the parameter f_green. This file will be used for Red-Green-Blue plot.

f_blue_fn=*f_blue_fn* (Optional output file)

Enter the file name of the SEP90 format output that contains the high frequency basis function coefficients. The high frequency center is defined by the parameter f_blue. This file will be used for Red-Green-Blue plot.

fmin_out=*fmin_out* (Default=10.0)

Enter the minimum frequency of the spectral components to be output in Hz.

fmax_out=*fmax_out* (Default=80.0)

Enter the maximum frequency of the spectral components to be output in Hz.

df_out=*df_out* (Default=5.0)

Enter the frequency increment of the spectral components to be output in Hz.

f_red=*f_red* (Default=10)

Enter the high frequency basis function's center frequency, e.g. 10 Hz.

f_green=*f_green* (Default=30)

Enter the middle frequency basis function's center frequency, e.g. 30 Hz.

f_blue=*f_blue* (Default=50)

Enter the low frequency basis function's center frequency, e.g. 50 Hz.

kc=*kc* (Default=20)

Enter the parameter values to define the fixed Gaussian window which is used in short window discrete Fourier transform.

st=*y* (Default=y)

Enter the 'y' or 'n' to define the spectral decomposition is using S-transform (st=y) or short window discrete Fourier transform (st=n).

MPI

This program spec_proj is only running with MPI.

BUGS

No bugs known at present.

SEE EXAMPLES /seismic/code/scripts/spec_proj.sh

```
mpirun -np 6 -machinefile ./tower_101_processors -v spec_proj
    d_fn=test.H
    spec_mag_fn=spec_mag_test.H
    spec_phase_fn=spec_phase_test.H
    f_red_fn=f_red_test.H
    f_green_fn=f_green_test.H
    f_blue_fn=f_blue_test.H
    avg_freq_fn=avg_freq_test.H
    dom_freq_fn=dom_freq_test.H
    bandwidth_fn=bandwidth_test.H
    fmin_out=10
    fmax_out=80
    df_out=10
    f_red=60
    f_green=40
    f_blue=20
    st=y
    kc=20
```

spec_cmp

RESTRICTIONS

AUTHORS

Jianlei Liu and Kurt J. Marfurt. Allied Geophysical Laboratories, University of Houston. Version June 9, 2006.

APPENDIX B
MANPAGE OF ALGORITHM SPEC_CMP

NAME

spec_cmp - decomposes seismic data into either Ricker or Morlet wavelets using a matching pursuit technique. The complex spectrum (amplitude and phase) of each wavelet is accumulated to generate a time-frequency spectral decomposition.

SYNOPSIS

d_fn=*d_fn* **amp_fn**=*amp_fn* **freq_fn**=*freq_fn* **phase_fn**=*phase_fn* **modeled_fn**=*modeled_fn* **residual_fn**=*residual_fn* **wavelet_fn**=*wavelet_fn* **spec_mag_fn**=*spec_mag_fn* **spec_phase_fn**=*spec_phase_fn* **peak_freq_fn**=*peak_freq_fn* **peak_phase_fn**=*peak_phase_fn* **peak_amp_fn**=*peak_amp_fn* **peak_amp_above_avg_fn**=*peak_amp_above_avg_fn* **spec_trace_mag_fn**=*spec_trace_mag_fn* **spec_trace_phase_fn**=*spec_trace_phase_fn* **avg_spec_fn**=*avg_spec_fn* **avg_spec_scale_fn**=*avg_spec_scale_fn* **spec_scale_fn**=*spec_scale_fn* **red_fn**=*red_fn* **green_fn**=*green_fn* **blue_fn**=*blue_fn* **fmin_table**=*fmin_table* **fmax_table**=*fmax_table* **df_table**=*df_table* **fmin_out**=*fmin_out* **fmax_out**=*fmax_out* **df_out**=*df_out* **maxiter**=*maxiter* **tol**=*tol* **pc_max**=*pc_max* **pc_fnorm**=*pc_fnorm* **dphase**=*dphase* **change_min**=*change_min* **first_line_out**=*first_line_out* **last_line_out**=*last_line_out* **first_cdp_out**=*first_cdp_out* **last_cdp_out**=*last_cdp_out* **ttaper**=*ttaper* **wavelet**=*wavelet* **interp**=*interp* **verbose**=*verbose*

DESCRIPTION

spec_cmp reads in a seismic data volume and decomposes it into either Ricker or Morlet wavelets using a matching pursuit algorithm and least squares solution. Each wavelet is expressed by an amplitude, phase, and frequency, which in turn can be broken into Fourier spectral components, thereby generating a spectral decomposition.

Command line arguments

d_fn=*d_fn* (Default - NONE)

Enter the SEP90 format input seismic file to be decomposed. The history file of the input should include the following information:
o1=first time sample in seconds
d1=sample increment in seconds
n1=number of time samples

o2=first cdp number
d2=cdp number increment (usually=1)
n2=number of cdps
o3=first line number
d3=line number increment (usally=1)
n3=number of lines

amp_fn=*amp_fn* (Optional output file)
Enter the file name of the SEP90 format output that contains the amplitude (envelope) of each wavelet used to fit the input data.

freq_fn=*freq_fn* (Optional output file)
Enter the file name of the SEP90 format output that contains the frequency of each wavelet used to fit the input data.

phase_fn=*phase_fn* (Optional output file)
Enter the file name of the SEP90 format output that contains the phase of each wavelet used to fit the input data.

modeled_fn=*modeled_fn* (Optional output file)
Enter the file name of the SEP90 format output that contains the modeled (that part of the data fit by the wavelets) seismic data.

residual_fn=*residual_fn* (Optional output file)
Enter the file name of the SEP90 format output that contains the residual (that part of the data NOT fit by the wavelets) seismic data.

spec_mag_fn=*spec_mag_fn* (Optional output file)
Enter the string that will form the root of a suite of SEP90 format file names containing the magnitude of the spectral components. For example, if *spec_mag_fn='spec_mag_vinton'*, and if the output frequency parameters are *fmin_out=5, fmax_out=100.,* and *df_out=5*, then the output spectral magnitude components will be named, *spec_mag_vinton___5.H, spec_mag_vinton___10.H, spec_mag_vinton_vinton__15.H,..., spec_mag_vinton__95.H, spec_mag_vinton_100.H*. Each output file contains a 'cube' of spectral magnitudes for a given frequency.

spec_phase_fn=*spec_phase_fn* (Optional output file)
Enter the string that will form the root of a suite of SEP90 format file names containing the phase of the spectral components. For example, if *spec_phase_fn='spec_phase_vinton'*, and if the output frequency parameters are *fmin_out=5, fmax_out=100.,* and *df_out=5*, then the output spectral phase components will be named, *spec_phase_vinton___5.H, spec_phase_vinton___10.H, spec_phase_vinton_vinton__15.H,..., spec_phase_vinton__95.H, spec_phase_vinton_100.H*. Each output file

contains a ’cube’ of spectral phases for a given frequency.

peak_freq_fn=*peak_freq_fn* (Optional output file)
Enter the file name of the SEP90 format output that contains the peak frequency (or mode) of the spectrum estimated at each point in the input data volume. The peak frequency is often an indicator of thin bed tuning.

peak_phase_fn=*peak_phase_fn* (Optional output file)
Enter the file name of the SEP90 format output that contains the phase at the peak frequency (or mode) of the spectrum estimated at each point in the input data volume. The peak phase may help in differentiating upward fining vs. upward coarsening sequences, as well as enhancing lateral discontinuities.

peak_amp_fn=*peak_amp_fn* (Optional output file)
Enter the file name of the SEP90 format output that contains the amplitude of the spectrum at the peak frequency (or mode) of the spectrum estimated at each point in the input data volume. The amplitude is a function of both the reflection coefficient and thin bed tuning.

peak_amp_above_avg_fn=*peak_amp_above_avg_fn* (Optional output file)
Enter the file name of the SEP90 format output that contains the amplitude of the spectrum at the peak frequency (or mode) of the spectrum as measured above the average spectrum. Subtracting out the average spectrum reduces the appearance of high amplitude, flat spectrum reflections, and enhances the appearance of high amplitude, highly tuned spectrum reflections.

spec_trace_mag_fn=*spec_trace_mag_fn* (Optional output file)
Enter the file name of the SEP90 format output that contains the magnitude of the spectrum trace by trace (usually for single trace test). The spectrum magnitudes are saved in sequential frequency series, e. g. from 1, 2, 3, ...100 Hz.

spec_trace_phase_fn=*spec_trace_phase_fn* (Optional output file)
Enter the file name of the SEP90 format output that contains the phase of the spectrum trace by trace (usually for single trace test). The spectrum phases are saved in sequential frequency series, e. g. from 1, 2, 3, ...100 Hz.

avg_spec_fn=*avg_spec_fn* (Optional output file)
Enter the file name of the SEP90 format output that contains the average spectrum. The average spectrum is saved for each time slice with frequency ranges from minimum frequency to maximum frequency.

avg_spec_scale_fn=*avg_spec_scale_fn* (Optional output file)
Enter the file name of the SEP90 format output that contains the scaled average spectrum (after spectrum balancing). The scaled average spectrum is

saved for each time slice with frequency ranges from minimum frequency to maximum frequency.

spec_scale_fn=*spec_scale_fn* (Optional output file)
Enter the file name of the SEP90 format output that contains the magnitude of the scaled spectrum after spectrum balancing (usually for single trace test). The scaled spectrum magnitudes are saved in sequential frequency series, e. g. from 1, 2, 3, ...100 Hz.

f_red_fn=*f_red_fn* (Optional output file)
Enter the file name of the SEP90 format output that contains the low frequency basis function coefficients. The high frequency center is defined by the parameter f_red. This file will be used for Red-Green-Blue plot.

f_green_fn=*f_green_fn* (Optional output file)
Enter the file name of the SEP90 format output that contains the middle frequency basis function coefficients. The high frequency center is defined by the parameter f_green. This file will be used for Red-Green-Blue plot.

f_blue_fn=*f_blue_fn* (Optional output file)
Enter the file name of the SEP90 format output that contains the high frequency basis function coefficients. The high frequency center is defined by the parameter f_blue. This file will be used for Red-Green-Blue plot.

fmin_table=*fmin_table* (Default=10.0)
Enter the minimum peak or center frequency of the tabled wavelets in Hz.

fmax_table=*fmin_table* (Default=100.0)
Enter the maximum peak or center frequency of the tabled wavelets in Hz.

df_table=*df_table* (Default=1.0)
Enter the increment of the peak or center frequency of the tabled wavelets in Hz.

fmin_out=*fmin_out* (Default=10.0)
Enter the minimum frequency of the spectral components to be output in Hz.

fmax_out=*fmax_out* (Default=100.0)
Enter the maximum frequency of the spectral components to be output in Hz.

df_out=*df_out* (Default=5.0)
Enter the frequency increment of the spectral components to be output in Hz.

maxiter=*maxiter* (Default=1)
Enter the maximum number of iterations to be used in the matching pursuit

waveform fitting.

tol=*tol* (Default=0.01)
Enter the fractional value of the rms energy of each trace below which the matching pursuit algorithm will be declared to have completed.

pc_max=*pc_max* (Default=0.50)
At each iteration, fit only those wavelets whose envelope falls above *pc_max** the maximum envelope of the current residual trace.

change_min=*change_min* (Default=0.02)
Enter the minimal fractional change in the convergence rate. If the rms energy of the residual does not decrease by more than a factor of *change_min* from the previous iteration, the iteration processed will be declared to have converged.

pc_fnorm=*pc_fnorm* (Default=0.05)
A normalization term in spectral balancing. If *a_max* is the maximum average spectral amplitude for the current time slice, and if *a(f)* is the average spectral amplitude for frequency *f* for the current time slice, then the amplitude at frequency *f* will be rescaled to be: @ a(f) = a(f) over (a(f) + pc_norm*amax) @

ttaper=*ttaper* (Default=1./(2.*fmin_table))
Enter the temporal taper to be applied to the beginning and end of the seismic trace. The software does not allow wavelet centers to fall off the trace.

f_red=*f_red* (Default=10)
Enter the high frequency basis function's center frequency, e.g. 10 Hz.

f_green=*f_green* (Default=30)
Enter the middle frequency basis function's center frequency, e.g. 30 Hz.

f_blue=*f_blue* (Default=50)
Enter the low frequency basis function's center frequency, e.g. 50 Hz.

wavelet=*wavelet* (Default='r')
Enter 'r' for Ricker or 'm' for Morlet to define the wavelet basis function. Since most input spectra are characterized by a bias towards the low end of the spectra, the Ricker wavelets ('r') in general result in smaller residuals and faster convergence.

verbose=*verbose* (Default='n')
Enter 'y' or 'n' to turn on verbose output. Useful in tracking down program

data flow errors.

MPI

This program spec_cmp is only running with MPI.

BUGS

No bugs known at present.

SEE EXAMPLES /seismic/code/scripts/spec_cmp.sh

```
mpirun -np 6 -machinefile /seismic/code/processors/tower_101_processors -v
spec_cmp
    d_fn=test.H
    spec_mag_fn=spec_mag_test.H
    spec_phase_fn=spec_phase_test.H
    fmin_out=10
    fmax_out=80
    df_out=10
    ttaper=0.01
    maxiter=100
    pc_max=0.8
    tol=0.05
    change_min=0.01
```

spec_proj, slice

RESTRICTIONS

AUTHORS

Jianlei Liu and Kurt J. Marfurt. Allied Geophysical Laboratories, University of Houston. Version June 9, 2006.

APPENDIX C
MANPAGE OF ALGORITHM GENERATE_PPM

NAME

generate_ppm - generate Red_Green_Blue graph file in .ppm format.

SYNOPSIS

red_fn=*red_fn* **green_fn=***green_fn* **blue_fn=***blue_fn* **line=***line* **cdp=***cdp*
slicetime=*slictime*

DESCRIPTION

generate_ppm reads in three Red, Green and Blue files and generates the RGB file in .ppm format.

generate_ppm red_fn= green_fn= blue_fn= line= cdp= slicetime= ppm_fn=

Command line arguments

red_fn=*red.H* (Required input file name)

Enter the SEP90 format input file to be used to generate RGB graph file. The red file is for low frequency basis function. The history file of the input should include the following information:
o1=first time sample in seconds
d1=sample increment in seconds
n1=number of time samples
o2=first cdp number
d2=cdp number increment (usually=1)
n2=number of cdps
o3=first line number
d3=line number increment (usually=1)
n3=number of lines

green_fn=*green.H* (Required input file name, same format as red_fn)

Enter the SEP90 format input file to be used to generate RGB graph file. The green file is for middle frequency basis function.

blue_fn=*blue.H* (Required input file name, same format as red_fn)

Enter the SEP90 format input file to be used to generate RGB graph file. The blue file is for high frequency basis function.

line=*line* (Default='NONE')

Enter the line number for output RGB graph file.

cdp=*cdp* (Default='NONE')
Enter the cdp number for output RGB graph file.

slicetime=*slicetime* (Default='NONE')
Enter the slice time in second for output RGB graph file.

BUGS

No bugs known at present.

SEE EXAMPLES /seismic/code/scripts/generate_ppm.sh

generate_ppm red_fn=red_test.H green_fn=green_test.H blue_fn=blue_test.H line=200 ppm_fn=rgb_output_line_test.ppm

RESTRICTIONS

AUTHORS

Jianlei Liu and Kurt J. Marfurt. Allied Geophysical Laboratories, University of Houston. Version June 9, 2006.

APPENDIX D
MANPAGE OF ALGORITHM FLATTEN

NAME

flatten - flatten the seismic volume with input horizon time values.

SYNOPSIS

horizon_fn=*horizon_fn* **tstart=***tstart* **tend=***tend*

DESCRIPTION

flatten reads in a seismic data volume and flatten it using the time values from horizon file.

flatten < input.H horizon_fn= tstart= tend= > output.H

Command line arguments

< *(standard SEP input file)* (Required input file name)

Enter the SEP90 format input seismic file to be flattened. The history file of the input should include the following information:
o1=first time sample in seconds
d1=sample increment in seconds
n1=number of time samples
o2=first cdp number
d2=cdp number increment (usually=1)
n2=number of cdps
o3=first line number
d3=line number increment (usually=1)
n3=number of lines

horizon_fn=*horizon_fn* (Required input horizon file name)

Enter the horizon file of SEP90 format containing the time values of the picked horizon. The horizon file only has one number of n1. n2 and n3 have the same number of input seismic volume.
o1=1
d1=1
n1=1
o2=first cdp number
d2=cdp number increment (usually=1)
n2=number of cdps
o3=first line number
d3=line number increment (usually=1)
n3=number of lines

tstart=*tstart* (Default=-0.05)

Enter the start time with respect to picked horizon in second (positive=below, negative=above).

tend=*tend* (Default=0.05)

Enter the end time with respect to picked horizon in second (positive=below, negative=above).

> *(standard SEP output file)* (Required output file name)

Enter the SEP90 format output seismic file with volume defined by tstart and tend.

BUGS

No bugs known at present.

SEE EXAMPLES /seismic/code/scripts/flatten.sh

flatten < input.H horizon_fn=horizon_test.H tstart=-0.05 tend=0.05 > output.H

RESTRICTIONS

AUTHORS

Jianlei Liu and Kurt J. Marfurt. Allied Geophysical Laboratories, University of Houston. Version June 9, 2006.